

**THE STUDY OF CARBON MATERIALS FOR ENERGY STORAGE
SYSTEMS: FROM SYNTHESIS TO STRUCTURE**

by
Kyungho Kim

A Dissertation

*Submitted to the Faculty of Purdue University
In Partial Fulfillment of the Requirements for the degree of*

Doctor of Philosophy



School of Materials Engineering
West Lafayette, Indiana
May 2019

THE PURDUE UNIVERSITY GRADUATE SCHOOL
STATEMENT OF COMMITTEE APPROVAL

Prof. Jeffrey Youngblood, Co-Chair

School of Materials Engineering

Prof. Vilas G. Pol, Co-Chair

Davidson School of Chemical Engineering

Prof. Sebastian Osswald

School of Materials Engineering

Prof. Eric Kvam

School of Materials Engineering

Approved by:

Prof. David Bahr

Head of the Graduate Program

ACKNOWLEDGMENTS

First of all, I would like to extend my deepest appreciation to my advisors, Prof. Jeffrey Youngblood and Prof. Vilas Pol. They never catch the fish for me but teach me how to catch the fish. Professor Youngblood always inspire me as a scientist. He always make extra efforts to help students, not only in academics but far beyond that. In research, the scientific and experimental feedback from him encourage me to look at my research in a different perspective. This approach of his upgraded me as an independent scientist and researcher. Furthermore, I would like to thanks his willingness in discussing and advising how to develop my own career path.

Professor Pol constructive comments and help in building novel ideas, raised the quality of my research. His enthusiasm in research always inspire me. He shows great patience and encourage me to expand my interest in science, which makes me feel confident and comfortable all the time. Thanks to his help I was able to publish qualitative works which helped me to design my future career as a scientist. Also his advice on how to become a good teammate helped me to successfully finish collaboration work with many other groups.

I would like to also extend my deepest gratitude to Professor Osswald. His presentation during my first semester gave me confident that I want to work with him and explore the field of energy. He helped me to develop a mind-set as a Ph.D. researcher and how to become a successful researcher. He always make me feel comfortable to find him and talk with him even at weekend for various topics such as research, coursework, and daily life.

I am also very thankful to Professor Kvam. His advice ensured that I headed down to the correct research path. Furthermore, the courses I attended provided by him has improved my knowledge as a material scientist.

I would like to thank my Master's research advisor, Prof. Yeon-Sik Jung, who was the first professor to motivate me as a material scientist. Without his support and advices it would have been impossible for me to pursue my Ph.D. research in Purdue.

This thesis would not be successful without the help of Dr. Patrick J. Kim. Discussion with Dr. Kim carried me to the next level as an individual researcher. Also I enjoyed the conversation and advice from him, which relief my stress and helped me to develop my own career path as well. I also appreciate help from my group members, Dr. Daw Gen Lim, Dr. Jimmy Tang, Dr. Ryan Adams, Dr. Arthur Dysart, Dr. Kwangse Lee, Dr. Palanisam Manikandan, Dr. Dhanya Puthusseri,

Dr. Jassiel Rodriguez, Dr. Francisco Montes, Reaz Chowdhury, Mihit Parekh, Vihang Parikh, Caitlyn M Clarkson, and a lot of other graduate students. Also I would like to show my appreciation to my friends at Purdue, Dr. Jongsoo Kim, Hyungu Jeong, Wooram Kang, Hoon Choi, Jonghoon Ahn, Jaehun Bang, Jaehun Cho, Taehoo Chang, Hyung gyung Jo, Gyuchul Park, Heyoung Son, Sungho Yook, Philsun Yoo, and many others for their help and support.

Finally and the most importantly, the support from my family throughout my Ph.D period helped me finish my study. The trust and love from my parents and my sister encouraged me. The support from my family in law always make me feel comfort and confident. Thank you Saerom Wang, my wife, who always sacrificed herself to support me when she is also pursuing her Ph.D. here at Purdue. Her love always warm my heart, where I gain energy for the achievement in my studies.

TABLE OF CONTENTS

LIST OF TABLES	8
LIST OF FIGURES	9
ABSTRACT	12
1. INTRODUCTION TO CARBON	14
1.1 Overview	14
1.2 Various types of carbon	14
1.2.1 Graphite	14
1.2.2 Carbon nanotube (CNT)	15
1.2.3 Non-graphitic carbon derived from sustainable sources	16
1.3 Characteristics of carbon.....	17
1.3.1 Structure of carbon	17
1.3.2 Conductivity of carbon	18
1.3.3 Cost of carbon.....	18
1.4 Characterization of carbon.....	18
1.4.1 Electron microscopy analysis	19
1.4.2 Structure analysis.....	19
1.4.3 Surface area analysis.....	20
1.4.4 Conductivity analysis.....	21
1.4.5 Thermal analysis.....	21
1.5 Dissertation structure	22
1.6 References	23
2. CARBON-BASED MATERIALS FOR ENERGY STORAGE.....	26
2.1 Introduction of energy storage systems	26
2.1.1 Introduction to lithium ion battery.....	28
2.2 Definition of terms	31
2.2.1 Capacity	31
2.2.2 Voltage.....	31
2.2.3 Energy and Power Density	31
2.2.4 Coulombic efficiency and cycle life	32

2.3	Carbon in energy storage systems.....	33
2.4	References	34
3.	DRY AUTOCLAVE METHOD DERIVED CARBON MATERIAL FOR LITHIUM ION BATTERY	35
3.1	Introduction.....	35
3.1.1	Conventional carbon preparation methods	36
3.1.2	Dry-autoclave method	36
3.2	Experimental.....	37
3.2.1	Synthesis of spheroidal carbon particles.....	37
3.2.2	Materials characterization.....	38
3.2.3	Electrochemical characterization.....	38
3.3	Results and discussions.....	39
3.3.1	Morphological analysis.....	39
3.3.2	Structural analysis of spheroidal carbon by Raman spectroscopy and XRD	40
3.3.3	Mechanistic elucidation of spheroidal carbon formation	42
3.3.4	Electrochemical characterization.....	43
3.3.5	Pre and post diagnostics: spheroidal carbon electrode analysis before/after cycling	46
3.4	Conclusion	47
3.5	Reference	48
4.	CARBON DERIVED FROM BIOMASS FOR SODIUM ION BATTERY AND ITS STORAGE MECHANISM STUDY	52
4.1	Alternative energy storage system	52
4.2	Introduction to sodium ion batteries	52
4.3	Introduction of this work	53
4.4	Experimental.....	56
4.4.1	Synthesis of pistachio shell derived carbon.....	56
4.4.2	Material characterization	57
4.4.3	Electrochemical characterization.....	57
4.5	Results and discussion	58
4.5.1	Structural analysis of pistachio shell derived carbon by Raman spectroscopy and XRD	60

4.5.2	TEM analysis	61
4.5.3	Characterization of pistachio shell derived carbon by N ₂ adsorption-desorption	63
4.5.4	Electrochemical characterization	64
4.6	Conclusion	71
4.7	References	73
5.	UNIQUE STRUCTURE OF BIOMASS DERIVED CARBON FOR LITHIUM-SULFUR BATTERY	77
5.1	Introduction to lithium-sulfur batteries	77
5.1.1	Li-S battery challenges	79
5.1.2	Efforts to resolve Li-S battery challenges	79
5.2	Introduction of current work	80
5.3	Experimental	81
5.3.1	Preparation of pistachio shell-derived carbon (PC)	81
5.3.2	Fabrication of nano-MnO ₂ decorated pistachio shell-derived carbon (M-PC)	81
5.3.3	Preparation of sulfur cathode electrode (M-PC/S and PC/S)	81
5.3.4	Material characterization	82
5.4	Results and discussion	82
5.5	Conclusion	96
5.6	References	98
6.	SUMMARY AND FUTURE PROSPECTS	101
6.1	Coffee oil derived carbon for lithium ion battery	102
6.2	Biomass derived carbon for sodium ion battery and its storage mechanism study	102
6.3	Biomass derived carbon for lithium-sulfur battery	102
6.4	Future outlooks	103
	VITA	104
	PUBLICATIONS	105

LIST OF TABLES

Table 2.1 The comparison of various energy storage systems properties.	28
Table 2.2 The performance and cost of various energy storage systems.....	28
Table 3.1. Material Properties for Coffee-oil derived carbon.....	40
Table 3.2 Results from CHNO analysis. Average values are highlighted in yellow, with standard deviation below (values are in weight %).	42
Table 3.3 The elemental analysis of Fluorine in both room and elevated temperature cycled cell electrode.	45
Table 4.1 The characteristics comparison of lithium and sodium.	53
Table 4.2 Literature survey of various biomass derived carbon anodes and their electrochemical performance.	56

LIST OF FIGURES

Figure 1.1 Schematic diagram of the armchair and the zigzag edge structure.	16
Figure 1.2 Schematic of (a) graphite, (b) soft-carbon, and (c) hard-carbon.	16
Figure 2.1 The load profile of energy storage system in terms of system demand (MW) vs. time of day.	26
Figure 2.2 The typical LIB cell configuration and components. The electron and lithium ion travel direction during charge and discharge process is illustrated as well.	30
Figure 2.3 Illustration of Coulombic efficiency.	32
Figure 3.1 Schematic diagram demonstrating coffee oil derived spheroidal carbon.	37
Figure 3.2 Scanning electron microscopy images of carbon particle prepared after dry autoclaving process (a), (c) and after additional pyrolysis (b), (d).	39
Figure 3.3 N ₂ adsorption-desorption analysis of spheroidal carbon particles.	40
Figure 3.4 XRD (a) and Raman (b) spectra of coffee oil derived carbon.	41
Figure 3.5 Electrochemical performance of spheroidal carbon. First and second cycle charge-discharge voltage profile at 25 °C (a), 50 °C (b), long cycling of spheroidal carbon anodes at 100 mA/g (c), and rate performance (d).	44
Figure 3.6 Cycling performance of sodium and potassium ion batteries.	46
Figure 3.7 SEM images of spheroidal carbon electrode before (a, c) and after (b, d) Galvanostatic cycling. Raman spectra of electrode before (e) and after (f) cycling.	47
Figure 4.1 (a) TGA result of pistachio shell in inert atmosphere and (b) preparation of rechargeable SIB using pistachio shells derived carbon treated at 1000 °C.	59
Figure 4.2 Raman spectra (a), (b) and XRD analysis (c), (d) of pistachio shell derived carbons at various temperatures.	61
Figure 4.3 Different resolution TEM image and FFT pattern of pistachio shell (a) P700, (b) P1000, (c) P1300, and (d) P1500.	62
Figure 4.4 Calculation of SAED pixel size of each carbon and its d-spacing value.	63
Figure 4.5 (a) N ₂ adsorption and desorption curve and (b) surface area and pore volume of each carbonized sample.	64

- Figure 4.6 (a) First charge-discharge profile of all carbon; (b) desodiation cycling capacity of carbons at different current density; (c) first and second charge-discharge curve of P1000 and (d) dQ/dV of first and second cycle of P1000..... 65
- Figure 4.7 Desodiation capacity normalized in respect to surface area for all carbon samples at different current rates. 67
- Figure 4.8 Cyclic voltammetry (CV) for pistachio derived carbon cells at different scan rate (a), (b) and plot showing linear relation of $\log(v)$ vs. $\log(i)$ for discharge sweeps from CV. 68
- Figure 4.9 Discharge profile of (a) P700, (b) P1000, (c) P1300 and (d) P1500 at different current densities. 69
- Figure 4.10 Cycle stability test of carbon materials of P1000 at 40 mA g⁻¹ current density. 70
- Figure 4.11 (a) Cycle information up to 100 cycles showing the capacity drop and (b), (c) the optical image of deteriorated sodium foil, where the cell was dissembled after capacity drop..... 71
- Figure 5.1 Schematic diagram of Li-S battery..... 78
- Figure 5.2 Schematic diagram. The electrochemical behaviors of (a) PC/sulfur electrode and (b) M-PC/sulfur electrode during discharge. 83
- Figure 5.3 Characterization of PC and M-PC. (a) Before and after pyrolysis of pistachio shell; confirmation of nano-MnO₂ decoration by (b) BET, (c) XRD, (d) TGA; SEM images of (e) pristine PC and (f) M-PC (MnO₂ is indicated by yellow arrow); (g) EDS mapping; TEM images of (h) pristine PC and (i) M-PC (wrinkled structure). 85
- Figure 5.4 The (a) top-view and (b) cross-sectional view SEM image of pistachio derived carbon. 86
- Figure 5.5 Electrolyte permeability test on the PC substrate. Total 3 drops of electrolyte was fully percolated into the PC substrate after 10 min..... 86
- Figure 5.6 Electrochemical performances of M-PC/S-phy. and M-PC/S-chem. Schematic diagram of (a) M-PC/S-phy. and (b) M-PC/S-chem. during discharge/charge; voltage profiles of (c) M-PC/S-phy. and (d) M-PC/S-chem. at 1st and 100th cycles; (e) cycle performance with Coulombic efficiency at a current density of 1 C. 88
- Figure 5.7 Long-term electrochemical performances of PC/S and M-PC/S. (a) Cycle performance of PC/S and M-PC/S at a current density of 0.5 C; (b) voltage profiles of PC/S and (c) M-PC/S 1st and 250th cycle; EIS studies of (d) PC/S and (e) M-PC/S at different cycle numbers. 90
- Figure 5.8 Rate study of before/after decoration of MnO₂ on PC (a) and a voltage profile at difference C-rates of PC (b), M-PC (c). 91

- Figure 5.9 Raman spectroscopy before and after polysulfide absorption test. Schematic diagram to illustrate the role of (a) PC and (b) M-PC during electrochemical tests. Raman spectra for (c) PC and (d) M-PC before and after polysulfide absorption..... 93
- Figure 5.10 Polysulfide absorption test of M-PC/Phys. 94
- Figure 5.11 Characterization of Li metal foil after 250 cycle tests. Photographs of (a) Li foil in PC/S cell and (b) Li foil in M-PC/S cell; SEM images of (c) Li foil in PC/S cell and (d) Li foil in M-PC/S cell. 95
- Figure 5.12 XPS result of black spots on cycled PC lithium foil. 96

ABSTRACT

Author: Kim, Kyungho. PhD

Institution: Purdue University

Degree Received: May 2019

Title: The Study of Carbon Materials for Energy Storage Systems: From Synthesis to Structure

Committee Chair: Prof. Jeffrey Youngblood and Prof. Vilas Pol

Worldwide concern on fossil fuels depletion and adverse impact on environment pushed researchers to find an alternative energy source. Among various potential systems, electrochemical energy storage devices have attracted significant attraction due to short charge/discharge time, easy relocation, and relatively cheap cost compared to large storage systems. Much research has been reported to suggest a material for electrochemical storage systems. Carbon is a key part of human life in terms of energy source, building materials, daily clothing and foods. The extraordinary characteristics of carbon materials, including good conductivity, good structure stability, relatively low cost, and sustainability, draw interest to carbon application in energy storage systems.

The introduction of lithium ion batteries (LIB), using graphite as an anode material, fulfilled the need of alternative energy source and elevated the technologies into next level high-performance applications such as portable devices. While the technology advancement in high performance electronics fosters the development of advanced lithium ion batteries, the introduction of electric vehicles and large intermittent systems seeks energy storage devices with high capacity, sustainability, and low cost. In this thesis, the impact of the characteristics of carbon material on energy storage system performance is studied. The work presented in this thesis not only suggests a cost-effective carbon synthesis for advanced LIB, but also addresses how the carbon structure impact and resolves the systematic issue associated with next generation energy storage systems.

Chapter 3 describes a facile, one-step, solvent-free ‘dry autoclaving’ synthesis method utilizing coffee oil as the carbon precursor to obtain micrometer diameter spheroidal carbon particles for lithium ion battery anodes. The spheroidal morphology resulted from the evaporation of liquid oil into a liquid/gas phase interphase at elevated temperature (700 °C), followed by

solid/gas sublimation interactions during cooling (below 350 °C) in a closed autoclave. A mechanism of spheroidal carbon formation is proposed considering the precursor's composition and chemical interactions during autoclaving. The prepared carbon from dry autoclave has shown successful LIB performance and structure stability after 250 cycles.

Chapter 4 illustrates the temperature effect on the structure of biomass derived carbon. In this study, due to its abundance and high porosity, pistachio shells were selected as the primary carbon source and carbonized at a range from 700 to 1500 °C. The temperature effect on carbon structure was analyzed by XRD, Raman, BET, and electron microscopy. To propose an advanced lithium ion battery, pistachio shell-derived carbon was applied as an anode material for a sodium ion battery (SIB). The correlation of carbon structure and SIB electrochemical performance is presented. Pistachio shell carbonized at 1000 °C resulted in highly amorphous structure with specific surface area (760.9 m²/g) and stable cycle performance (225 mAh g⁻¹ at 10 mA g⁻¹). With support from Raman, XRD, and BET, the storage mechanism has been studied as well.

Chapter 5 describes the impact of carbon structure on resolving the polysulfide shuttling effect in lithium sulfur (Li-S) batteries. Lithium sulfur batteries have received tremendous attention due to its high theoretical capacity (1672 mAh g⁻¹), sulfur abundance, and low cost. However, main systemic issues, associated with polysulfide shuttling and low Coulombic efficiency, hinder the practical use of sulfur electrodes in commercial batteries. The work in this thesis demonstrated an effective strategy of decorating nano-MnO₂ (less than 10 wt. %) onto a sulfur reservoir in order to further capture the out-diffused polysulfides via chemical interaction, and thereby improve the electrochemical performance of sulfur electrodes without increasing the mass burden of the total battery configuration. Pistachio shell-derived sustainable carbon (PC) was employed as an effective sulfur container due to its structural characteristics (interconnected macro channels and micropores). With the aids of the structural benefits of PC scaffold and the uniform decoration of nano-MnO₂, the polysulfide shuttling effect was significantly suppressed and cycling performance of a sulfur cathode was dramatically improved over 250 cycles.

This thesis offers a new prospect in the study of carbon materials applications in various energy storage systems. This concept can be further extended to other applications, such as lithium metal batteries. The intercalation property of carbon structure can reduce the local current density, reducing the risk of lithium dendrite growth, which is the most critical issue of lithium metal battery.

1. INTRODUCTION TO CARBON

1.1 Overview

Carbon is an essential element for all living species, and one of the most abundant and versatile elements found on earth.¹ In addition, the existence of several allotropes and its capability to form bonds with various other elements make carbon a diverse element that can be found in more than a million carbon compounds.² Carbon is regarded as an important source for the development of modern technologies. Various carbon applications are found around us, including automobiles, portable devices, transportation systems, ink derived from lampblack, wood and coal for heat generation, oil and natural gas in modern technologies, graphite in nuclear energy sources, and many others.³⁻⁶ The recent concern on issues of fossil fuels increased research focus on sustainable and high performance energy storage systems. Fullerene-based semiconducting polymers in photovoltaics,^{7,8} carbon allotrope based transparent and electronically conductive films for solar cells,⁹ and carbon allotropes (graphite, CNT, activated carbon) in the battery industry describe the value of carbon as energy storage materials.¹⁰⁻¹²

In this chapter, different types of carbon allotropes and their characteristics are briefly discussed. Furthermore, characterization methods to verify these characteristics are briefly introduced.

1.2 Various types of carbon

1.2.1 Graphite

Graphite is, generally, stacks of graphene in AB ordering.¹³ Each layer of graphene is constructed with hexagonally arranged carbon atoms. The separation distance between carbon atoms is 0.142 nm and the interlayer spacing between graphene sheets is 0.335 nm.¹⁴ The unique structure of graphite makes it an interesting material for various applications. Each carbon atom in the hexagonal structure is bonded to three other carbon atoms. This leave one delocalized electron, in other words, a free electron, in the structure. Due to the free electron, graphite shows excellent conductive properties. In addition, the graphene layers in graphite can easily slip, attributed to the weak Van der Waals bonding between graphene layers, which is preferable for frictionless applications such as lubricants.

Owing to graphite's unique structure, graphite exhibits high thermal conductivity, electrical conductivity, temperature and chemical stability, high resistance to neutron radiation, low wettability by liquid metals, and self-lubricant property. Various industry and research fields have utilized graphite for its unique characteristics. The chemical and nuclear industries focused on high temperature and chemical stability properties of graphite.¹⁵ The friction coefficient is controlled by graphite additive into friction materials.¹⁶ Spark plasma sintering (SPS) uses graphite dies to generate high heat at a short amount of time.¹⁷ Lubricants, carbon brushes, and refractories use graphite as well.¹⁸ Furthermore, the excellent conductivity and the layered structure of graphite make it an excellent material for a secondary ion battery.

1.2.2 Carbon nanotube (CNT)

CNTs are a cylindrical carbon material with a diameter from 1 to 100 nm and lengths from several micrometers to millimeters, depending on the synthesis condition. Since their discovery by Iijima in 1991, CNTs have gained research interest as a new carbon material.¹⁹ CNTs are distinguished into two types, named single-walled (SWNTs) and multi-walled CNT (MWNTs).

The electrical conductivity of CNTs varies depending on the rolling-up direction of graphene sheets.²⁰ The armchair structure, so called because the diameter edge looks like the shape of armchair, have identical chiral indices and thereby exhibits high conductivity, while the zigzag edge exhibits semiconducting property. Figure 1.1 illustrates the armchair and zigzag edges. The specific mechanical strength of CNT can be 400 times than that of steel due to the strong sp^2 bonding formed between carbon atoms. The hollow interior of CNT can be filled with nanomaterials, to protect them from exterior environments.²¹ Furthermore, the regular arrangement of carbon atoms in CNT enables high thermal conductivity.

CNT characteristics provide various applications, including transistors for its semiconducting property, wearable electronics for its flexibility and transparency, and nanomedicine for its ability to store nanomaterials.^{22,23} The excellent electrical conductivity of CNTs make it a perfect material as an electrode for super-capacitors and batteries.

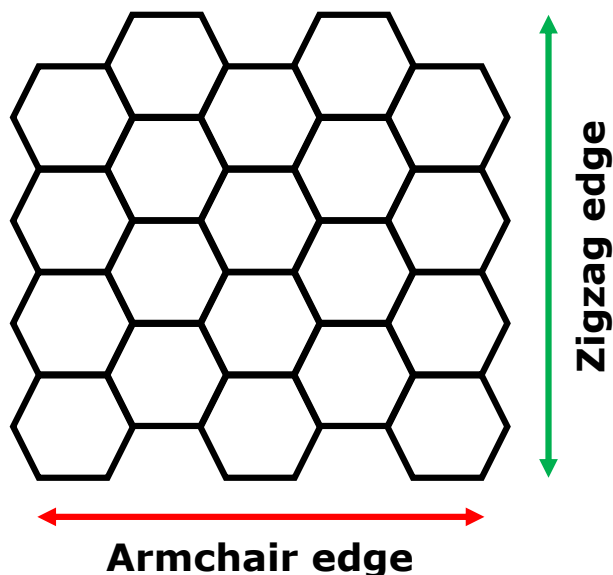


Figure 1.1 Schematic diagram of the armchair and the zigzag edge structure.

1.2.3 Non-graphitic carbon derived from sustainable sources

The structure of non-graphitic carbon consist a hexagonal planar network of carbon atoms but no crystallographic order in the vertical direction. Non-graphitic carbon is classified into two categories, named soft carbon and hard carbon. The exact definition of soft and hard carbon is still questionable, but it is roughly explained with the degree of graphitization at high temperature.^{24,25} While the carbon layers of soft carbon forms a graphitic layer at high temperature ($> 2500\text{ }^{\circ}\text{C}$), hard carbon does not form a well-ordered graphitic layer at even high temperature. Figure 1.2 illustrates the structure of graphite, soft carbon, and hard carbon.

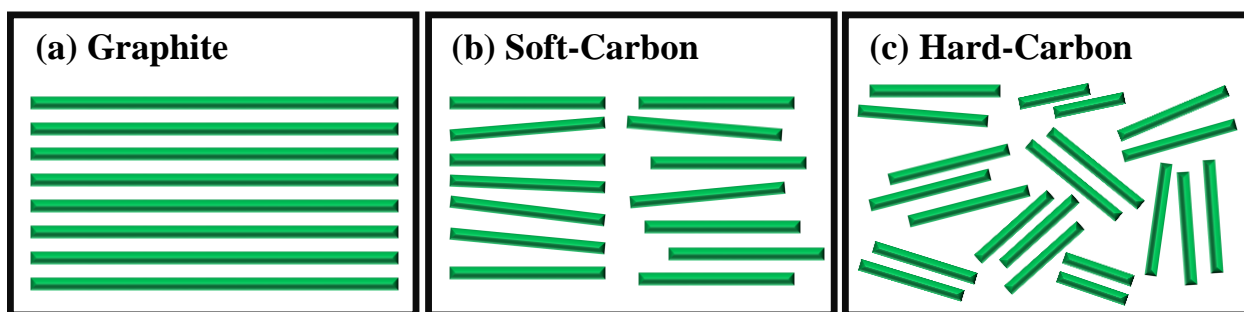


Figure 1.2 Schematic of (a) graphite, (b) soft-carbon, and (c) hard-carbon.

Soft carbon is mostly obtained from coal tar and petrol pitch, while hard carbon is mostly derived from phenolic resins and biomass. Hard carbon has advantages over soft carbon, including larger interlayer spacing, more storage sites, high structure stability, and small ion diffusion path. It has attracted attention as an anode material to obtain cost-effective, sustainable, and high capacity battery.²⁶ Hard carbon in lithium ion batteries is proposed to either compete with the capacity of conventional LIB or suggest a cheaper cell component.^{27,28} The sufficient interlayer spacing of hard carbon enables sodium intercalation storage.^{29,30} Hard carbon materials are introduced to resolve the issue associated with lithium sulfur and lithium metal batteries, such as the polysulfide shuttling effect and lithium dendrite growth, respectively.³¹⁻³³

1.3 Characteristics of carbon

1.3.1 Structure of carbon

The structure of hard carbon derived from sustainable sources (e.g. biomass) possess micropores, macro-channels, and carbon layers.³⁴ The macroporosity of carbon eases the permeation of electrolyte, which decreases the ionic diffusion length and improves the rate/capacity performance.^{35,36} The microporosity of hard carbon provides additional storage sites for a secondary ion battery, which increases the capacity of the battery. In addition, pore size smaller than 2-3 nm physically restricts polysulfide migration, improving the lithium-sulfur battery performance.³⁷

The layered structure of a hexagonal carbon atom array is one of the most important characteristics for various carbon applications. The weak Van der Waals bonding between carbon layers enables easy plane slip, which is favorable for less friction material additives. The ion storage between carbon layers, named intercalation, is the primary storage mechanism of secondary ion batteries (e.g. lithium ion battery, sodium ion battery, and potassium ion battery). Graphite, for example, has an interlayer spacing of 0.345 nm, which is sufficient for lithium storage.³⁸ Non-graphitic carbon has short-range ordering graphitic layer structure, where the interlayer spacing is larger than 0.360 nm. Thereby, non-graphitic carbon is suitable for all types of secondary ion batteries, including potassium-ion and sodium-ion batteries.^{39,40}

1.3.2 Conductivity of carbon

The recent development of large grid storage and electric vehicles requires a battery with a fast charge/discharge rate.^{41,42} To fulfill this qualification, the design and/or selection of electrode material is critical. One of the strategies is to use a conductive electrode material. Carbon materials can successfully answer this requirement. Both graphitic and non-graphitic carbon has layers of carbon with sp^2 -bonding, where three valence electrons are covalently bonded to neighbor carbon electrons, which leaves one electron delocalized. The free electron gives carbon materials excellent conductive properties. Lithium-sulfur batteries use carbon as a sulfur reservoir, since sulfur is an insulating material. Another example is carbon/metal or CNT/metal composites, where carbon materials provide both increment of conductivity and sites to accommodate the volume expansion of metal.⁴³

1.3.3 Cost of carbon

According to Tesla, UBS estimates, Umicore, and many other numerous reports, the portion of electrode cost out of the entire battery cost is approximately 20%.^{44,45} If we consider only the cost of cell configuration, excluding the manufacturing and transportation cost, the electrode material cost rises to 50%. The material cost split, according to Tesla's report, in total is USD 195/kWh. The cost for an electrode is approximately USD 100/kWh, where a couple of dollars decrease may not seem critical. However, recent technology, such as grid energy storage, requires energy in terms of MWh or GWh. A couple of dollar saving for material can save more than thousands or millions of dollars for grid storage systems. Thereby, electrode material selection and design is important to reduce the overall cost. Carbon is a cheap resource that can be considered for energy storage systems. In addition, carbon derived from biomass or bio-waste provides more cost benefits.

1.4 Characterization of carbon

Characterization techniques are essential to understand the impact of carbon characteristics (e.g. structure, morphology, crystallinity, porosity) on electrochemical performance. In this section, analysis techniques for carbon characterization are briefly described. Furthermore, the correlation of carbon characterization results and the energy storage system is carefully discussed as well.

1.4.1 Electron microscopy analysis

The interaction of injected electrons with the specimen's nucleus or electron generates several signals, including backscattered electrons, secondary electrons, auger electrons, and characteristic X-rays. Scanning electron microscopy (SEM) detects the secondary electrons and obtain topological information from the sample. Furthermore, quantitative and qualitative elemental information of the sample is obtained from energy-dispersive X-ray spectroscopy (EDS), analysis attached to SEM. Various information can be anticipated from SEM images, such as the morphology of prepared carbon, macroporous information, weight percent of each element in the composite, size of material, interface of solid electrolyte and electrode, electrode information, and many others. The morphological difference of an electrode material before and after the charge/discharge cycles describes the stability of the material. The existence of macropore in a material indicates high permeability of electrolyte into the material, which improves the rate capability due to shorter ion diffusion length. Quantitative and qualitative information of the material is provided by the EDS analysis. In addition, the observation of solid state electrolyte and electrode interface provide valuable information such as wettability.

Transmission electron microscopy (TEM) collects the transmitted electrons. Atomic scale information of the specimen is easily collected from TEM due to the smaller wavelength of the initial electron beam.⁴⁶ The crystal information of sample, core/shell structure observation, and thickness of coated material are representative information collected from TEM. Advanced TEM, such as cryo-TEM, enabled the observation of in-situ lithium dendrite growth.

1.4.2 Structure analysis

X-ray diffraction (XRD) and Raman spectroscopy provide the fingerprint information of the material, especially for carbon materials.

The crystallographic information (structure and lattice parameters) are characterized by XRD, which is expressed by Bragg diffraction as:

$$2d \sin \theta = n\lambda$$

where d is the crystal plane spacing, θ is the Bragg diffraction angle, n is an integer, and λ is the initial X-ray wavelength. The samples could be measured in either powder or bulk form. The material information is identified by comparing the characteristic XRD pattern with standard XRD reference peaks. The lattice spacing of the material is calculated from the position of the 2θ peak.

For example, carbon materials, generally, exhibit (002) and (100) lattice characteristics. The size of each crystal is calculated by using Scherrer's equation:

$$d \text{ spacing} = \frac{k \lambda}{B \cos \theta}$$

where k is a constant value, λ is the wavelength of X-ray source (1.54 Å for Cu K α), θ is the Bragg diffraction angle, and B is the full width half maximum (FWHM) of the peak intensity at the measured 2θ position. The XRD analysis provides information if the tested material has sufficient interlayer spacing or secondary ion battery (e.g. 0.37 nm for sodium ion battery).

Raman spectroscopy provides a strong fingerprint of the material.⁴⁷ The vibrational energy of the material is measured by the energy difference between the incident and Raman light. Identification of the material, distinguishing polymorphic differences of samples, temperature study, structural disorder, crystal size, and etc. are obtained from Raman spectroscopy.⁴⁸⁻⁵⁰ For carbon materials, the D and G bands are typical peaks acquired from Raman.^{51,52} The G band, 1500 - 1600 cm⁻¹, originates from the vibration of two carbon atoms of the graphene unit cell. The D band, 1250 - 1350 cm⁻¹, originate from structural disorder coming from the edge and defects of carbon structure.⁴⁷ The D/G peak ratio is used to analyze the disorder in carbon materials or to compare the amount of defects among different carbon samples. According to Ferrari's 3-stage carbon theory, depending on the carbon stage, the D/G ratio either increase or decrease. The D/G ratio increase for amorphous carbon growth toward nanocrystalline graphite is attributed to the formation of sp² clusters.⁵³ Also the full width half maximum (FWHM) of the Raman peak gives crystallinity information about the carbon material, a wider FWHM indicates more amorphous characteristics.

1.4.3 Surface area analysis

The material surface area varies by the porosity and the size of carbon material. More porosity and smaller size of carbon increase the surface area, which can provide more storage sites. The macroporosity of carbon material is preferable in terms of shortening the diffusion length of ions and electrons. However, high surface area provides more SEI layer growth sites. The continuous growth and break of SEI layer accelerates the depletion of electrolyte, which cause serious safety issues such as lithium dendrite growth and thermal runaway. Thereby, precise measurement of the carbon surface area is essential.

A typical tool to measure the surface area of carbon material is the Brunauer-Emmett-Teller (BET) surface area measurement tool. The BET method uses a nitrogen gas isotherm adsorption-desorption test at liquid nitrogen temperature to measure the surface area and volume distribution of pores. From BET analysis, not only the surface area information is obtained but also the pore size information is obtained as well.

1.4.4 Conductivity analysis

The material conductivity is important for electrochemical performance. Many battery applications, such as electric vehicles, require high power. For high power devices, the charge/discharge rate is fast (C-rates higher than 4C).⁵⁴ At higher rate, the charge/discharge time is short. A material with good conductivity will perform higher capacity at higher C-rate than a material with poor conductivity. Thereby, the measurement of material conductivity is essential to understand the electrochemical performance of the cell.

Electrochemical Impedance Spectroscopy (EIS) measurement provides the ionic resistance information between current collector/electrode and electrode/electrolyte interface.²⁶ The comparison of the easiness of ion diffusion into different material is measurable. Galvanostatic Intermittent Titration Technique (GITT) measurement provides the electric conductivity information. A constant current is applied and not-applied during the process. The voltage drop during the rest period (current off) is related to the electrical resistance of the material. The electrical conductivity of different material can be compared by observing the voltage drop of each sample. Smaller voltage drop of a sample indicates higher electric conductivity.

1.4.5 Thermal analysis

Thermal gravimetric analysis (TGA) is utilized to study the decomposition temperature, phase transitions, chemisorptions, mass portion of a composite, and yield of material after carbonization. TGA simply measure the mass of sample during the temperature changes at specific gas atmosphere. The thermal stability of a certain material can be measured by TGA. No mass change is observed if the material is stable at the specific temperature range. The weight portion of the composite can be measured by TGA. For a carbon/metal composite, carbon is generally burned out at high temperature under air atmosphere.⁵⁵ By reading the remaining weight after a

TGA run, we can back calculate the weight portion of carbon and metal. The sulfur loading inside the carbon scaffold is measurable as well.⁵⁶

1.5 Dissertation structure

This dissertation aims to explore the requirements of energy storage systems and to meet the needs by understanding and utilizing the characteristics of carbon material. Recent technology advancement requires next generation energy storage systems with benefits in cost, sustainability, and performance. Each chapter of this dissertation aims to resolve the requirement of next generation battery systems. The dissertation is outlined as:

Chapter 1 gives a general introduction to carbon and brief information about different types of carbon materials. In addition, carbon characteristics that attract research on carbon for energy storage systems are introduced. The characterization tools to analyze carbon characteristics are briefly summarized as well.

Chapter 2 explains the application of carbon material in energy storage devices. For further understanding, the basic principles of lithium ion battery and terms used in battery are discussed.

Chapter 3 discuss about a plausible method to meet the cost requirement of the next generation energy storage systems. An economical and ecological benign dry autoclave method to prepare carbon is proposed for a lithium ion battery. A spherical carbon is formed from coffee oil and the performance of such carbon showed a good cycle and structure stability.

Chapter 4 studies the impact of temperature on carbon structure. As the carbonization temperature increases, carbon shows a more graphitic structure. Each carbon sample was applied in sodium ion battery. P1000 showed the highest capacity value due to the combination of sodium intercalation, defect sites, and pseudocapacitance sodium storage mechanism.

Chapter 5 suggest a plausible method to resolve the polysulfide shuttling effect in a lithium-sulfur battery. The structure of pistachio derived carbon exhibits macro-channels and micropores. The macro-channels structure increase sulfur loading and shorten the ion diffusion length. Physical restriction of polysulfide shuttling is realized by the micropores of pistachio derived carbon. Further synergic effect on restricting polysulfide shuttling was realized by MnO₂ decoration on pistachio carbon. MnO₂ decoration further suppress polysulfide shuttling by chemical reaction and formation of thiosulfate on MnO₂ surface.

In chapter 6, summary and future outlook of the research are described, including carbon material application in lithium metal batteries.

1.6 References

- 1 Lide, D. R. *CRC handbook of chemistry and physics: a ready-reference book of chemical and physical data*. (CRC press, 1995).
- 2 Haley, M. M. Carbon allotropes: On the road to carbyne. *Nat Chem* (2010) **2**, 912.
- 3 Pandolfo, A. & Hollenkamp, A. Carbon properties and their role in supercapacitors. *J Power Sources* (2006) **157**, 11-27.
- 4 Bechtel, A. *et al.* Biomarker and carbon isotope variation in coal and fossil wood of Central Europe through the Cenozoic. *Palaeogeography, Palaeoclimatology, Palaeoecology* (2008) **262**, 166-175.
- 5 Griffin, J. J. & Goldberg, E. D. Morphologies and origin of elemental carbon in the environment. *Science* (1979) **206**, 563-565.
- 6 Kim, K. *et al.* Tailored carbon anodes derived from biomass for sodium-ion storage. *Acs Sustain. Chem. Eng.* (2017) **5**, 8720-8728.
- 7 Thompson, B. C. & Fréchet, J. M. Polymer–fullerene composite solar cells. *Angewandte chemie international edition* (2008) **47**, 58-77.
- 8 Brabec, C. J. *et al.* Polymer–fullerene bulk-heterojunction solar cells. *Adv. Mater.* (2010) **22**, 3839-3856.
- 9 Ulbricht, R. *et al.* Transparent carbon nanotube sheets as 3-D charge collectors in organic solar cells. *Solar Energy Materials and Solar Cells* (2007) **91**, 416-419.
- 10 Cui, L.-F., Hu, L., Choi, J. W. & Cui, Y. Light-weight free-standing carbon nanotube-silicon films for anodes of lithium ion batteries. *Acs Nano* (2010) **4**, 3671-3678.
- 11 Kim, J. H. *et al.* Encapsulation of S/SWNT with PANI web for enhanced rate and cycle performance in lithium sulfur batteries. *Sci. Rep.* (2015) **5**, 8946.
- 12 Lotfabad, E. M. *et al.* High-density sodium and lithium ion battery anodes from banana peels. *Acs Nano* (2014) **8**, 7115-7129.
- 13 Pierson, H. O. *Handbook of carbon, graphite, diamonds and fullerenes: processing, properties and applications*. (William Andrew, 2012).
- 14 Wen, Y. *et al.* Expanded graphite as superior anode for sodium-ion batteries. *Nat. Commun.* (2014) **5**, 4033.
- 15 Setton, R. The graphite intercalation compounds: their uses in industry and chemistry. *Synthetic Met* (1988) **23**, 467-473.
- 16 Cho, M. H., Ju, J., Kim, S. J. & Jang, H. Tribological properties of solid lubricants (graphite, Sb₂S₃, MoS₂) for automotive brake friction materials. *Wear* (2006) **260**, 855-860.
- 17 Yucheng, W. & Zhengyi, F. Study of temperature field in spark plasma sintering. *Materials Science and Engineering: B* (2002) **90**, 34-37.
- 18 Li, X., Rigaud, M. & Palco, S. Oxidation Kinetics of Graphite Phase in Magnesia-Carbon Refractories. *Journal of the American Ceramic Society* (1995) **78**, 965-971.
- 19 Iijima, S. Helical microtubules of graphitic carbon. *Nature* (1991) **354**, 56.
- 20 Hamada, N., Sawada, S.-i. & Oshiyama, A. New one-dimensional conductors: graphitic microtubules. *Phys Rev Lett* (1992) **68**, 1579.

- 21 Mao, W. *et al.* In-situ synthesis of MnO₂@ CNT microsphere composites with enhanced electrochemical performances for lithium-ion batteries. *J Power Sources* (2016) **310**, 54-60.
- 22 Bianco, A., Kostarelos, K. & Prato, M. Applications of carbon nanotubes in drug delivery. *Current opinion in chemical biology* (2005) **9**, 674-679.
- 23 Franklin, A. D. *et al.* Sub-10 nm carbon nanotube transistor. *Nano Lett.* (2012) **12**, 758-762.
- 24 Franklin, R. E. Crystallite growth in graphitizing and non-graphitizing carbons. *Proc. R. Soc. Lond. A* (1951) **209**, 196-218.
- 25 Franklin, R. E. Homogeneous and heterogeneous graphitization of carbon. *Nature* (1956) **177**, 239.
- 26 Kim, K., Kim, P. J. H., Youngblood, J. P. & Pol, V. G. Surface Functionalization of Carbon Architecture with Nano-MnO₂ for Effective Polysulfide Confinement in Lithium-Sulfur Batteries. *Chemsuschem* (2018).
- 27 Li, W., Chen, M. & Wang, C. Spherical hard carbon prepared from potato starch using as anode material for Li-ion batteries. *Mater Lett* (2011) **65**, 3368-3370.
- 28 Saravanan, K. & Kalaiselvi, N. Nitrogen containing bio-carbon as a potential anode for lithium batteries. *Carbon* (2015) **81**, 43-53.
- 29 Wu, L., Buchholz, D., Vaalma, C., Giffin, G. A. & Passerini, S. Apple-Biowaste-Derived Hard Carbon as a Powerful Anode Material for Na-Ion Batteries. *Chemelectrochem* (2016) **3**, 292-298.
- 30 Hou, H., Qiu, X., Wei, W., Zhang, Y. & Ji, X. Carbon Anode Materials for Advanced Sodium-Ion Batteries. *Adv. Energy Mater.* (2017) **7**, 1602898.
- 31 Zhang, J. *et al.* Biomass derived activated carbon with 3D connected architecture for rechargeable lithium– sulfur batteries. *Electrochim. Acta* (2014) **116**, 146-151.
- 32 Chen, F., Yang, J., Bai, T., Long, B. & Zhou, X. Biomass waste-derived honeycomb-like nitrogen and oxygen dual-doped porous carbon for high performance lithium-sulfur batteries. *Electrochim. Acta* (2016) **192**, 99-109.
- 33 Zheng, G. *et al.* Interconnected hollow carbon nanospheres for stable lithium metal anodes. *Nature nanotechnology* (2014) **9**, 618.
- 34 Buiel, E. & Dahn, J. Li-insertion in hard carbon anode materials for Li-ion batteries. *Electrochim. Acta* (1999) **45**, 121-130.
- 35 Song, R. *et al.* Hierarchical porous carbon nanosheets and their favorable high-rate performance in lithium ion batteries. *J Mater Chem* (2012) **22**, 12369-12374.
- 36 Hu, Y. S. *et al.* Synthesis of hierarchically porous carbon monoliths with highly ordered microstructure and their application in rechargeable lithium batteries with high-rate capability. *Adv Funct Mater* (2007) **17**, 1873-1878.
- 37 Lee, J. T. *et al.* Sulfur-Infiltrated Micro-and Mesoporous Silicon Carbide-Derived Carbon Cathode for High-Performance Lithium Sulfur Batteries. *Adv. Mater.* (2013) **25**, 4573-4579.
- 38 Bacon, G. The interlayer spacing of graphite. *Acta Crystallogr* (1951) **4**, 558-561.
- 39 Dahbi, M. *et al.* Synthesis of hard carbon from argan shells for Na-ion batteries. *J. Mater. Chem. A* (2017) **5**, 9917-9928.
- 40 Jian, Z., Xing, Z., Bommier, C., Li, Z. & Ji, X. Hard carbon microspheres: potassium-ion anode versus sodium-ion anode. *Adv. Energy Mater.* (2016) **6**, 1501874.

- 41 Li, X. *et al.* An ultrafast rechargeable lithium metal battery. *J. Mater. Chem. A* (2018) **6**, 15517-15522.
- 42 Shen, X., Liu, H., Cheng, X.-B., Yan, C. & Huang, J.-Q. Beyond lithium ion batteries: Higher energy density battery systems based on lithium metal anodes. *Energy Storage Mater* (2018) **12**, 161-175.
- 43 Cui, L.-F., Yang, Y., Hsu, C.-M. & Cui, Y. Carbon– silicon core– shell nanowires as high capacity electrode for lithium ion batteries. *Nano Lett.* (2009) **9**, 3370-3374.
- 44 Upadhyay, A. Tesla's Powerwall & Battery Costs Disruption. (2015).
- 45 Archives, N. The cost components of a lithium ion battery. (2016).
- 46 Williams, D. B. & Carter, C. B. in *Transmission electron microscopy* 3-17 (Springer, 1996).
- 47 Ferrari, A. C. *et al.* Raman spectrum of graphene and graphene layers. *Phys Rev Lett* (2006) **97**, 187401.
- 48 Hassan, A., Torell, L., Börjesson, L. & Doweidar, H. Structural changes of B₂O₃ through the liquid-glass transition range: A Raman-scattering study. *Phys Rev B* (1992) **45**, 12797.
- 49 Quiñones, R., Brown, R. T., Searls, N. & Richards-Waugh, L. Study of polymorphism using patterned self-assembled monolayers approach on metal substrates. *Appl Surf Sci* (2018) **427**, 97-105.
- 50 Ni, Z. H. *et al.* Probing charged impurities in suspended graphene using Raman spectroscopy. *Acs Nano* (2009) **3**, 569-574.
- 51 Dresselhaus, M. S., Jorio, A., Hofmann, M., Dresselhaus, G. & Saito, R. Perspectives on carbon nanotubes and graphene Raman spectroscopy. *Nano Lett.* (2010) **10**, 751-758.
- 52 Chhowalla, M., Ferrari, A., Robertson, J. & Amaratunga, G. Evolution of sp² bonding with deposition temperature in tetrahedral amorphous carbon studied by Raman spectroscopy. *Appl Phys Lett* (2000) **76**, 1419-1421.
- 53 Ferrari, A. C. & Robertson, J. Interpretation of Raman spectra of disordered and amorphous carbon. *Phys Rev B* (2000) **61**, 14095.
- 54 Wang, D. W., Li, F., Liu, M., Lu, G. Q. & Cheng, H. M. 3D aperiodic hierarchical porous graphitic carbon material for high-rate electrochemical capacitive energy storage. *Angewandte Chemie* (2008) **120**, 379-382.
- 55 Yue, H. *et al.* Ultra-thick porous films of graphene-encapsulated silicon nanoparticles as flexible anodes for lithium ion batteries. *Electrochim. Acta* (2015) **174**, 688-695.
- 56 Vu, D.-L., Seo, J.-S., Lee, H.-Y. & Lee, J.-W. Activated carbon with hierarchical micro–mesoporous structure obtained from rice husk and its application for lithium–sulfur batteries. *Rsc Adv* (2017) **7**, 4144-4151.

2. CARBON-BASED MATERIALS FOR ENERGY STORAGE

2.1 Introduction of energy storage systems

The conventional energy systems have rapidly advanced with the introduction of fossil fuel energy. However, the limitation of fossil fuels availability and the economical- / ecological-issues associated with fossil fuels brought worldwide interest to low-cost, environmental friendly, abundant, and high-performance energy storage system (ESS).

ESS stores energy during off-peak and provides energy during peak demand period. Figure 2.1 describes the working principle of ESS during different periods of the day. These ESS could reduce the cost of generating energy during peak periods and improve the energy quality and reliability. Several technologies have been introduced, such as chemical storage (biofuel, hydrogen), mechanical storage (compressed-air, pumped-storage), thermal storage (sensible heat thermal energy storage), and electrochemical storage (rechargeable battery, supercapacitor).¹ Some of these techniques are introduced in this section.

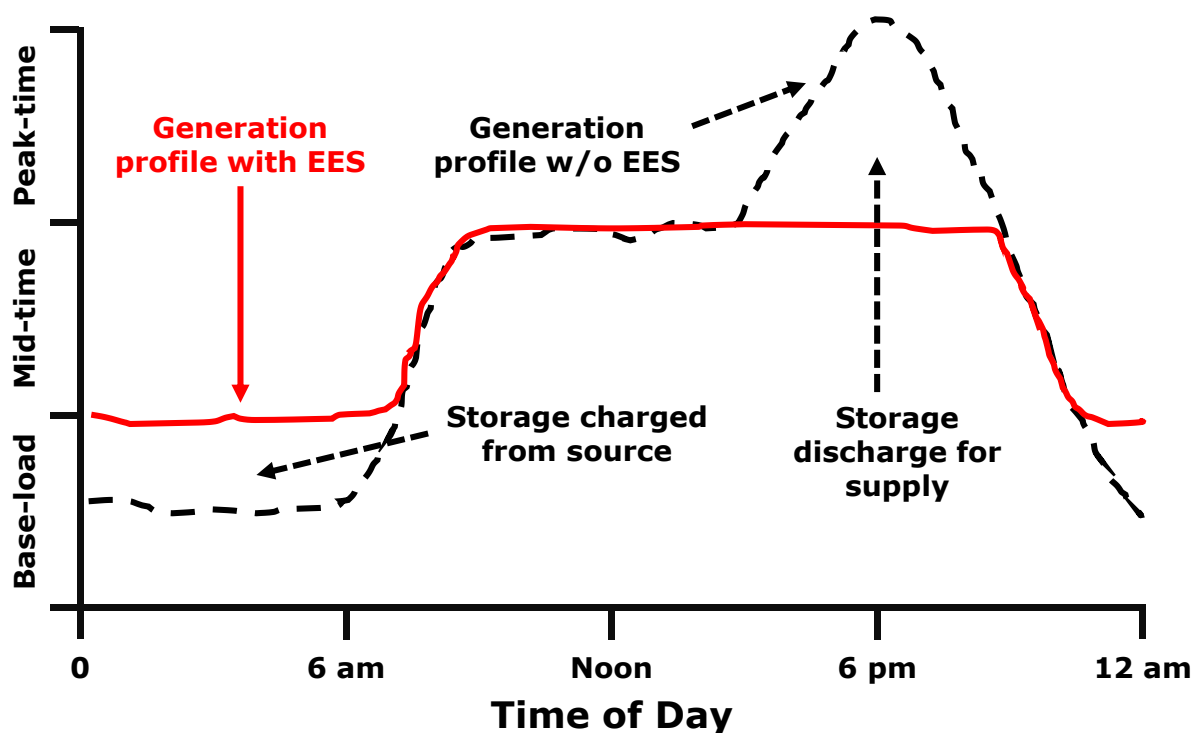


Figure 2.1 The load profile of energy storage system in terms of system demand (MW) vs. time of day.

The pumped-hydro storage (PHS) uses the potential energy of water.^{2,3} Water gains acceleration by falling from a high location, to propel the turbine, which generates electricity. PHS stores water into the upper reservoir during off-peak period and releases water during peak-demand to a turbine to generate necessary energy. As the turbine spins, electricity is generated and provided to area that requires energy. The thermal energy storage (TES) generates electricity by flow of hot or cold air through a heat engine.³ Hydrogen storage provides the highest energy density by weight, but exhibits lowest energy density by volume.⁴ One of the issues for hydrogen storage is the chance of explosion. To resolve the issue, high pressure and chemical compounds are proposed to provide a safe, compact, and reliable hydrogen storage system.

Despite the benefits of aforementioned storage systems, the physical dimensions issue, long construction time, high construction cost, and the requirement of sophisticated techniques calls for energy storage systems with high performance, reliable cost, facile construction, and small physical dimensions. Electrochemical energy storage (EES) is a valuable system to meet the requirements and to use in all power systems, including transportation and power generation. Table 2.1 and Table 2.2 compare the performance and characteristics of each storage system. Although the power rating and life-time of EES is lower than other storage systems, EES had advantages over other systems, including faster energy distribution, longer cycle life, higher efficiency, and cheaper cost. The EES energy (battery) and power (capacitor) density performance is higher than other storage systems. These characteristics make EES suitable for back-up power supply, portable electronic devices, electric vehicles, and many other applications.

Table 2.1 The comparison of various energy storage systems properties.

Technology	Power Rating (MW)	Discharge Time	Cycling capacity	Life Time (years)
Pumped-Hydro	100 – 5000	1 – 24 hrs	20,000 – 50,000	40 – 60
Compressed-Air	5 – 300	1 – 24 hrs	10,000 – 30,000	20 – 40
High-temperature Thermal	0 – 60	1 – 24 hrs	N/A	5 – 15
Super-Capacitor	0 – 0.3	Milliseconds – 60 mins	100,000 +	20
Lithium-Ion Battery	0 – 0.1	Minutes – Hours	1,000 – 10,000	5 – 15

Table 2.2 The performance and cost of various energy storage systems.

Technology	Energy Density (Wh / kg)	Power Density (W / kg)	Round Trip Efficiency (%)	Cost (\$ / kW)
Pumped-Hydro	0.5 – 1.5	N/A	65 – 80	600 – 2000
Compressed-Air	30 – 60	0.5 – 2	70 – 85	400 – 800
High-temperature Thermal	80 – 200	N/A	N/A	30 – 60
Super-Capacitor	2 – 5	500 – 10,000	75 – 90	100 – 300
Lithium-Ion Battery	75 – 200	150 – 315	85 – 100	175 – 4000

2.1.1 Introduction to lithium ion battery

A battery is defined as ‘a device comprising one or more electrochemical cells with external circuit to supply power to electrical applications’.⁵ A secondary battery is a cell that goes through an electrochemical reversible redox reaction. The original charge condition can be restored by controlling the flow of current direction (charge and discharge flows, oppositely). During the cell operation (discharge process), the chemical energy is converted into electric energy. For a lithium

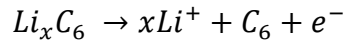
ion battery (LIB), the oxidized anode releases electrons to an external circuit and releases lithium ions to the internal circuit. A reductive reaction occurs on cathode as both ions and electrons travel to the cathode. The redox reaction and current flow occurs reversely during the charge process of the battery. Among various rechargeable batteries, including lithium ion batteries (LIB), nickel-metal hydride, and lead acid batteries, LIB has been under the spotlight for its high energy density, long cycle life, high capacity, and flexible cell design.

LIB is mainly composed of cathode, anode, separator, and electrolyte. Li-containing metal oxide layered structures (LiCoO_2 , LiFePO_4 , etc.) or tunnel structures (LiMn_2O_4) are generally used as cathode materials.⁶ Anode materials are categorized into 3 types, including insertion-type (graphite, amorphous carbon), alloying-type (Si, Sn, Al), and conversion-type (Fe_2O_3) materials. Most electrolytes are inorganic lithium salt dissolved in organic solvents. A separator is placed between anode and cathode to provide ionic permeability and restrict internal electron transport.

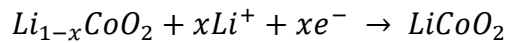
The schematic of LIB charge/discharge process is illustrated in figure 2.2. In a typical LIB cell, lithium cobalt oxide (LiCoO_2 , in brief LCO) and graphite (C) are used as cathode and anode, respectively. The redox reaction of LIB can be written as:

<Discharge process>

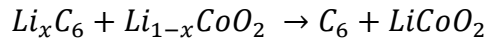
Negative electrode: anodic reaction, oxidation



Positive electrode: cathodic reaction, reduction

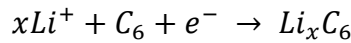


The overall reaction

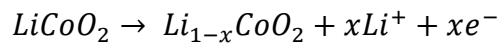


<Charge process>

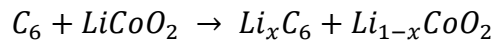
Negative electrode: cathode reaction, reduction



Positive electrode: anodic reaction, oxidation



The overall reaction



As technologies advances into large applications, such as for electric vehicles, new design criteria (e.g. cost, performance, different battery system) become essential. Much research on electrode material modification, electrolyte modification, and separator has been reported for improving the performance of LIB. Next generation battery systems, such as sodium ion battery, lithium-sulfur battery, and lithium-metal battery, have attracted significant interest for their cost and high capacity benefits. As described in Chapter 1.3, carbon-based materials exhibit characteristics which are favored for battery application. The next two sections describe the basic terms used in batteries and general introduction of carbon-based material application in energy storage devices.

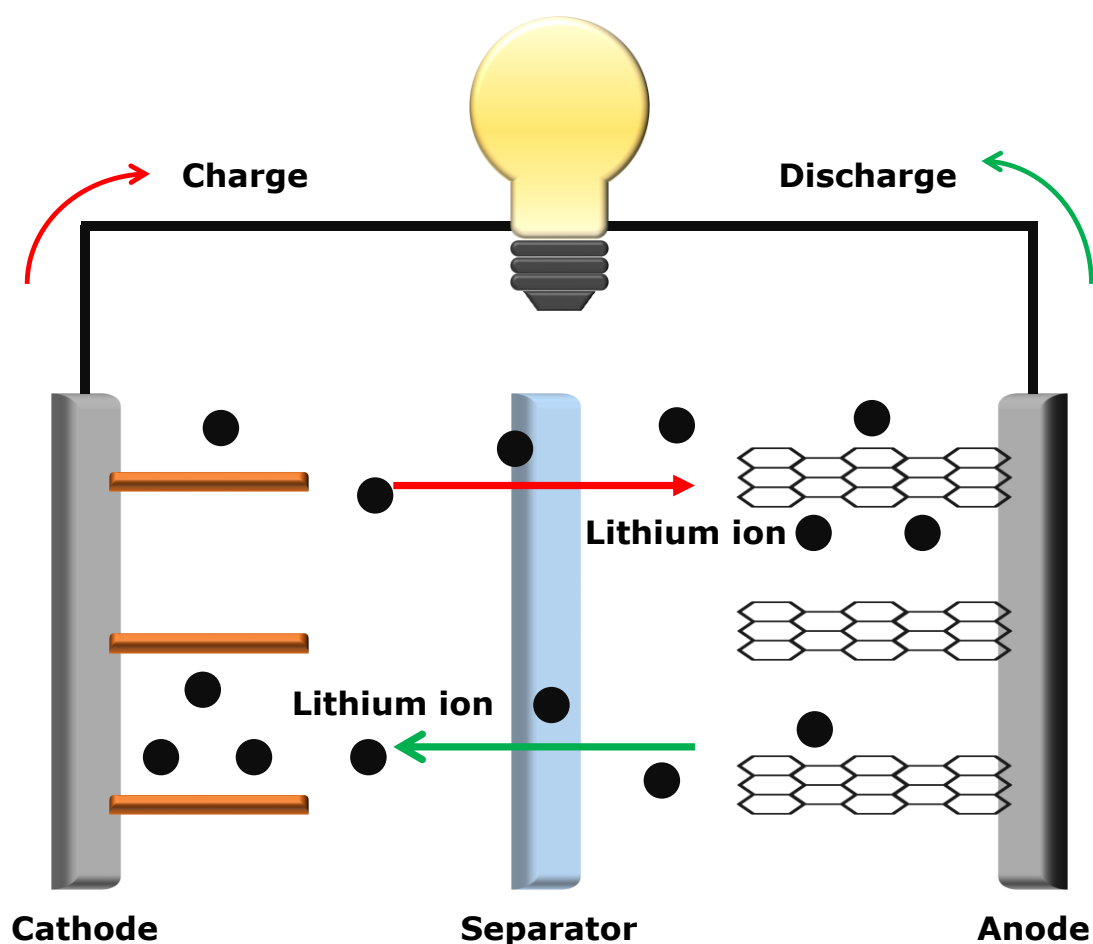


Figure 2.2 The typical LIB cell configuration and components. The electron and lithium ion travel directions during charge and discharge process are illustrated as well.

2.2 Definition of terms

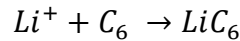
This section explains the basic terms that are frequently used in the battery field.

2.2.1 Capacity

Capacity is an amount of energy that the device can deliver in a single discharge. The specific capacity is an amount of charge stored per unit mass of materials, expressed in terms of mAh g⁻¹. The specific capacity is defined as:

$$C_{electrode} \text{ (Specific Capacity)} = \frac{z \times F}{3.6 \times M} \text{ mAh g}^{-1}$$

where z is the amount of electric charge transferred per mole of active material; F is the Faraday constant (96485 C mol⁻¹); and M is the molecular mass of active material. For example, graphite specific capacity calculation starts from the lithium insertion reaction as:



The amount of electric charge transferred per mole z is 1 and the molecular mass M of the storage material is 72 g mol⁻¹. Applying these numbers to above specific capacity equation gives a graphite specific capacity in LIB as 372 mAh g⁻¹.

The specific capacity of a full-cell composed of cathode and anode is defined as:

$$C_{full\ cell} = \frac{1}{\frac{1}{C_{cathode}} + \frac{1}{C_{anode}}} \text{ (mAh g}^{-1}\text{)}$$

2.2.2 Voltage

Voltage is an electro-potential difference between anode and cathode electrode.⁷ In a battery, the open circuit voltage (OCV) is simply a potential difference between anode and cathode material. A higher potential window is preferred, as the energy density and power density are proportional to cell voltage.

2.2.3 Energy and Power Density

Energy and power density are conventional terms used and considered for a commercial battery. Energy density explains how much energy the battery can deliver. Energy density is determined from the cell capacity and cell voltage as:

$$W_{cell} = E^o \times C_{cell} \text{ (Wh kg}^{-1} = V \cdot Ah \text{ kg}^{-1}\text{)}$$

Power density shows the power output per unit volume. In a battery, power density is a product of cell potential and current. Power density is related to C-rate, which is related to the charge/discharge rate. C-rate, $x\text{C}$, is defined as each charge and discharge is completed over $1/x$ hours. For example, if each charge and discharge completes over 5 hours, the C-rate is 0.2 C .

2.2.4 Coulombic efficiency and cycle life

Coulombic efficiency (CE) depicts the reversibility of a cell during charge and discharge cycles. It is simply described as discharge capacity divided by charge capacity. CE is related to the chemical reaction of electrode materials and electrolyte occurring on either cathode or anode electrode. The reaction of electrode materials and electrolyte forms a solid electrolyte interphase (SEI) layer on the electrode. This SEI layer formation is an irreversible reaction. Thereby, more reaction between electrode and electrolyte forms a thicker SEI layer and results in lower CE. Figure 2.3 illustrates an example of a material with 50% CE. During lithiation process, 50% of lithium ions are consumed to form a SEI layer on electrode surface. Only 50% of initial lithium ions from the counter-electrode travel back to the original electrode during de-lithiation process.

Cycle life is defined as a number of complete charge/discharge cycles of the battery before the cycle retention drops below 80% of its initial capacity. The cycle life varies depending on the depth of discharge (DoD) and the temperature of the storage environment.

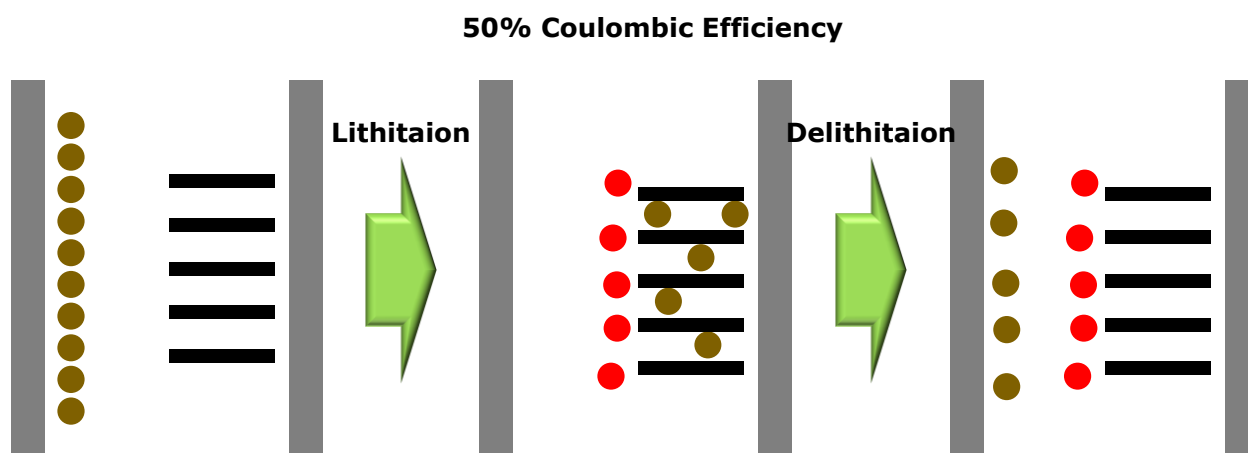


Figure 2.3 Illustration of Coulombic efficiency.

2.3 Carbon in energy storage systems

Carbon, the fourth most abundant element by mass, has been used as an energy source throughout the development of human history. Numerous examples are found around us: wood as an energy source starting BC 2000, coal coke paved the way for industrialization in the 17th century, fossil fuels and biofuels application, and even CO₂ is being suggested as energy source.⁸ The characteristics of carbon materials, including high conductivity, good electrochemical reversibility, relatively low cost, low self-discharge rate, and low potential, boosted its application in not only lithium ion batteries but also next generation energy storage systems (ESS). In this section, carbon application in ESS is briefly introduced.

The first commercialized battery used graphite as an anode material. CNT are emerging as transparent and electrically conductive films for the display industry, solar industry, and many others.⁹⁻¹¹ Hard carbon materials are used in a sodium ion battery for its sufficient interlayer spacing (> 0.37 nm).

The polysulfide shuttling effect is a critical issue for the lithium-sulfur battery. Insoluble low order polysulfide sitting on a lithium anode decreases the CE and overall capacity during repeated cycles. Also, the insulating characteristics of sulfur are another issue. To resolve the aforementioned issues, carbon materials are utilized as a sulfur reservoir. The conductive property of carbon provides a conductive path and the micropores in the carbon structure provide physical trapping sites for polysulfides.

Lithium metal has attracted huge interest for its low density, cheap cost, and high specific capacity. However, growth of lithium dendrite during repeated cycles has caused serious issues such as thermal runaway and internal short circuit. Carbon materials are utilized to resolve the dendrite issue by lowering local current density and mechanically blocking dendrite penetration.^{12,13} Kim et al., reported a separator modified with graphite to resolve the lithium dendrite issue.¹⁴ The current density reaching the lithium counter-electrode is reduced due to lithium insertion in graphite. Local current density applied to the counter-electrode is reduced and the performance of the lithium metal battery is improved.

The following chapters describe the effort of my Ph.D. study on resolving issues of each ESS by carbon materials.

2.4 References

- 1 Wikipedia. Energy storage. (2015).
- 2 Rehman, S., Al-Hadhrani, L. M. & Alam, M. M. Pumped hydro energy storage system: A technological review. *Renewable and Sustainable Energy Reviews* (2015) **44**, 586-598.
- 3 Cabeza, L. F. *Advances in thermal energy storage systems: Methods and applications*. (Elsevier, 2014).
- 4 Hirose, K. *Handbook of hydrogen storage: new materials for future energy storage*. (John Wiley & Sons, 2010).
- 5 Crompton, T. P. *Battery reference book*. (Elsevier, 2000).
- 6 Etacheri, V., Marom, R., Elazari, R., Salitra, G. & Aurbach, D. Challenges in the development of advanced Li-ion batteries: a review. *Energ Environ Sci* (2011) **4**, 3243-3262.
- 7 Wikipedia. Voltage. (2019).
- 8 Jiang, K. *et al.* Isolated Ni single atoms in graphene nanosheets for high-performance CO₂ reduction. *Energ Environ Sci* (2018) **11**, 893-903.
- 9 Pasquier, A. D., Unalan, H. E., Kanwal, A., Miller, S. & Chhowalla, M. Conducting and transparent single-wall carbon nanotube electrodes for polymer-fullerene solar cells. *Appl Phys Lett* (2005) **87**, 203511.
- 10 Kaempgen, M. & Roth, S. Transparent and flexible carbon nanotube/polyaniline pH sensors. *Journal of Electroanalytical Chemistry* (2006) **586**, 72-76.
- 11 Fu, W., Liu, L., Jiang, K., Li, Q. & Fan, S. Super-aligned carbon nanotube films as aligning layers and transparent electrodes for liquid crystal displays. *Carbon* (2010) **48**, 1876-1879.
- 12 Wang, H. *et al.* Wrinkled graphene cages as hosts for high capacity Li metal anodes shown by cryogenic electron microscopy. *Nano Lett.* (2019).
- 13 Liu, Y. *et al.* An Ultrastrong Double-Layer Nanodiamond Interface for Stable Lithium Metal Anodes. *Joule* (2018).
- 14 Kim, P. J. & Pol, V. G. High Performance Lithium Metal Batteries Enabled by Surface Tailoring of Polypropylene Separator with a Polydopamine/Graphene Layer. *Adv. Energy Mater.* (2018) **8**, 1802665.

3. DRY AUTOCLAVE METHOD DERIVED CARBON MATERIAL FOR LITHIUM ION BATTERY

The scientific hypothesis was made by K.Kim and executed with the help of R. Adams, P. J. Kim, Prof. J. Youngblood, and Prof. V. Pol. Most of the experimental and characterization work was performed by K.Kim. A. Arora conducted the dry autoclave process. Data analysis was conducted by K.Kim and discussion was made with P.J. Kim. Manuscript writing was performed by K. Kim and revised by R. Adams, P. J. Kim, Prof. J. Youngblood, and Prof. V. Pol.

The following chapter contains content reproduced with permission from K. Kim, R. Adams, P. J. Kim, A. Arora, E. Martinez, J. P. Youngblood, and V. G. Pol., Li-ion storage in an amorphous, solid, spheroidal carbon anode produced by dry-autoclaving of coffee oil., *Carbon* **2018**, 133, 62 – 68. Copyright 2018 Elsevier Publisher.

3.1 Introduction

Since their development in the early 1990s, lithium ion batteries (LIBs) have dominated the rechargeable battery market, using graphite as anode material due to its moderate capacity (372 mAh g⁻¹), high voltage window, and long cycle life.¹ To meet the increasing worldwide demand for improved performance and efficient energy sources, research in developing safer, high energy and power density batteries is increasing. However, global concerns on environmental issues requires the energy field to match the needs by unveiling eco-friendly material, process and cost effective methods.²

Due to its high structural stability, low cost, and reasonable capacity, carbon is an attractive anode material for both LIBs and sodium-ion batteries (SIBs).³ Since the introduction of amorphous carbon as LIB anode material, many researches have focused on the effects of precursor, synthesis method, and carbon structuring on Li storage performance. In this section, the unique dry-autoclave method is introduced and the conventional carbon synthesis methods are briefly discussed as well.

3.1.1 Conventional carbon preparation methods

Porous carbon films, carbon nanomaterials (short ion/electron diffusion length), and carbon material derived from sustainable sources (e.g. biomass) synthesis method have been reported to meet the needs of each application. Laser ablation,⁴ template-based synthesis,^{5,6} combustion method,⁷ direct pyrolysis⁸, hydrothermal,^{9,10} solvothermal,^{11,12} microwave heating,^{13,14} and many other synthesis methods have been proposed.^{15,16} However, these strategies involve environmental issues, long processing times, and sophisticated techniques which hinders the use in large scale systems.¹⁷

3.1.2 Dry-autoclave method

Dry autoclaving¹⁷ is a simple, solvent- and catalyst- free method that avoids these issues. In dry autoclave method, unlike hydrothermal or solvothermal method, the chemical reactions happens without solvents. As temperature reaches the reaction temperature, different phases are formed depending on the evaporation temperature of the element. Subsequently, during cooling process, solid nucleates and grow forming final product.

Previous studies on functional sulfides,^{18,19} phosphides,²⁰ nitrides,²¹ carbides^{22,23}, mesitylene derived carbon spheres²⁴, corn oil²⁵, and olive oil²⁶ showed that dry autoclave method successfully produced a variety of organic and inorganic materials without catalyst. Recent reports on carbon derived from pomelo peels,²⁷ fungi,²⁸ pollen,²⁹ and pistachio shells³⁰ demonstrated the global emphasis on the development of sustainable carbon materials. Herein, we utilize coffee oil as a carbon precursor as it is an unused waste product of coffee production.^{31,32} As global consumption of coffee increases every year, reaching 9,300,000 metric tons in 2016, more coffee oil can be generated every year.³³ This fits the theme of environmental sustainability by reusing waste product for an ‘upcycled’ electrochemical application. Coffee oil mainly consists carbon, hydrogen, and oxygen, which enables the decomposition of the precursor at the elevated temperature (700 °C) and generates autogenic pressure. These chemical and physical factors transform the liquid precursor into solid carbon upon cooling. As a result, spherical and dumbbell-shaped carbon particles evolve from coffee oil in a simple, solvent free, and catalyst free dry autoclaving method. A possible formation mechanism of the carbon morphology by understanding the components of coffee oil (C, H, and O) is also discussed. Promising electrochemical results for both lithium ion

and sodium ion batteries are presented and discussed. To the best of our knowledge, this is the foremost study utilizing the dry autoclave synthesis method for production of spheroidal carbons from coffee oil as a Li-ion anode electrode.

3.2 Experimental

3.2.1 Synthesis of spheroidal carbon particles

Commercial coffee oil (Sigma Aldrich, roasted / natural Coffee oil from Arabica) was used as a carbon precursor. To synthesize the anode material, 0.9 g of coffee oil was sealed inside a 1/2" stainless steel Swagelok chamber, which was assembled and sealed inside a glovebox under argon gas atmosphere. The Swagelok reactor was placed at the center of a tube furnace for uniform heating. The furnace was heated to 700 °C with a ramp rate of 30 °C min⁻¹ and maintained for 20 mins. After cooling the Swagelok reactor, it was opened and yielded 45% weight of solid carbon product. The obtained carbon sample was further heat treated to 900 °C with a ramping rate of 5 °C min⁻¹ and held for 2 hours to remove possible organic moieties and improve product purity.

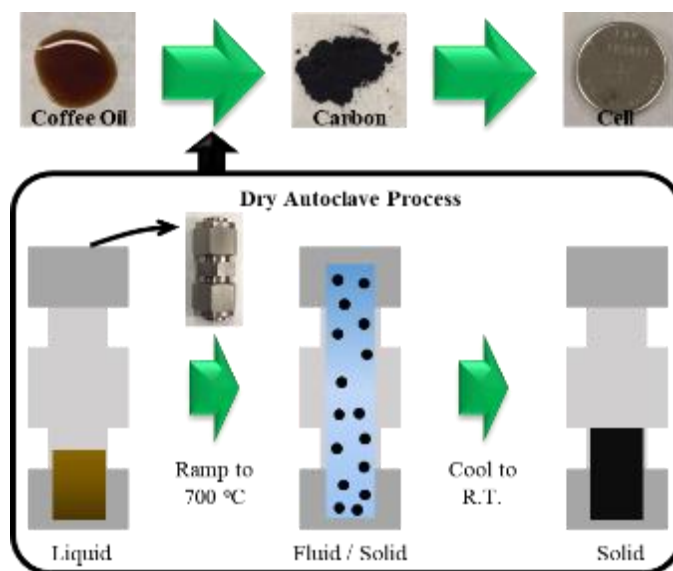


Figure 3.1 Schematic diagram demonstrating coffee oil derived spheroidal carbon.

The schematic diagram (Figure 3.1) shows the dry autoclaving process to produce spheroidal carbon anode from a coffee oil precursor. The box shows how coffee oil converts to amorphous carbon via critical interactions between the molecules during dry autoclaving.

3.2.2 Materials characterization

To image the morphologies and microstructure of dry autoclave derived carbon, scanning electron microscope (SEM, FEI quanta 3D FED dual-beam at 10 kV) was utilized. N₂ adsorption-desorption equipment (Qunatachrome Nova 2200e) was utilized to determine the Brunauer-Emmett-Teller (BET) surface area and pore volume. The crystallographic nature of coffee oil derived carbon sphere was studied using Raman spectroscopy (Renishaw, InVia Raman microscope) and X-ray diffraction (XRD, Rigaku at 40 kV and 44 mA). The inter-planar spacing $d(002)$ and the lateral size (L_a) was calculated by Bragg's law (Eqn. 1) and Scherrer's equation by analyzing the (002) and (100) peaks from XRD (Eqn. 2).

$$d = \frac{\lambda}{\sin \theta} \quad (1)$$

$$L = \frac{K \lambda}{\beta \cos \theta} \quad (2)$$

β is the full width half maximum (FWHM) of the diffraction peak and K is a dimensionless shape factor, which is 1.84 for lateral size and 0.91 for stacking height calculation.

The tap density was measured by placing a weighed quantity of spheroidal carbon in a graduated cylinder and measuring the volume after application of 10,000 auto taps (Auto tap, Quantachrome).

3.2.3 Electrochemical characterization

Electrode slurries comprising 80 wt.% spheroidal carbon, 10 wt.% polyvinylidene fluoride (PVDF, MTI), 10 wt.% conductive carbon (Timcal Super P), and N-methyl-2-pyrrolidone (NMP, MTI) as solvent were made. Prepared slurries were casted on copper foil using an automated doctor blade applicator. As-coated film was dried in a vacuum oven at 80 °C for 12 hours. After drying, the electrodes were cut to 12 mm circular disks and assembled into a 2032-type coin cell battery. Lithium metal (MTI) was used as a reference and counter-electrode and 1 M lithium hexafluorophosphate (1.0 M LiPF₆ in EC/DEC = 50/50, Sigma Aldrich) as electrolyte with Celgard

2500 polypropylene separator. Galvanostatic charge-discharge cycling was measured by Arbin BT-2000 in the potential range of 0.01- 2 V vs. Li^+/Li for both 25 °C and 50 °C condition.

3.3 Results and discussions

3.3.1 Morphological analysis

The morphology of coffee oil derived carbon was studied by SEM. As a result of the dry autoclave process, spherical and dumbbell-like carbon is formed. As-prepared and further heat treated materials show analogous morphologies (Figure 3.2a and 3.2b). In addition, some defective particles show that the carbon particles are solid and dense (Figure 3.2c and 3.2d).

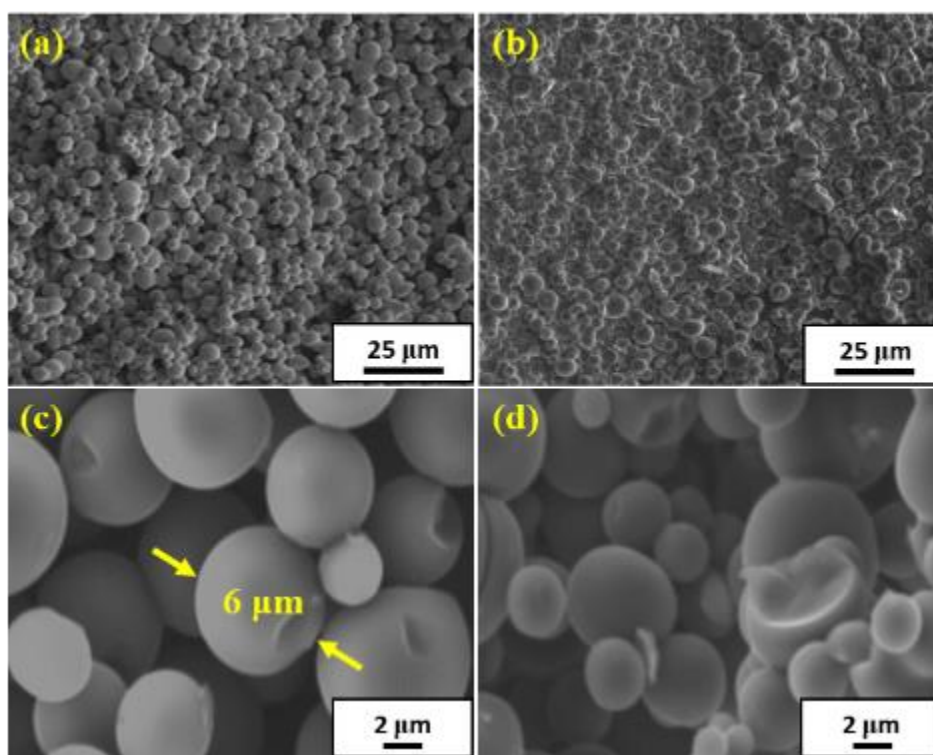


Figure 3.2 Scanning electron microscopy images of carbon particle prepared after dry autoclaving process (a), (c) and after additional pyrolysis (b), (d).

To clarify that the carbon particles are solid and dense, we conducted nitrogen adsorption-desorption analysis and measured the tap density (Figure 3.3 and Table 3.1). Adsorption-desorption hysteresis curves demonstrate the mesoporous structure of carbon particles.³⁴ Branauer-

Emmett-Teller (BET) calculations yielded a low surface area of $5.05 \text{ m}^2 \text{ g}^{-1}$ and the pore characteristics determined by Density Functional Theory (DFT) show a distribution of 2 – 5 nm (Figure 3.3). The obtained material has a cumulative pore volume of 0.006 cc g^{-1} . These spheroidal solid carbon particles have a tap density of 0.85 g cc^{-1} . Typically, measured tap density of the solid graphitic particles is 1 g cc^{-1} , which is essential measure to make high energy density batteries.³⁵

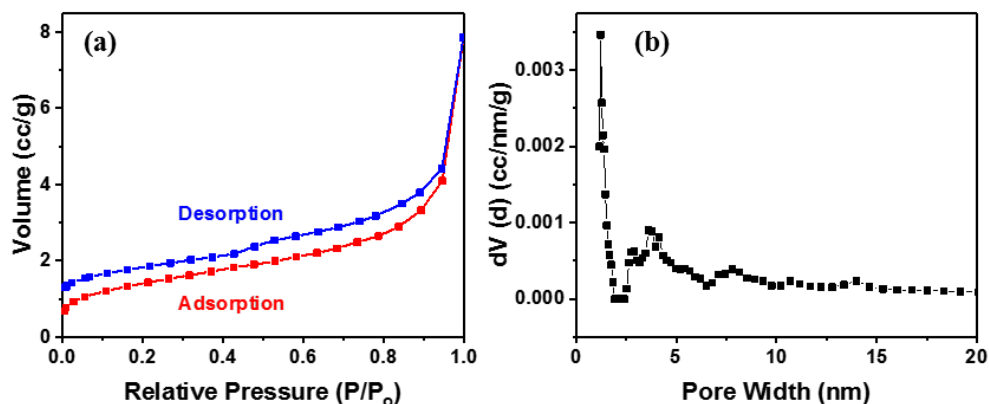


Figure 3.3 N_2 adsorption-desorption analysis of spheroidal carbon particles.

Table 3.1. Material Properties for Coffee-oil derived carbon

Sample	BET surface area ($\text{m}^2 \text{ g}^{-1}$)	DFT Pore Volume (cc g^{-1})	Tap Density (g cm^{-3})
Spheroidal carbon	5.05	0.006	0.85

3.3.2 Structural analysis of spheroidal carbon by Raman spectroscopy and XRD

The crystalline characteristics of coffee oil derived carbon were studied by X-ray diffraction (XRD) and Raman spectroscopy. The XRD pattern before and after pyrolysis show similar peak locations, such that the structure is well maintained after heat treatment, as presented in Figure 3.4. Coffee oil derived carbon shows two diffraction peaks (2θ) at $\sim 23.5^\circ$ and $\sim 43.5^\circ$, which originate from the (002) and (100) reflections of graphitic lattice, respectively. Using Eqns.

(1) and (2), the interlayer spacing (3.53 \AA) and in-plane lateral size (20.17 \AA) were calculated. Generally, lithium ion intercalates within the graphitic inter-layer spacing (3.35 \AA), whereas spherical carbon has an increased carbon interlayer ($> 3.5 \text{ \AA}$) to facilitate lithium ion storage kinetics.³⁶

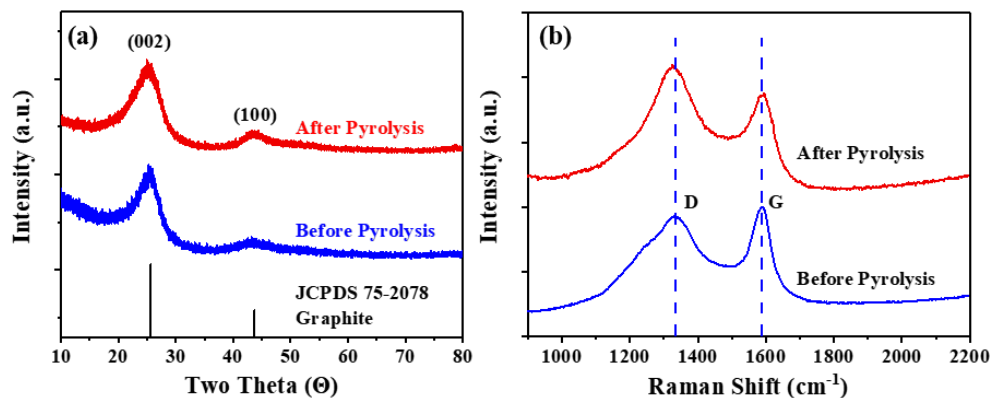


Figure 3.4 XRD (a) and Raman (b) spectra of coffee oil derived carbon.

Raman spectroscopy shows a blue shift of D peak (1330.8 to 1325.0 cm^{-1}), red shift of G peak (1588.3 to 1593.1 cm^{-1}) after pyrolysis with increased D/G ratio (from 0.94 to 1.18). From CHNO analysis, the initial coffee oil contains 77.8% carbon, 11.3% hydrogen, 10.6% oxygen, and 0.2% nitrogen. After dry autoclaving the compound changes to 96.0% C, 2.3% H, and 1.5% O, respectively. After pyrolysis, the final product consists of 99.0% C, 0.7% H, and 0.1% O (Table 3.2, STD DEV and nitrogen information is included). According to Ferrari's 3 stage theory, these phenomenon are explained as increased sp^2 clusters throughout the sample.³⁷ Therefore, initial coffee oil has developed into relatively amorphous carbon and after further pyrolysis step the final carbon contains more sp^2 clusters as removal of additional hydrogen and oxygen enables carbon to bond to each other.

Table 3.2 Results from CHNO analysis. Average values are highlighted in yellow, with standard deviation below (values are in weight %).

	Carbon	Hydrogen	Oxygen	Nitrogen
Pristine Coffee Oil	77.8%	11.3%	10.6%	0.21%
	0.35	0.43	0.16	0.09
Carbon with Dry Autoclaved Coffee Oil	96.0%	2.3%	1.5%	0.22%
	0.01	0.02	0.003	0.02
Spheroidal carbon after Pyrolysis	99%	0.7%	0.1%	0.18%
	0.07	0.02	0.05	0.04

3.3.3 Mechanistic elucidation of spheroidal carbon formation

The chemical components of coffee oil and their interactions at elevated temperatures during the dry autoclave process play an important role in determining the final morphology and structure of the produced carbon particles. Arabica coffee oil is composed of 79% triglycerides (glycerol with 3 fatty acids composed of C, H, O), 17% esters of diterpene alcohols (composed of C, H, O), and the remaining is fatty acids (C-H bonds and oxygen side groups) and sterols (steroids with a hydroxyl group).³⁸ In pristine coffee oil, the chemical elemental percentage is 78% carbon, 11% hydrogen and 10% oxygen. These constituents contain C-C, C-O, and C-H bonds,²⁶ which above 600 °C dissociate into individual elements in a closed dry reactor.³⁹ Above 700 °C, coffee oil comprising complex chemical structures decompose into its constituent individual elements either in gas or liquid phases or both phases based on the thermodynamic and kinetic stabilities of the comprised molecules/elements. For example, hydrogen and oxygen will become gases and C will remain in the liquid phase because of its high boiling point.³⁹ Liquid carbon crystals will be surrounded by gases components in a closed chamber.⁴⁰ Operando X-ray studies of polyethylene³⁹ during the dry autoclave process demonstrated that the precursor decomposes during heat treatment and that X-ray amorphous entities are produced at 700 °C. The solid spherical carbon particles nucleates at around 350 °C during cooling. The coffee oil precursor yields various morphologies, including spherical, dumbbell shaped and anisotropic carbon morphology. Gershi *et al.* studied various carbon precursors and investigated that carbon shape formation is dependent on the nature of the carbon chemical bonding (single, double, triple, etc.).⁴¹ Precursors containing

only one sp^2 bond will encourage prolate shaped carbon, while two or more result in a mixture of sphere and prolate shapes. Coffee oil contains triglycerides and esters containing multiple carbon double bonds, which explains why a mixture of spherical and dumbbell-like carbon morphologies result.

3.3.4 Electrochemical characterization

The first cycle discharge shows irreversible decomposition of electrolyte below 1.0 V, due to creation of the initial solid electrolyte interface (SEI) layer.⁴² The formation of SEI layer is seen by comparison of the charge-discharge voltage profiles of the first and second cycle (Figure 3.5a and 3.5b). The carbonized samples showed an initial lithiation capacity of 281.8 and 436.9 mAh g⁻¹ for cells tested at 25 °C and 50 °C, respectively. A first cycle irreversible capacity of 34.5% and 26.1% (25 and 50 °C, respectively) results, with the disappearing plateau region at ~1.0 V from the second cycle onward clarifying that the SEI stabilized. The smaller capacity loss of cells tested at 50 °C could be explained by the enhanced solid state diffusion of lithium ions. Increased diffusion kinetics will result in lower lithium residue after charging, which would give a higher initial coulombic efficiency for cells tested at high temperature.⁴³

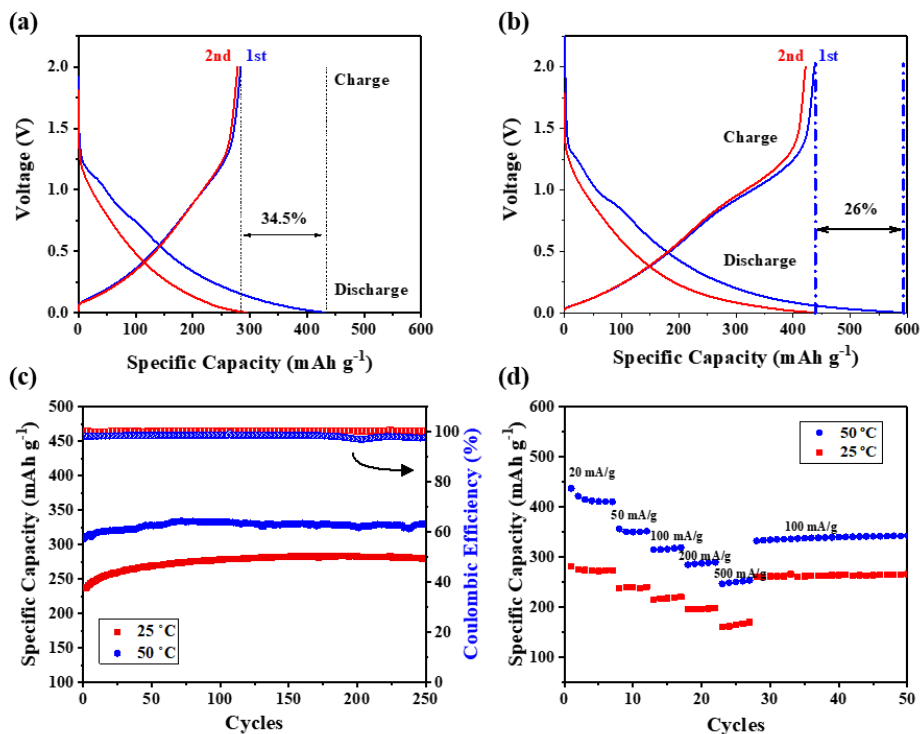


Figure 3.5 Electrochemical performance of spheroidal carbon. First and second cycle charge-discharge voltage profile at 25 °C (a), 50 °C (b), long cycling of spheroidal carbon anodes at 100 mA/g (c), and rate performance (d).

Galvanostatic cycling studies were conducted to determine the cycling stability and electrochemical performance of spheroidal carbon anode. Long term stability was determined at a current density of 100 mA g⁻¹ (Figure 3.5c). At room temperature, the specific capacity of 237.6 mAh g⁻¹ increased to 282.2 mAh g⁻¹ over 200 cycles and reached 274 mAh g⁻¹ after 250 cycles, which is a 97% retention. For the 50 °C cell, the initial capacity started at 311 mAh g⁻¹ and reached 342 mAh g⁻¹ after 100 cycles. The average Coulombic efficiency is 99% and 98% for 25 °C and 50 °C over 200 cycles, respectively. This difference is attributed to faster electrolyte depletion and increasing SEI layer thickness, which will increase impedance for cells tested at higher temperatures.⁴⁴ LiF is a well-known compound that forms SEI layer. Thereby, further EDX study of cycled cell at room and elevated temperature were conducted to compare the fluorine amount on the surface of electrode (Table 3.3). The amount detected was 2.5 wt% and 4.2 wt% for cell

cycled at room temperature and elevated temperature, respectively. Higher fluorine contents in elevated temperature cell verifies the fast electrolyte decomposition.

Table 3.3 The elemental analysis of Fluorine in both room and elevated temperature cycled cell electrode.

	Room Temperature	Elevated Temperature
wt% of Fluorine	2.47 wt%	4.15 wt%

A rate study was conducted at various current densities with stable capacities of 210 mAh g⁻¹ and 320 mAh g⁻¹ at 100 mA g⁻¹ current density (25 and 50 °C, respectively). High capacity at high temperature is attributed to the increased reaction kinetics and diffusion rate of Li ion.⁴⁵ The capacity at the initial 100 mA g⁻¹ (~210 mAh g⁻¹) compared to the final 100 mA g⁻¹ (~260 mAh g⁻¹) during the rate study shows a significant difference (Figure 3.5d). This phenomenon correlates with the cycling performance in Figure 3.5c, where the capacity increases over the first 100 cycles. In addition to LIBs, we have tested the possibility of coffee oil derived carbon as a sodium ion (SIB) and potassium ion battery (PIB) anode (Figure 3.6). For both SIB and PIB, cycling study was conducted at 100 mA g⁻¹ current density. The initial capacity of SIB is 123 mAh g⁻¹ and dropped to 109 mAhg⁻¹ after 200 cycles, an 88.6 % retention. PIB showed an initial capacity of 218.6 mAh g⁻¹ and reached 101.5 mAh g⁻¹ after 100 cycles which is 46.4 % retention. Potassium ion has smaller stokes radius compared to sodium ion. Thereby, the initial capacity is higher in PIB. Zhao et al. reported the importance of binder in PIB.⁴⁶ Carbon material using PVDF as binder shows low coulombic efficiency and continuous capacity degradation during repeated cycles. This explains the rapid capacity fading of our work.

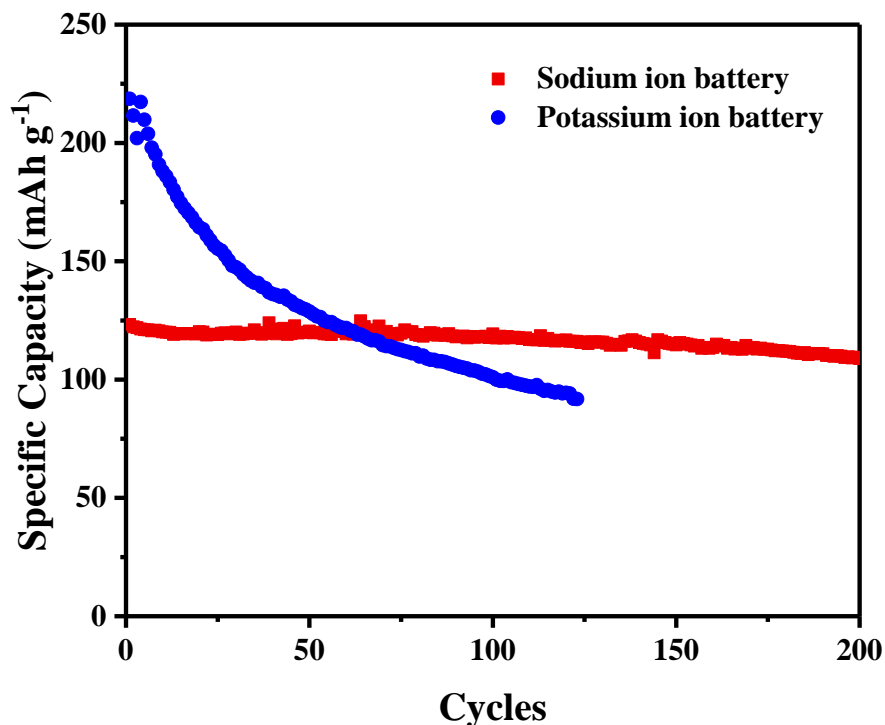


Figure 3.6 Cycling performance of sodium and potassium ion batteries.

3.3.5 Pre and post diagnostics: spheroidal carbon electrode analysis before/after cycling

To investigate the effect of long-term cycling (250 cycles) on spheroidal carbon electrodes, we performed SEM and Raman analysis on pristine and cycled electrodes. The prepared anode laminate is composed of spheroidal carbon connected by conductive carbon and PVDF binder (Figure 3.7a and 3.7c), leaving voids between carbon particles. The SEM image depicts that the morphology is maintained well throughout 250 cycles, with only additional surface roughness that can be attributed to SEI formation. Raman spectroscopy shows similar D and G bands positioned at ~ 1332 and 1592 cm^{-1} , respectively, for both pristine and cycled electrodes. The D/G ratio has slightly increased for cycled electrode compared to pristine (0.78 vs. 0.8). The traditional carbonaceous material, graphite, was reported to have an analogous trend of D/G ratio change before and after cycling.⁴⁷ These results noticeably describe the structural stability of coffee oil derived spheroidal carbon during continued charge-discharge cycles.

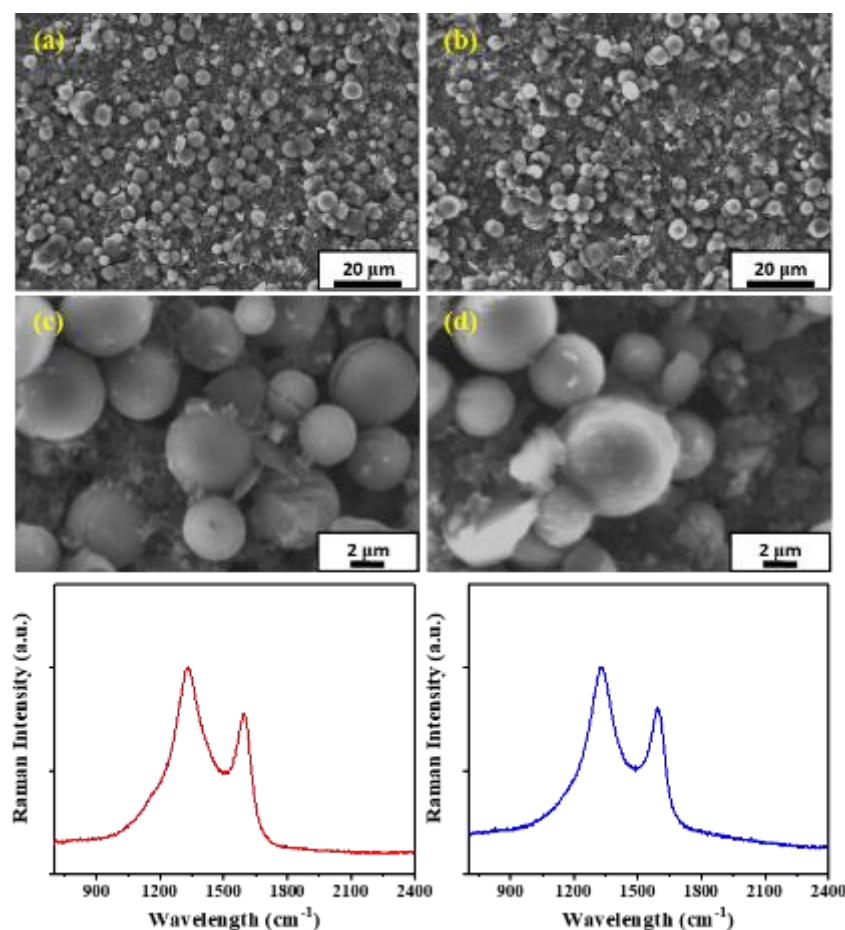


Figure 3.7 SEM images of spheroidal carbon electrode before (a, c) and after (b, d) Galvanostatic cycling. Raman spectra of electrode before (e) and after (f) cycling.

3.4 Conclusion

Reported here is a solvent-free, catalyst-free, and facile method to fabricate spherical carbon particles for electrochemical energy storage application. The formation of carbon spheres is discussed as the decomposition of coffee oil at elevated temperature (700 °C) with self-generated pressure, and subsequent carbon crystallization at ~ 350 °C during cooling. Compared to other olive oil or mesitylene precursors, coffee oil contains linoleic acid (contains more than two sp^2 bonding), which induces a mixture of spherical and anisotropic structures. A stable capacity of 270 mAh g⁻¹ is achieved at 20 mA g⁻¹ current density, along with stable rate performance achieving 240 mAh g⁻¹ at 100 mA g⁻¹. Stable cycling with a capacity increasing to 280 mAh g⁻¹ and 99.9%

Coulombic efficiency up to 250 cycles was demonstrated at a current density of 100 mA g⁻¹. This work demonstrated that the dry autoclave method is effective for producing materials for secondary ion batteries and may also be useful to various other fields, such as lubrication.⁴⁸

3.5 Reference

- 1 Larcher, D. & Tarascon, J. M. Towards greener and more sustainable batteries for electrical energy storage. *Nat Chem* (2015) **7**, 19-29, doi:10.1038/Nchem.2085.
- 2 Gao, Z., Zhang, Y. Y., Song, N. N. & Li, X. D. Biomass-derived renewable carbon materials for electrochemical energy storage. *Mater Res Lett* (2017) **5**, 69-88, doi:10.1080/21663831.2016.1250834.
- 3 Stevens, D. A. & Dahn, J. R. The mechanisms of lithium and sodium insertion in carbon materials. *J. Electrochem. Soc.* (2001) **148**, A803-A811, doi:10.1149/1.1379565.
- 4 Sun, Y.-P. *et al.* Quantum-sized carbon dots for bright and colorful photoluminescence. *J Am Chem Soc* (2006) **128**, 7756-7757.
- 5 Strubel, P. *et al.* ZnO Hard Templating for Synthesis of Hierarchical Porous Carbons with Tailored Porosity and High Performance in Lithium-Sulfur Battery. *Adv Funct Mater* (2015) **25**, 287-297.
- 6 Titirici, M. M., Thomas, A. & Antonietti, M. Replication and coating of silica templates by hydrothermal carbonization. *Adv Funct Mater* (2007) **17**, 1010-1018.
- 7 Choucair, M. & Stride, J. A. The gram-scale synthesis of carbon onions. *Carbon* (2012) **50**, 1109-1115.
- 8 Al-Muhtaseb, S. A. & Ritter, J. A. Preparation and properties of resorcinol–formaldehyde organic and carbon gels. *Adv. Mater.* (2003) **15**, 101-114.
- 9 Hu, Y. S. *et al.* Superior storage performance of a Si@SiO_x/C nanocomposite as anode material for lithium-ion batteries. *Angew. Chem. Int. Edit.* (2008) **47**, 1645-1649, doi:10.1002/anie.200704287.
- 10 Cakan, R. D. *et al.* Hydrothermal carbon spheres containing silicon nanoparticles: synthesis and lithium storage performance. *Chem. Commun.* (2008), 3759-3761, doi:10.1039/b805671b.
- 11 Xiang, H. F. *et al.* Graphene/nanosized silicon composites for lithium battery anodes with improved cycling stability. *Carbon* (2011) **49**, 1787-1796, doi:10.1016/j.carbon.2011.01.002.
- 12 Demazeau, G. Solvothermal reactions: an original route for the synthesis of novel materials. *J Mater Sci* (2008) **43**, 2104-2114, doi:10.1007/s10853-007-2024-9.
- 13 Zhang, M. *et al.* Magnetite/graphene composites: microwave irradiation synthesis and enhanced cycling and rate performances for lithium ion batteries. *J Mater Chem* (2010) **20**, 5538-5543, doi:10.1039/c0jm00638f.
- 14 Wolf, H., Pajkic, Z., Gerdes, T. & Willert-Porada, M. Carbon-fiber-silicon-nanocomposites for lithium-ion battery anodes by microwave plasma chemical vapor deposition. *J Power Sources* (2009) **190**, 157-161, doi:10.1016/j.jpowsour.2008.07.035.
- 15 Erb, U. Electrodeposited nanocrystals: Synthesis, properties and industrial applications. *Nanostruct Mater* (1995) **6**, 533-538, doi:Doi 10.1016/0965-9773(95)00114-X.

- 16 Mangolini, L., Thimsen, E. & Kortshagen, U. High-yield plasma synthesis of luminescent silicon nanocrystals. *Nano Lett.* (2005) **5**, 655-659, doi:10.1021/nl050066y.
- 17 Pol, V. G., Pol, S. V. & Gedanken, A. Dry Autoclaving for the Nanofabrication of Sulfides, Selenides, Borides, Phosphides, Nitrides, Carbides, and Oxides. *Adv. Mater.* (2011) **23**, 1179-1190, doi:10.1002/adma.201001210.
- 18 Pol, V. G., Pol, S. V. & Gedanken, A. Core-shell nanorods of SnS-C and SnSe-C: Synthesis and characterization. *Langmuir* (2008) **24**, 5135-5139, doi:10.1021/la7040532.
- 19 Pol, S. V., Pol, V. G., Calderon-Moreno, J. M., Cheylan, S. & Gedanken, A. Facile synthesis of photoluminescent ZnS and ZnSe nanopowders. *Langmuir* (2008) **24**, 10462-10466, doi:10.1021/la800921a.
- 20 George, P. P., Pol, V. G. & Gedanken, A. Synthesis of carbon encapsulated nanocrystals of WP by reacting W(CO)(6) with triphenylphosphine at elevated temperature under autogenic pressure. *J Nanopart Res* (2007) **9**, 1187-1193, doi:10.1007/s11051-006-9201-7.
- 21 George, P. P. *et al.* Synthesis and characterization of titanium nitride, niobium nitride, and tantalum nitride nanocrystals via the RAPET (reaction under autogenic pressure at elevated temperature) technique. *J Nanopart Res* (2009) **11**, 995-1003, doi:10.1007/s11051-008-9550-5.
- 22 Pol, V. G., Pol, S. V. & Gedanken, A. Novel synthesis of high surface area silicon carbide by RAPET (reactions under autogenic pressure at elevated temperature) of organosilanes. *Chem Mater* (2005) **17**, 1797-1802, doi:10.1021/cm048032z.
- 23 Pol, V. G., Pol, S. V. & Gedanken, A. One-Step Synthesis and Characterization of SiC, Mo₂C, and WC Nanostructures. *Eur J Inorg Chem* (2009), 709-715, doi:10.1002/ejic.200801037.
- 24 Pol, V. G., Motiei, M., Gedanken, A., Calderon-Moreno, J. & Yoshimura, M. Carbon spherules: synthesis, properties and mechanistic elucidation. *Carbon* (2004) **42**, 111-116, doi:10.1016/j.carbon.2003.10.005.
- 25 Pol, V. G., Calderon-Moreno, J. M., Chupas, P. J., Winans, R. E. & Thiyagarajan, P. Synthesis of monodispersed prolate spheroid shaped paramagnetic carbon. *Carbon* (2009) **47**, 1050-1055, doi:10.1016/j.carbon.2008.12.028.
- 26 Pol, V. G., Calderon-Moreno, J. M. & Thiyagarajan, P. Catalyst-Free, One-Step Synthesis of Olivary-Shaped Carbon from Olive Oil. *Ind Eng Chem Res* (2009) **48**, 5691-5695, doi:10.1021/ie900095v.
- 27 Hong, K. L. *et al.* Biomass derived hard carbon used as a high performance anode material for sodium ion batteries. *J. Mater. Chem. A* (2014) **2**, 12733-12738, doi:10.1039/c4ta02068e.
- 28 Tang, J. L., Etacheri, V. & Pol, V. G. Wild Fungus Derived Carbon Fibers and Hybrids as Anodes for Lithium-Ion Batteries. *Acs Sustain. Chem. Eng.* (2016) **4**, 2624-2631, doi:10.1021/acssuschemeng.6b00114.
- 29 Tang, J. L., Etacheri, V. & Pol, V. G. From Allergens to Battery Anodes: Nature-Inspired, Pollen Derived Carbon Architectures for Room- and Elevated-Temperature Li-ion Storage (vol 6, 20290, 2016). *Sci. Rep.* (2016) **6**, doi:Artn 32276 10.1038/Srep32276.

- 30 Kyungho Kim, D. G. L., Chang Wan Han, Sebastian Osswald, Volkan Ortalan, Jeffrey P. Youngblood, and Vilas G. Pol. Tailored Carbon Anodes Derived from Biomass for Sodium-Ion Storage. *Acs Sustain. Chem. Eng.* (2017), doi:10.1021/acssuschemeng.7b01497.
- 31 Yang, S., Wu, M. & Wu, C. Application of biomass fast pyrolysis part I: Pyrolysis characteristics and products. *Energy* (2014) **66**, 162-171.
- 32 Hughes, S. R. *et al.* Sustainable conversion of coffee and other crop wastes to biofuels and bioproducts using coupled biochemical and thermochemical processes in a multi-stage biorefinery concept. *Appl Microbiol Biot* (2014) **98**, 8413-8431, doi:10.1007/s00253-014-5991-1.
- 33 Organization, I. C. *Coffee Market Report*, <<http://www.ico.org/documents/cy2016-17/cmr-0617-e.pdf>> (2017).
- 34 Thommes, M. *et al.* Physisorption of gases, with special reference to the evaluation of surface area and pore size distribution (IUPAC Technical Report). *Pure Appl Chem* (2015) **87**, 1051-1069, doi:10.1515/pac-2014-1117.
- 35 Pol, V. G. & Thackeray, M. M. Spherical carbon particles and carbon nanotubes prepared by autogenic reactions: Evaluation as anodes in lithium electrochemical cells. *Energ Environ Sci* (2011) **4**, 1904-1912, doi:10.1039/c0ee00256a.
- 36 Cao, Y. L. *et al.* Sodium Ion Insertion in Hollow Carbon Nanowires for Battery Applications. *Nano Lett.* (2012) **12**, 3783-3787, doi:10.1021/nl3016957.
- 37 Ferrari, A. C. & Robertson, J. Interpretation of Raman spectra of disordered and amorphous carbon. *Phys Rev B* (2000) **61**, 14095-14107, doi:DOI 10.1103/PhysRevB.61.14095.
- 38 Spiller, G. A. *Caffeine*. (CRC Press, 1997).
- 39 Pol, V. G. *et al.* Probing the evolution and morphology of hard carbon spheres. *Carbon* (2014) **68**, 104-111, doi:10.1016/j.carbon.2013.10.059.
- 40 Hurt, R. H. & Chen, Z. Y. Liquid crystals and carbon materials. *Phys Today* (2000) **53**, 39-44, doi:Doi 10.1063/1.883020.
- 41 Gershi, H., Geclanken, A., Keppner, H. & Cohen, H. One-step synthesis of prolate spheroidal-shaped carbon produced by the thermolysis of octene under its autogenic pressure. *Carbon* (2011) **49**, 1067-1074, doi:10.1016/j.carbon.2010.11.003.
- 42 Dong, J. J. *et al.* Remarkable cycle-activated capacity increasing in onion-like carbon nanospheres as lithium battery anode material. *Nanotechnology* (2017) **28**, doi:Artn 035704 10.1088/1361-6528/28/3/035704.
- 43 Qiu, B. *et al.* Temperature dependence of the initial coulombic efficiency in Li-rich layered Li_{0.144}Ni_{0.136}Co_{0.136}Mn_{0.544}O₂ oxide for lithium-ions batteries. *J Power Sources* (2014) **268**, 517-521, doi:10.1016/j.jpowsour.2014.06.031.
- 44 Marco-Tulio F. Rodrigues, G. B., Hemtej Gullapalli, Kaushik Kalaga, Farheen N. Sayed, Keiko Kato, Jarin Joyner and Pulickel M. Ajayan. A materials perspective on Li-ion batteries at extreme temperatures. *Nature Energy* (2017) **2**, doi:10.1038/nenergy.2017.108.
- 45 Adams, R. A. *et al.* Superior Lithium-Ion Storage at Room and Elevated Temperature in an Industrial Woodchip Derived Porous Carbon. *Ind Eng Chem Res* (2016) **55**, 8706-8712, doi:10.1021/acs.iecr.6b01786.

- 46 Zhao, J., Zou, X., Zhu, Y., Xu, Y. & Wang, C. Electrochemical intercalation of potassium into graphite. *Adv Funct Mater* (2016) **26**, 8103-8110.
- 47 Inaba, M. *et al.* In situ Raman study on electrochemical Li intercalation into graphite. *J. Electrochem. Soc.* (1995) **142**, 20-26.
- 48 Alazemi, A. A. *et al.* Novel tertiary dry solid lubricant on steel surfaces reduces significant friction and wear under high load conditions. *Carbon* (2017) **123**, 7-17, doi:10.1016/j.carbon.2017.07.030.

4. CARBON DERIVED FROM BIOMASS FOR SODIUM ION BATTERY AND ITS STORAGE MECHANISM STUDY

The scientific hypothesis was made by K.Kim and executed with the help of Prof. J. Youngblood and Prof. V. Pol. Most of the experimental and characterization work was performed by K.Kim. D.G Lim performed Raman and analysis with advice from Prof. Osswald. C.W. Han performed TEM and analysis with advice from Prof. Ortalan. Data analysis was conducted by K.Kim and discussion was made with D.G Lim and C.W. Han. Manuscript writing was performed by K. Kim and revised by D.G Lim, C.W. Han, Prof. S. Osswald, Prof. V. Ortalan, Prof. J. P. Youngblood, and Prof. V. G. Pol.

The following chapter contains content reproduced with permission from K. Kim, D.G Lim, C.W. Han, S. Osswald, V. Ortalan, J. P. Youngblood, and V. G. Pol., Tailored Carbon Anodes Derived from Biomass for Sodium-ion Storage, *ACS Sustainable Chemistry and Engineering* **2017**, 5 (10), 8720 - 8728. Copyright 2017 American Chemical Society.

4.1 Alternative energy storage system

Since its development in early 1990s, lithium ion batteries (LIB) have dominated the world energy storage systems. LIB has been applied in numerous systems including portable devices, uninterruptable back-up power source, systems in remote regions, and many other systems. However, recent technology such as electric vehicles and large intermittent systems require energy storage system with larger capacity, larger power density, sustainability, and cheaper cost. Furthermore, lithium has limited terrestrial reserves and is commonly obtained in geo-political sensitive regions that can increase the cost of commodity lithium.¹⁻³ Thereby, economic, performance, and political concerns on lithium boost research on an alternative next generation batteries.

4.2 Introduction to sodium ion batteries

Sodium ion battery (SIB) has emerged as an alternative energy storage system for its abundant resource and similarity to lithium ion battery (LIB).^{4,5} Sodium, the world's 4th most

abundant element, has similar chemical and physical characteristics to lithium. Table 4.1 shows the characteristics of lithium and sodium.

Table 4.1 The characteristics comparison of lithium and sodium.

	Lithium	Sodium
Cation radius (Å)	0.76	1.06
Atomic Weight	6.9 g/mol	23 g/mol
E° (vs. SHE)	-3.04	-2.71
Cost of carbonate (\$ / ton)	5000	150
Capacity (mAh g ⁻¹), metal	3829	1165
Distribution	70% in South America	Everywhere

The working principle of SIB and LIB is analogous. During discharge, the sodium ion migrates from anode to cathode. To balance the charge, electron travels through external circuit to cathode as well. This process is reversed during charging. Due to similar working principle, the early stage research of SIB anode material focused on materials used in LIB. However, for SIB, graphite did not show promising result. The failure of graphite is due to the ionic size difference between lithium and sodium (0.76 Å for Li⁺ and 1.06 Å for Na⁺). The interlayer spacing of graphite, 0.34 nm, is insufficient for sodium intercalation.^{1,6,7} Conversion and alloying type anode materials have been reported as well. Sn,⁸⁻¹² SnO₂,¹³ Co₃O₄,¹⁴ Sb,¹⁵⁻¹⁷ SbO_x,¹⁸ P,^{19,20} Si,²¹ and CuO^{22,23} exhibit high specific capacities, however, large volume expansion and pulverization continue to plague metal- and metal oxide-based electrodes. Organic compounds such as sodium terephthalate (Na₂C₈H₂O₄)²⁴ offer high flexibility in electrode designs, but suffer from insufficient electron conductivity.²⁵

4.3 Introduction of this work

As mentioned in previous section, graphite is not a suitable SIB anode material due to the insufficient interlayer spacing.^{1,6,7} Instead, hard carbon with its stable cyclability, good capacity number, low cost, and low potential is a promising anode. Stevens and Dahn have shown the

possibility of glucose-derived carbon as an anode for SIB. They demonstrated a first reversible capacity of 300 mAh g⁻¹ at C/80 rate.²⁶ Other studies have reported similar results: hard carbon precursors such as polyacrylonitrile-derived nanofibers delivered an initial capacity of 233 mAh g⁻¹ at a current density of 50 mAh g⁻¹ and achieved a capacity retention of 97%.²⁷ LDPE bag-derived carbon spheres showed first charge cycle capacity as 250 mAh g⁻¹ and dropped to 150 mAh g⁻¹ after the third cycle at 15 mAh g⁻¹,²⁸ and electrospun PVC exhibited 389 mAh g⁻¹ at first cycle and 211 at 120th cycle at 12 mAh g⁻¹.²⁹

Among available hard carbon precursors, biomass has been heavily studied for its low cost and accessibility.^{30,31} Furthermore, global interest in ‘green energy’ led to growing interest in biomass due to its environmentally-friendly and sustainable characteristics.³² Recent biomass applications in battery research include banana peels,³³ sugar,^{34,35} cellulose,³⁶ lignin,³⁷ peat moss,³⁸ lotus,³⁹ and pomelo peel.² Wu et al. reported the possibility of using apple bio-waste derived carbon material as an SIB anode.⁴⁰ They applied phosphoric acid to increase the porosity and surface area of the derived carbon. The initial reversible capacity measured 245 mAh g⁻¹ at a current density of 20 mA g⁻¹ and after 50 cycles the capacity still measured 240 mAh g⁻¹.

In this study, we investigated the use of pistachio shell as a possible feedstock for carbon electrode material production. Over 10% of the annual U.S. tree nut production (more than 250,000 tons) is pistachios, following almonds and walnuts.⁴¹ Thus, considering the shell/pistachio ratio (~45%), over 100,000 tons of pistachio shell is being produced annually and wasted every year.⁴² This represents a significant potential resource for biomass-derived carbon. Xu et al. applied pistachio shell in a supercapacitor and reported an energy density of 39 Wh kg⁻¹ and a power density of 286 kW kg⁻¹ using 1 M TEABF₄ in EC:DEC (1:1) electrolyte.⁴³ These promising values were reportedly due to a large surface area of 1069 m² g⁻¹ using chemical activation steps for the formation of micropores and surface functional group. These results suggest that pistachio shell-derived carbons may possess huge potential as an SIB anode. Unfortunately, previous chemical activations required neutralization with acid treatment and two or more additional steps.

Accordingly it is desirable to develop a more eco-friendly process for obtaining a porous carbonized structure. We simply introduce carbonization without any prior- or pre-treatment to obtain carbonized pistachio shell for SIB anode. Different carbonization temperature has been applied to understand the temperature effect on pistachio derived carbon structure and electrochemical performance. Pistachio shell carbonized at 1000°C shows high surface area (760.9

m²/g) and dilated interlayer spacing (>0.37 nm), which gives a desodiation capacity (225 mAh/g) higher than other carbonization temperature. Although pistachio derived carbon does not show the highest reported specific capacity, among the simple and eco-friendly synthetic approaches, it is reasonably enhanced. Compared to other biomass derived carbon, this work uses lower reaction temperature (favorable for industry to reduce cost) and no pre/post-treatment to obtain 225mAh/g anode capacity, and, importantly, the source is from a large scale source of biomass waste. Obtaining large surface area (760 m²/g) without pre/post-treatment which has not been reported by other biomass derived carbon shows the possibility of using pistachio shell not only for battery electrode but also for other storage system (e.g. capacitor). In addition, our work uses higher loading mass than other biomass derived carbon (2 mg/cm² vs. ~1 mg/cm²). According to Kil and Paik, the loading mass (thickness) of electrode has influence on the electrochemical performance.⁴⁴ Therefore, direct comparison of our work and other biomass derived carbon is not likely. We have also looked into the sodium storage mechanism for our material. High surface area (reducing the solid state diffusion of ion at higher current rate), defect sites (D/G intensity ratio from Raman spectroscopy), pseudocapacitance behavior and dilated interlayer spacing of amorphous carbon explains our carbon behavior. Table 4.2 demonstrates selected biomass, reaction conditions, electrochemical performance and storage mechanism.

Table 4.2 Literature survey of various biomass derived carbon anodes and their electrochemical performance.

Precursor	Synthesis	Capacity (mAh g ⁻¹)	Coulombic efficiency	Mechanism	Loading mass (mg/cm ²)
Peat moss ³⁸	Pyrolysis (1100 °C) HCl + KOH	300	57.5%	<ul style="list-style-type: none"> ● Pseudographitic ● Intercalation 	~ 1.0
Pomelo Peels ²	Pyrolysis (700 °C) Phosphoric acid	288	27%	<ul style="list-style-type: none"> ● Intercalation ● O-containing surface ● Nano pore filling 	N/A
Rape seed shuck ⁴⁵	Hydrothermal Pyrolysis (700 °C)	196	~ 62%	<ul style="list-style-type: none"> ● Not specified 	N/A
Cellulose ⁴⁶	Pyrolysis (700 °C)	125	39%	<ul style="list-style-type: none"> ● Intercalation ● Micropore insertion 	N/A
Apple ⁴⁰	Pyrolysis (1100 °C) Phosphoric acid	245	61%	<ul style="list-style-type: none"> ● Intercalation ● Surface group (H, S, N) ● Micropore filling 	1
Lotus petioles ³⁹	Pyrolysis (1100 °C)	230	~ 52%	<ul style="list-style-type: none"> ● Intercalation ● Surface group (F) 	1 ~ 1.5
Pistachio Shell	Pyrolysis (1000 °C)	225	71%	<ul style="list-style-type: none"> ● Intercalation ● Defect site 	1.9

4.4 Experimental

4.4.1 Synthesis of pistachio shell derived carbon

Commercial salted pistachio shell (Southern Grove product) was used as a carbon precursor after seed extraction. 5 grams of pistachio shells were loaded in an alumina crucible and then placed inside a tube furnace under inert argon gas flow of 10 ml min⁻¹. The carbon precursor was carbonized at 700°C, 1000°C, 1300°C and 1500°C (named P700, P1000, P1300, P1500 respectively) with a constant temperature ramping rate of 5°C/min, and held at each carbonization temperature for 2 hours. The average yield obtained is 0.8g which is ~15% of initial precursor. Carbonized samples were thoroughly washed using DI water to remove unreacted NaCl and then dried at 300°C for 2 hours under argon gas flow. Ball milling (8000 M Mixer/Mill from SPEX Sample Prep) was used to mill as-prepared carbonaceous shell into black powder.

4.4.2 Material characterization

The morphologies and microstructures of carbonized samples were investigated by scanning electron microscope (SEM, FEI quanta 3D FEG dual-beam at 30 kV) and transmission electron microscope (TEM, FEI Titan ETEM 80-300 at 300 kV) equipped with an electron energy loss spectrometer (EELS, Gatan GIF Tridiem). Selected area electron diffraction (SAED) patterns were obtained using a selected area (SA) aperture of 40 μm and a camera length (CL) of 71.6 cm. CL calibration was performed using Au nanoparticles and DiffTools.⁴⁷ Azimuthal averaging and background subtraction using a Digital Micrograph plug-in PASAD software, calculated the pixel size of each diffraction pattern.⁴⁸

The Brunauer-Emmett-Teller (BET) surface area was examined using a nitrogen adsorption-desorption apparatus (Quantachrome Nova 2200e). Thermogravimetric analysis (TGA, TA instruments Q50) was conducted under an argon gas flow of 40 ml min^{-1} at constant heating and cooling rates of 5°C min^{-1} .

The structures of the carbonized samples were also investigated using Raman spectroscopy (Renishaw, InVia Raman microscope) and X-ray diffractometer (XRD, Rigaku at 40 kV and 44 mA). (002) and (100) XRD peaks obtained by a Cu-K α source ($\lambda=0.154$ nm) were used to measure the inter-planar spacing ($d_{(002)}$) and the lateral size (L_a) of carbonized shells from Bragg's law and Scherrer's equation (eq. 1), respectively.

$$d = \frac{\lambda}{\sin \theta}$$

$$L = \frac{K \lambda}{B \cos \theta} \quad (1)$$

Here, B is the full width half maximum (FWHM) of each diffraction peak and K is a dimensionless shape factor, i.e. 1.84 for lateral size and 0.91 for stacking height calculation.

4.4.3 Electrochemical characterization

Electrode slurries were prepared with 80 wt.% pistachio shell derived carbon, 10 wt.% polyvinylidene fluoride (PVDF, MTI), and 10 wt.% conductive carbon (Timcal SuperP). These slurries were dispersed in N-methyl-2-pyrrolidone (NMP, MTI), and casted on copper foil using an automated doctor blade applicator. The casted films were dried in a vacuum oven at 80°C for 12

hr. The as-prepared electrode was cut to disks and assembled into a 2032-type coin cell battery using a sodium metal electrode (Sigma Aldrich) as a counter-electrode and 1M NaClO₄ (Sigma Aldrich) in propylene carbonate (Sigma Aldrich) as an electrolyte with a glass fiber separator. The loading mass of prepared electrode is 1.9 mg/cm². Cell assembly was conducted in an argon filled glove box. The galvanostatic charge-discharge was measured by BST8-MA (MTI Corporation) in the potential range of 0 to 2 V.

4.5 Results and discussion

In order to identify the required process temperature and to gain deeper insight into the carbonization mechanism of pistachio shell, thermogravimetric (TG) analysis was conducted (Figure 4.1a). TGA data revealed that the thermal degradation of pistachio shell occurs in several characteristic steps. Below 100 °C, temperatures are not sufficient to induce structural changes in the material and weight loss is primarily caused by the removal of moisture. The actual carbonization process of pistachio shell can be divided into 3 temperature stages. First stage (stage I) is at a range of 250 – 300 °C, second (stage II) near 350 °C and final stage (stage III) is from 350 to 900 °C.

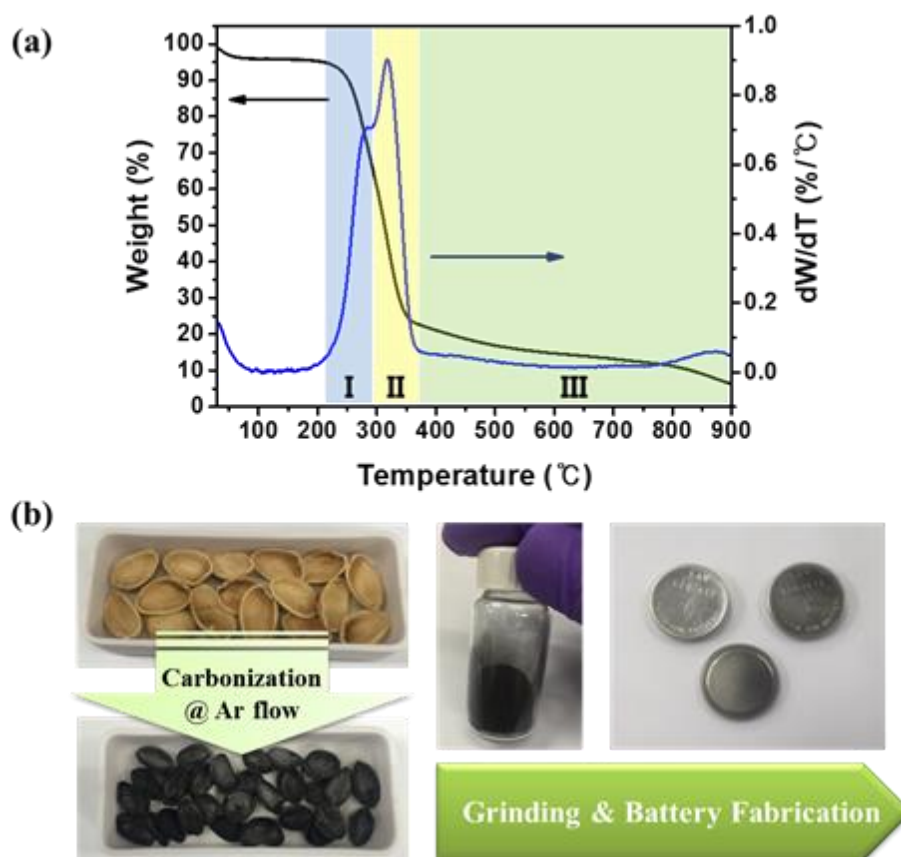


Figure 4.1 (a) TGA result of pistachio shell in inert atmosphere and (b) preparation of rechargeable SIB using pistachio shells derived carbon treated at 1000 °C.

Pistachio shell is classified as biomass, a lignocellulosic material composed of hemicellulose, cellulose and lignin. The decomposition temperatures of the three lignocellulosic components are known to be 210–325 °C, 310–400 °C, and 250–900 °C for hemicellulose, cellulose, and lignin, respectively,⁴⁹ in good agreement with the stages observed in our experiments. The three lignocellulosic components contain volatile alcohol, ether, and methyl groups which vaporize as the carbonization temperature increases and the final product such as carboxylic acids, phenols, ketones, and aldehydes, which toxicity level can be easily decreased by disproportionation treatment and solid (carbon char) is obtained.^{50,51}

4.5.1 Structural analysis of pistachio shell derived carbon by Raman spectroscopy and XRD

As structural characterization and electrochemical studies require larger amounts of carbon material, several grams of pistachio shell were carbonized using a tube furnace (Figure 4.1b). The structure of carbon derived from pistachio shells was investigated by both Raman spectroscopy and XRD. As shown in Figure 4.2a, two broad Raman bands were observed near 1340 and 1600 cm^{-1} for all samples, representing the D band (breathing mode of κ -point phonons with A_{1g} symmetry occurring at defective graphitic sites) and the G band (E_{2g} vibration mode of carbon-carbon bonding in 2-D hexagonal lattice), respectively. In Figure 2b, the D- to G- band intensity ratio (I_D/I_G) increases as the carbonization temperature rise, yielding 0.81, 0.98, 1.05, and 1.11 for P700, P1000, P1300, and P1500, respectively. The I_D/I_G value and error bar has been calculated by directly reading the intensity of D- and G-band from ten different measurement points for each sample.

The increase in I_D/I_G and the corresponding structural changes may be explained by Ferrari's "three-stage model".⁵² As the D-band intensity is proportional to the number of six-fold rings, it increases when sp^3 -bonded carbon atoms aromatize into sp^2 -rings. Therefore, with increasing carbonization temperature, the increasing I_D/I_G ratio of our experiment indicates a conversion of sp^3 carbon and formation of sp^2 -rings.

Figure 4.2c shows that all carbonized samples have two diffraction peaks (2θ) around $22\sim 24^\circ$ and $42\sim 44^\circ$, which represent the (002) and (100) reflection peaks of the graphitic lattice, respectively. Using Eq. (1), inter-planar spacing and in-plane lateral size were calculated and are depicted in Figure 4.2d. Both lattice spacing and lateral size start to change upon carbonization at temperatures above 1300 $^\circ\text{C}$ (P1300 and P1500). These results indicate that while for the selected precursor (pistachio shells) carbonization starts around 300 $^\circ\text{C}$ (TGA data), whereas graphitization requires temperatures beyond 1300 $^\circ\text{C}$ to enhance inner-planar and inter-planar ordering of the carbonized carbon. Data obtained by Raman spectroscopy support these findings (Figure 4.2b). P700 and P1000 show similar lattice spacing (Figure 4.2d) but P1000 is subject to more ordering (Figure 4.2b). This can be explained by the formation of more sp^2 clusters in P1000 as compared to P700. At higher carbonization temperatures (P1300 and P1500), carbon atoms possess enough thermal energy to rearrange. Consequently, sp^2 clusters grow in size, a process referred to as

graphitization (Figure 4.2d). Therefore, our results indicate that the amount of graphitic ordering and the size of graphitic clusters can be controlled by adjusting the carbonation temperature.

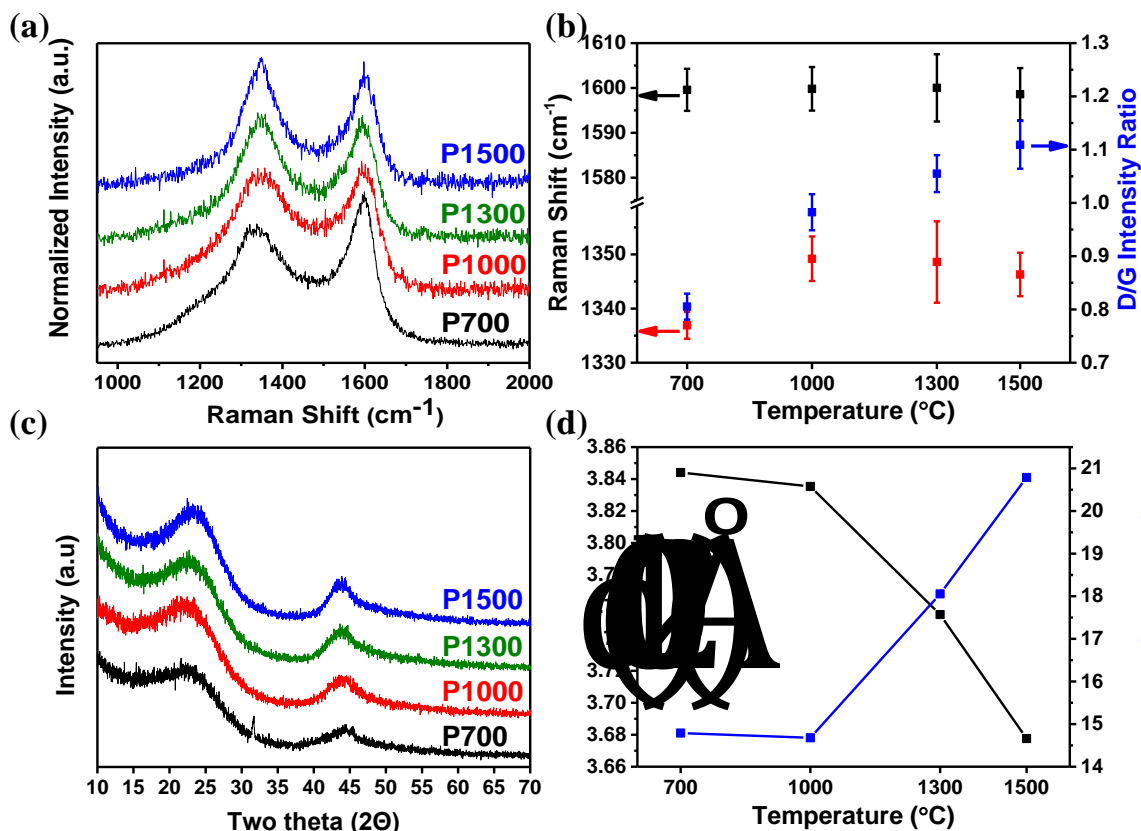


Figure 4.2 Raman spectra (a), (b) and XRD analysis (c), (d) of pistachio shell derived carbons at various temperatures.

4.5.2 TEM analysis

TEM analysis was carried out to visualize the microstructures of the carbonized samples (Figure 4.3). The first columns in Figure 4.3 depict the low magnification images (28,277x which is 0.4951 nm/pixel) of each sample. Size and morphology of carbon particles in all samples are similar. This is expected, as nearly all of the weight loss observed upon carbonization occurs below 700 $^{\circ}\text{C}$ (Figure 4.1a). High resolution images (second column in Figure 4.3, 481,803x which is 0.029 nm/pixel) reveal a highly amorphous microstructure in all carbonized samples. As the carbonization temperature increases from 700 to 1500 $^{\circ}\text{C}$, carbon layers grow in length and become increasingly ordered. This tendency is more clearly visible in the fast Fourier

transformation (FFT) patterns (third column in Figure 4.3) of the high resolution images. The intensity of the (002) reflection becomes stronger and sharper with increasing carbonization temperature, thus supporting our previous assumptions.

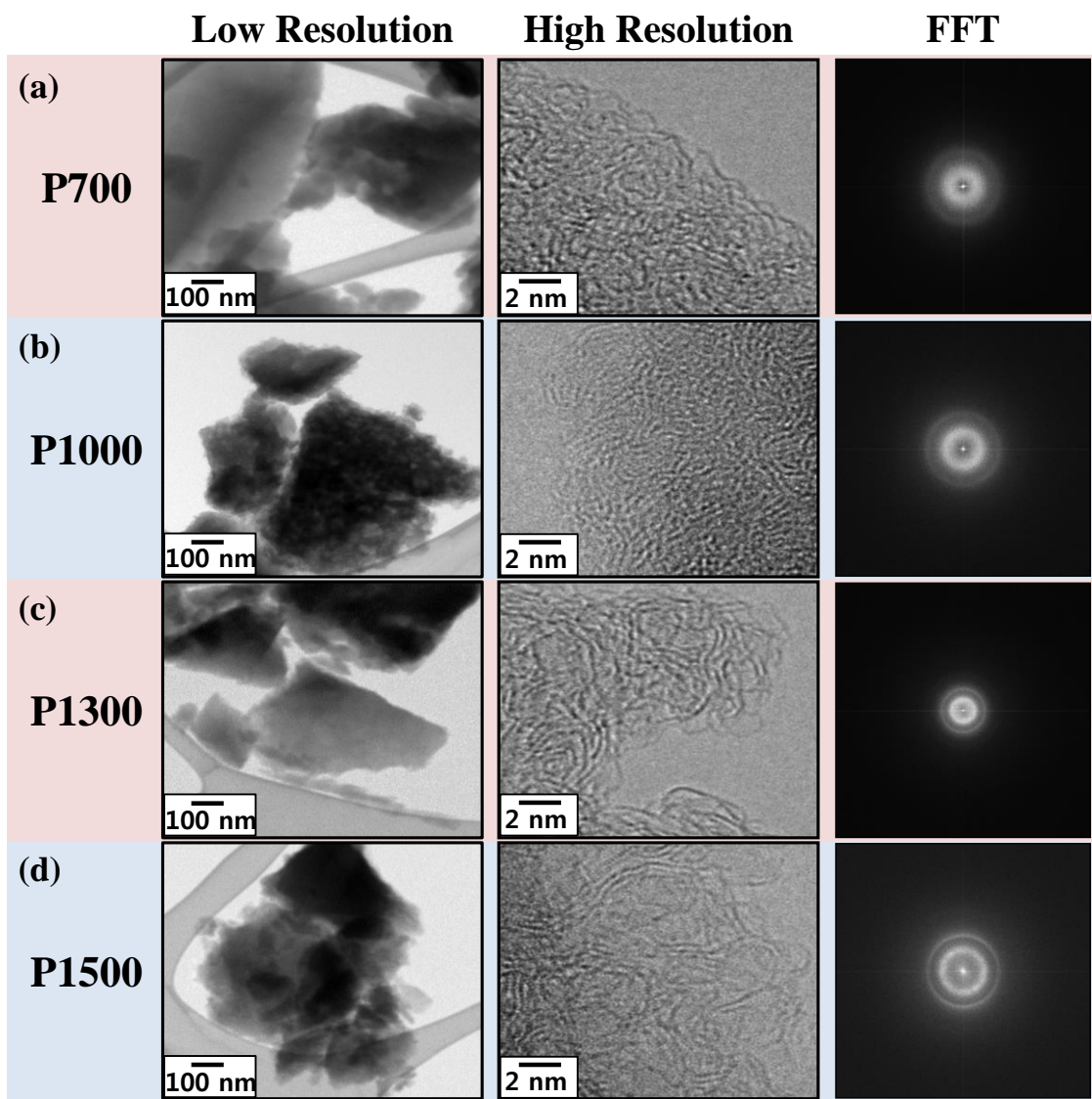


Figure 4.3 Different resolution TEM image and FFT pattern of pistachio shell (a) P700, (b) P1000, (c) P1300, and (d) P1500.

We also performed SAED with a purpose of measuring the variation of $d_{(002)}$ with respect to pyrolysis temperature. Similar to XRD analysis results, the $d_{(002)}$ spacing of pistachio shell-

derived carbon decreased as the pyrolysis temperature increased (Figure 4.4). Although the measured $d_{(002)}$ values by SAED and XRD are slightly different, they show similar tendencies. This difference could be understood by the inherent difference between nano and bulk measurements.

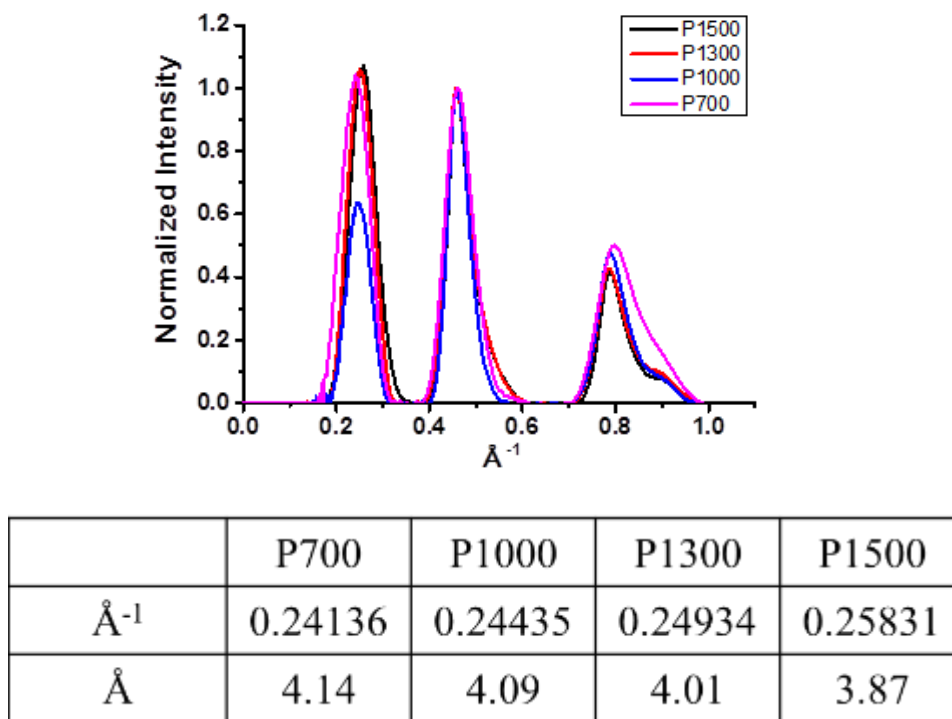


Figure 4.4 Calculation of SAED pixel size of each carbon and its d-spacing value.

4.5.3 Characterization of pistachio shell derived carbon by N_2 adsorption-desorption

Figure 4.5a illustrates the nitrogen adsorption-desorption results for surface area and pore volume as a function of carbonization temperature. The increasing surface area from P700 (444.6 m^2/g) to P1000 (760.9 m^2/g) can be attributed to the decomposition of lignin. As mentioned, lignin decomposes in a range of 250 – 900 $^{\circ}\text{C}$. Thus, at 1000 $^{\circ}\text{C}$, the decomposition of lignin is more likely to be completed than at 700 $^{\circ}\text{C}$ which possibly explains the higher surface area of P1000. At even higher temperatures, the pore structure collapses due to graphitization, yielding a lower surface area (33.1 m^2/g and 16.9 m^2/g for P1300 and P1500 respectively). N_2 adsorption and desorption curves are illustrated in supplementary data (Figure 4.5b).

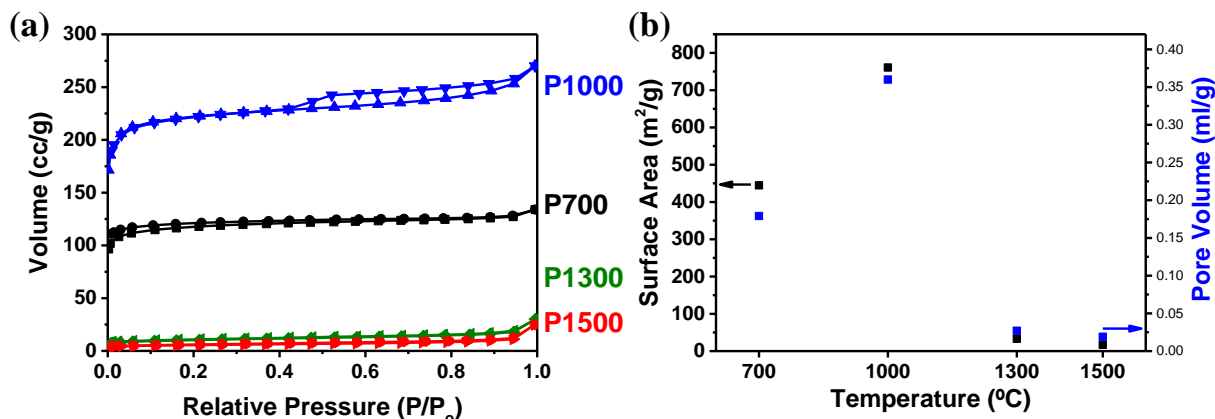


Figure 4.5 (a) N₂ adsorption and desorption curve and (b) surface area and pore volume of each carbonized sample.

4.5.4 Electrochemical characterization

As-prepared carbon materials were tested in a half-cell configuration (vs. sodium metal) with a potential range of 0 – 2 V. Figure 4.6a shows the first charge-discharge curve of each carbon sample. The carbonized samples exhibited an initial sodiation capacity of 267, 312, 300 and 362 mAh g⁻¹ for P700, P1000, P1300 and P1500, respectively; with an initial coulombic efficiency of 58.4%, 71.0%, 74.3% and 74.9%, respectively. The large irreversible capacity loss during the first few cycles can be attributed to the formation of the solid electrolyte interface (SEI) layer at the carbon surface. From Figure 4.5 surface area from P1000 to P1500 decreases while P700 is lower than P1000 but higher than P1300 and P1500. Therefore, rather than surface area playing a role, carbon disorder seems to be the control factor for this CE trend. Moreover, I_D/I_G ratio increases as temperature increases (Figure 4.2b), and this is because of more sp² cluster formation throughout the sample. Here we conclude that the low CE value for lower carbonization temperature sample is due to an amorphous region between the sp² carbon domains or defect sites that traps the Na and results in a low CE value.

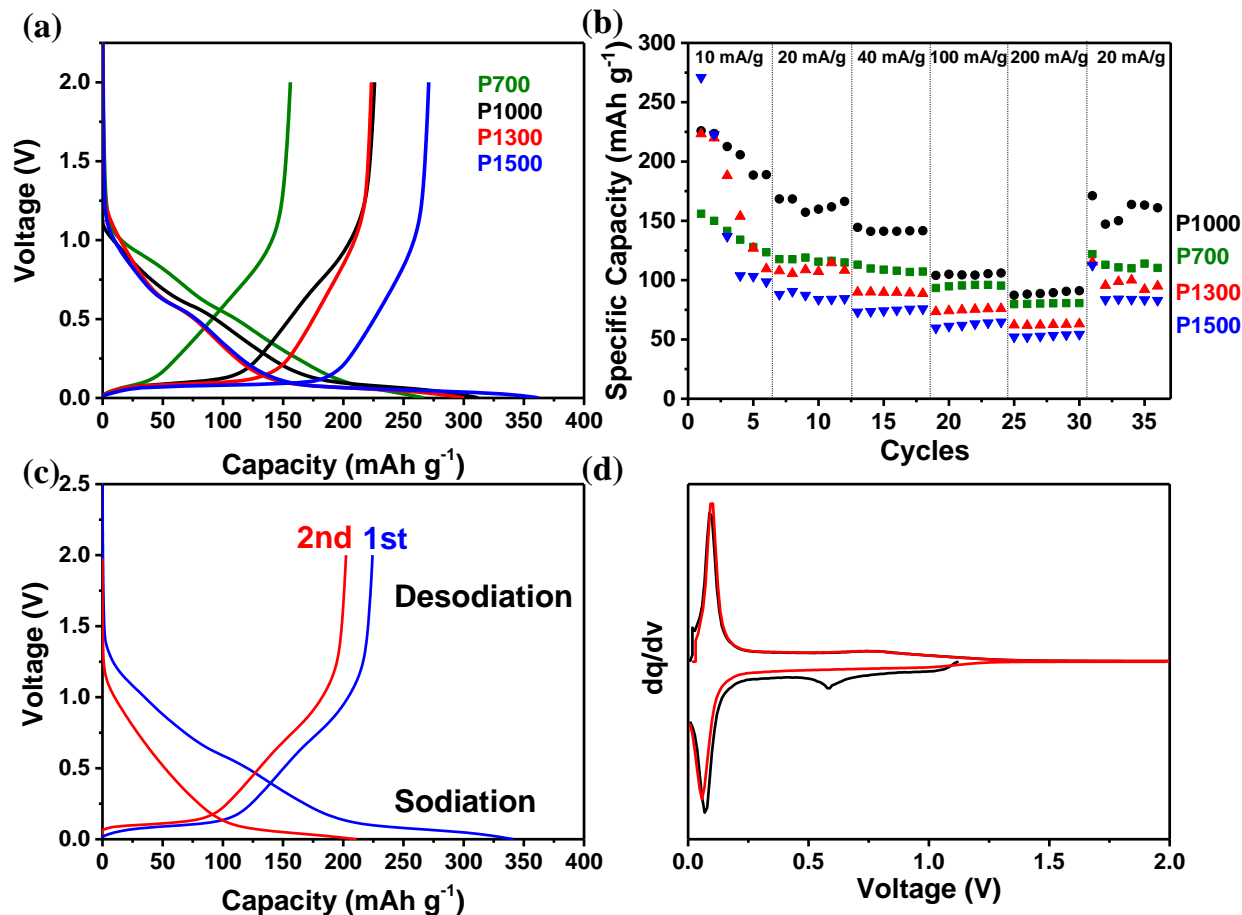


Figure 4.6 (a) First charge-discharge profile of all carbon; (b) desodiation cycling capacity of carbons at different current density; (c) first and second charge-discharge curve of P1000 and (d) dQ/dV of first and second cycle of P1000.

To understand the electrochemical performance of pistachio derived carbon, we describe the voltage profile and rate test result of different carbonization temperature treated pistachio shell (Figure 4.6). Sodium insertion mechanism has been described as follows: a surface heteroatom reacting as adsorption site,⁵³ a “house of cards” model which describes the sodium insertion as nano-pore filling, “nanoplatting”, and sodium ion insertion between graphitic carbon layers,²⁶ and a structural defect sites acting as an adsorption site.³³ Loftabad et al., showed that at higher carbonization temperatures for biomass derived carbon, the low potential region capacity increases in contradiction to the “house of cards” model of sodium storage. Instead of nano-pore filling, they argue that intercalation is the storage mechanism. In addition, the pseudocapacitance effect from

any heteroatoms is introduced as well.³³ Research into carbon based on biomass such as pomelo peel,² peanut shell,⁵⁴ and apple⁴⁰ also agrees that intercalation and heteroatom sites as the primary storage mechanisms for sodium. From Figure 4.6a, it is obvious that the electrochemical profile of each carbon is divided into two stages: the sloping region above 0.2V and the plateau region from 0-0.2 V. Similar profiles for high temperature carbonization were reported.^{31,33,38} As all carbonized sample has defect, the sloping region is a result of defect sites sodium storage.^{38,55} In addition, as carbonization temperature increases, the capacity contribution to the entire capacity from the sloping region decrease. This is attributed from increasing graphitic ordering of the carbon samples. The plateau region capacity of P700, P1000, P1300, and P1500 is 95.76, 161.37, 180.32 and 239.38 mAh g⁻¹ which is 35.8%, 51.7%, 60.0% and 66.1% of the entire discharge capacity, respectively. In addition, at higher carbonization temperature, the porosity of the pistachio shell derived carbon decrease (Figure 4.5) while the plateau region capacity contribution to entire sodiation capacity increases. This result does not fit the “house of cards” model. Figure 4.7 shows desodiation capacity normalized by specific surface area (DSC/SA) of each carbon at various specific current rates. The desodiation capacity chosen here is the final desodiation capacity of each specific current rate. Previously it was shown from XRD and Raman that P700 and P1000 shows similar graphitization. Therefore, higher DSC/SA is due to lower surface area of P700. At higher carbonization temperatures (P1300 and P1500), more ordered structure (high I_D/I_G ratio) is formed throughout the sample and results in higher DSC/SA. Thus, from this result it is possible to assume that more formation and growth of sp² carbon bonding at higher carbonization temperatures provide more storage sites for sodium insertion into the carbon layers. Thus, we attribute the low potential region storage mechanism as sodium insertion in activated carbon layers due to increasing sp² carbon content.

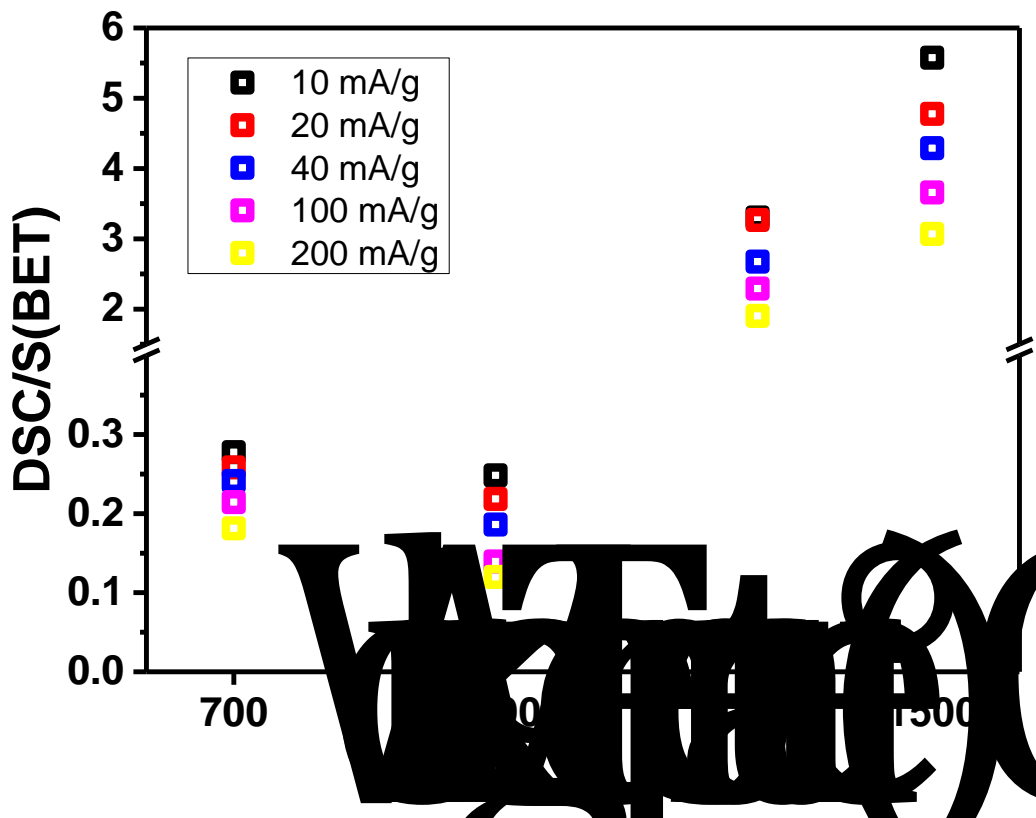


Figure 4.7 Desodiation capacity normalized in respect to surface area for all carbon samples at different current rates.

Surface heteroatom (such as nitrogen and oxygen) and defect sites enable surface redox reactions, commonly known as pseudocapacitance storage mechanism.⁵⁶ To understand possible mechanism further, cyclic voltammetry studies with a scan rates from 0.2 mV s^{-1} to 20 mV s^{-1} was conducted (Figure 4.8). These curves are analyzed with power law type equation: $i = av^b$, where i is current, v is the scan rate, and a , b are adjustable parameters.⁵⁶ Parameter ‘ b ’ determines the plausible storage mechanism of sodium. If the value is $b=0.5$ it is controlled by ideal diffusion Faradaic reaction, i.e. intercalation storage or if the value is $b=1.0$ the material shows capacitance behavior, i.e. pseudocapacitance storage. The parameter b is evaluated by finding the slope of $\log(v)$ vs. $\log(i)$ at different potential region, as shown in Figure 4.8c. From the plot, pseudocapacitance behavior is shown at low potential ($<0.5 \text{ V}$) and high potential ($>1.5 \text{ V}$), while the potential between 0.5 V to 1.5 V shows more intercalation performance. Therefore, the storage mechanism of pistachio derived carbon is originated from defect sites, contributes in the slope

region, intercalation for low potential, and also pseudocapacitance from defect sites and electrode surface. This results correlates to other biomass derived carbon storage mechanism.^{2,33,40,54}

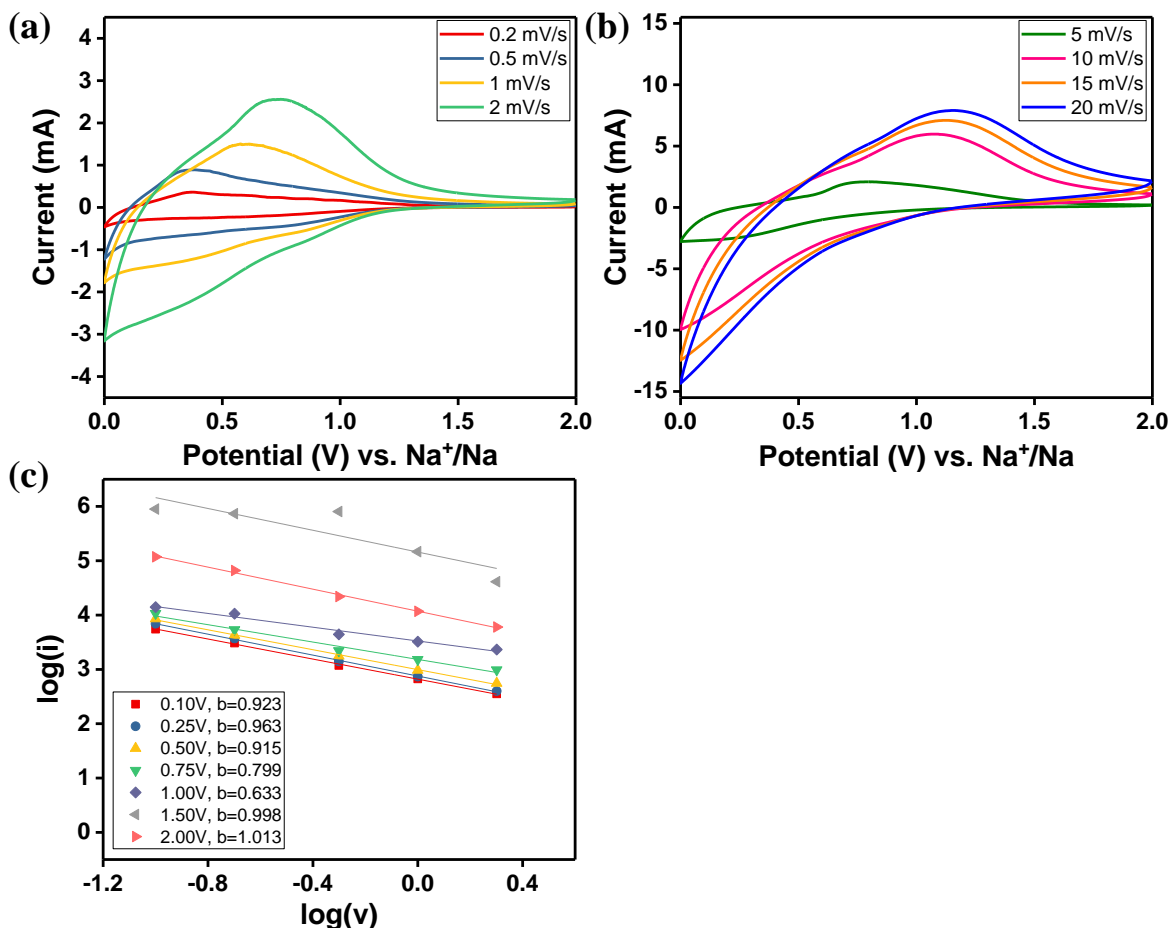


Figure 4.8 Cyclic voltammetry (CV) for pistachio derived carbon cells at different scan rate (a), (b) and plot showing linear relation of $\log(v)$ vs. $\log(i)$ for discharge sweeps from CV.

Figure 4.6b shows the rate test of each carbon sample. The capacity drop at 10 mA/g region can be attributed to the unstable interface between electrode and electrolyte and insufficient penetration of electrolyte within the electrode. Also, at higher pyrolysis temperature, pistachio derived carbon seems to be a more graphitic carbon than the carbon produced at low pyrolysis temperature (Figure 4.2). This phenomenon leads to larger capacity drop of high temperature derived materials as compared to low temperature treated pistachio shell. Two possible factors can be discussed as a reason for P1000 showing the highest performance: dilated interlayer spacing of

carbon layers and high surface area. From Figure 4.9, it is noticeable that the plateau region capacity does not significantly contribute to capacity at high current density. However, P1000 still shows low potential region contribution, while there is nearly no plateau for P1500. At high rate, solid-state diffusion of ion is known to be the limiting factor for ion intercalation.⁵³ The introduction of porosity, however, reduces the solid-state diffusion length due to a thinner carbon wall (compared to macroscopic carbon, which has less porosity). Accordingly, high surface area of P1000 exposes more active storage sites to sodium ion which results in more sodium storage between carbon layers and increase capacity.

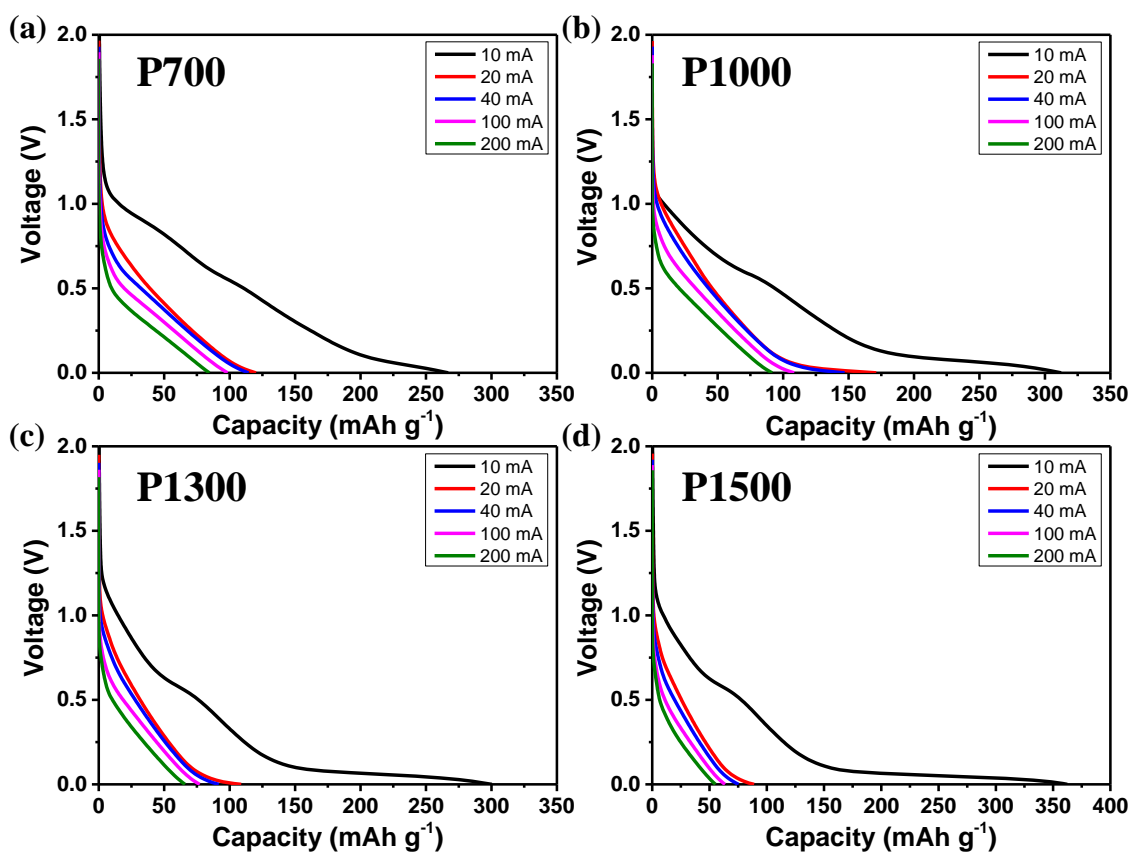


Figure 4.9 Discharge profile of (a) P700, (b) P1000, (c) P1300 and (d) P1500 at different current densities.

P1000 first and second charge-discharge profile is selected to observe the electrochemical characteristic. According to the differential capacity analysis (Figure 4.6c and 4.6d), first discharge

cycle shows a small peak near 0.6-0.7 V. This describes the electrolyte decomposition on carbon surface (SEI layer). Both first and second cycles display a sharp pair of redox peak which is observed at 0-0.2 V. This corresponds to the insertion of sodium ion between disordered carbon layers. In addition, the similarity of the first and second cycle curves reveals the reversibility of our pistachio carbon is reasonable.

Figure 4.10 illustrates the cycling performance of P100 at a rate of C/5 and a potential range of 0-2 V. The coulombic efficiency of P700, P1000, P1300 and P1500 reaches 100%, 99.7%, 99.7% and 100% after the second cycle, respectively. After the initial conditioning test at a current density of 10 mA g^{-1} , each material delivers a capacity of 119.5 , 150.6 , 105.4 and 84.1 mAh g^{-1} at a current density of 40 mA g^{-1} . The capacity retention after 50 cycles are approximately 90.4%, 86.3%, 87.2% and 91.3%, respectively. Since it's a half cell studies (Carbon vs. Na), we demonstrated 50 charge-discharge cycles. Afterword 60 cycles, the capacity fade (Figure 4.11) could result from the deterioration of sodium foil, possibly due to its oxidation (as shown Na foil opened after 100 cycles).

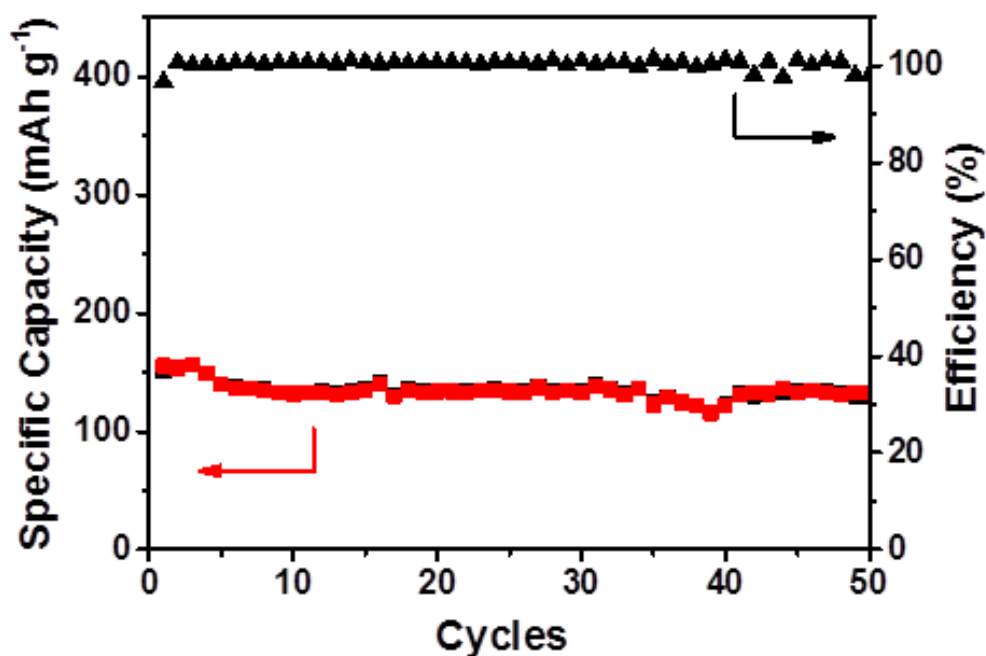


Figure 4.10 Cycle stability test of carbon materials of P1000 at 40 mA g^{-1} current density.

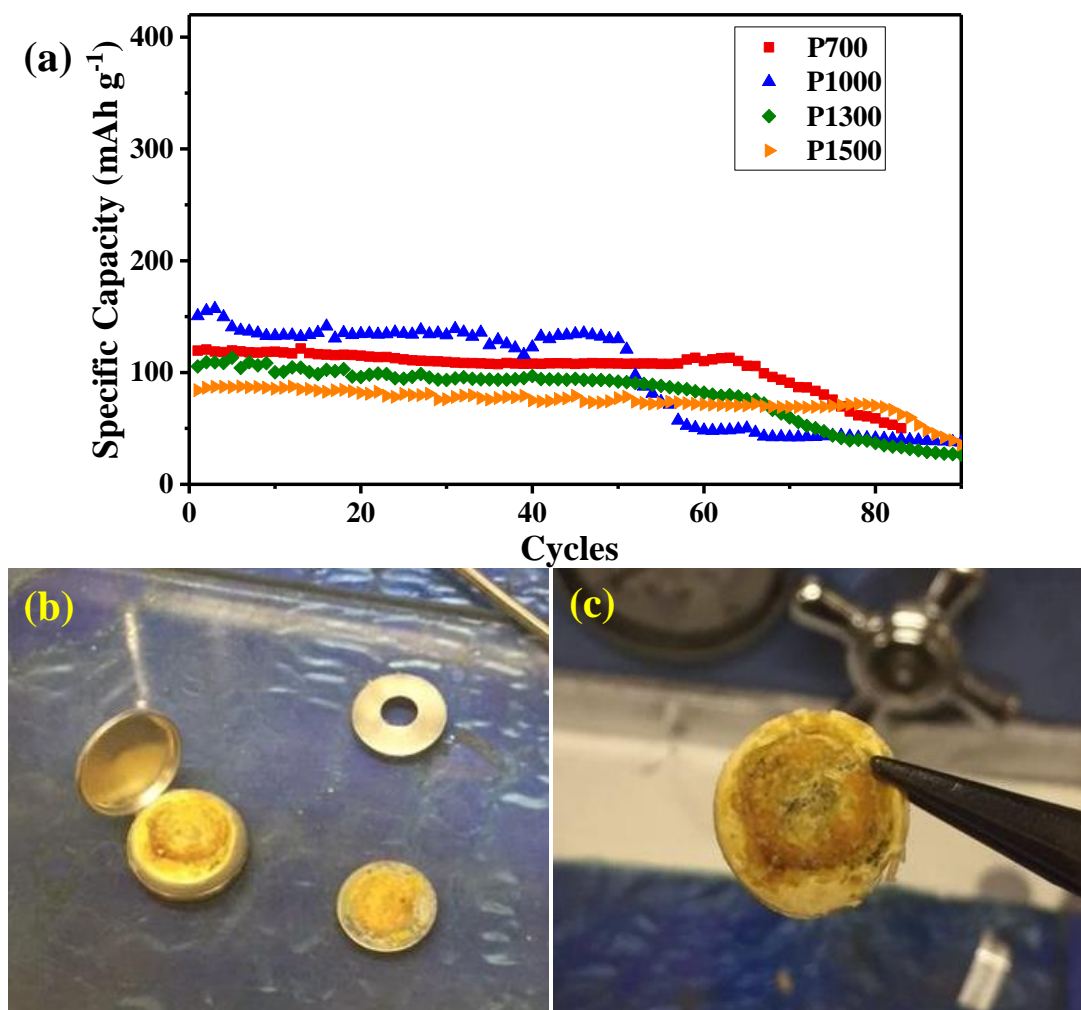


Figure 4.11 (a) Cycle information up to 100 cycles showing the capacity drop and (b), (c) the optical image of deteriorated sodium foil, where the cell was disassembled after capacity drop.

4.6 Conclusion

In this manuscript, carbonaceous anode materials for sodium ion battery were derived from pistachio shell, a common waste biomass. The resulting tailored carbon structure and electrochemical performance were studied as a function of the carbonization temperatures. Carbon samples carbonized at 1000°C demonstrated the best electrochemical performance (225 mAh g⁻¹ at 10 mA g⁻¹) due to its large surface area and reasonable sp² content. Also we suggest a combination of defect sites, sp² content, pseudocapacitance and insertion between larger carbon

layers as a possible storage mechanism for pistachio shell-derived carbon. This result clearly demonstrates that raw bio-waste such as pistachio shell without any pre-treatment, in this study only simple carbonization has been applied, can be applied as a promising anode material for sodium ion battery.

4.7 References

- 1 Palomares, V. *et al.* Na-ion batteries, recent advances and present challenges to become low cost energy storage systems. *Energ Environ Sci* (2012) **5**, 5884-5901, doi:10.1039/c2ee02781j.
- 2 Hong, K. L. *et al.* Biomass derived hard carbon used as a high performance anode material for sodium ion batteries. *J. Mater. Chem. A* (2014) **2**, 12733-12738, doi:10.1039/c4ta02068e.
- 3 Bommier, C. *et al.* Predicting capacity of hard carbon anodes in sodium-ion batteries using porosity measurements. *Carbon* (2014) **76**, 165-174, doi:10.1016/j.carbon.2014.04.064.
- 4 Kang, H. Y. *et al.* Update on anode materials for Na-ion batteries. *J Mater Chem A* (2015) **3**, 17899-17913, doi:10.1039/c5ta03181h.
- 5 Bommier, C. & Ji, X. L. Recent Development on Anodes for Na-Ion Batteries. *Isr J Chem* (2015) **55**, 486-507, doi:10.1002/ijch.201400118.
- 6 Dahbi, M., Yabuuchi, N., Kubota, K., Tokiwa, K. & Komaba, S. Negative electrodes for Na-ion batteries. *Phys Chem Chem Phys* (2014) **16**, 15007-15028, doi:10.1039/c4cp00826j.
- 7 Slater, M. D., Kim, D., Lee, E. & Johnson, C. S. Sodium-Ion Batteries. *Adv Funct Mater* (2013) **23**, 947-958, doi:10.1002/adfm.201200691.
- 8 Abel, P. R., Fields, M. G., Heller, A. & Mullins, C. B. Tin-Germanium Alloys as Anode Materials for Sodium-Ion Batteries. *Acs Appl Mater Inter* (2014) **6**, 15860-15867, doi:10.1021/am503365k.
- 9 Zhu, H. L. *et al.* Tin Anode for Sodium-Ion Batteries Using Natural Wood Fiber as a Mechanical Buffer and Electrolyte Reservoir. *Nano Lett* (2013) **13**, 3093-3100, doi:10.1021/nl400998t.
- 10 Kim, C. *et al.* Long-term cycling stability of porous Sn anode for sodium-ion batteries. *J Power Sources* (2016) **317**, 153-158, doi:10.1016/j.jpowsour.2016.03.060.
- 11 Tang, D. H. *et al.* Room-Temperature Synthesis of Mesoporous Sn/SnO₂ Composite as Anode for Sodium-Ion Batteries. *Eur J Inorg Chem* (2016), 1950-1954, doi:10.1002/ejic.201501441.
- 12 Su, D. W., Ahn, H. J. & Wang, G. X. SnO₂@graphene nanocomposites as anode materials for Na-ion batteries with superior electrochemical performance. *Chem Commun* (2013) **49**, 3131-3133, doi:10.1039/c3cc40448j.
- 13 Liu, Y. H. *et al.* SnO₂ coated carbon cloth with surface modification as Na-ion battery anode. *Nano Energy* (2015) **16**, 399-407, doi:10.1016/j.nanoen.2015.07.010.
- 14 Zhang, D. *et al.* Two-Dimensional Cobalt-/Nickel-Based Oxide Nanosheets for High-Performance Sodium and Lithium Storage. *Chem-Eur J* (2016) **22**, 18060-18065, doi:10.1002/chem.201604115.
- 15 Darwiche, A. *et al.* Better Cycling Performances of Bulk Sb in Na-Ion Batteries Compared to Li-Ion Systems: An Unexpected Electrochemical Mechanism. *J Am Chem Soc* (2012) **134**, 20805-20811, doi:10.1021/ja310347x.
- 16 Zhao, X. *et al.* Antimony/Graphitic Carbon Composite Anode for High-Performance Sodium-Ion Batteries. *Acs Appl Mater Inter* (2016) **8**, 13871-13878, doi:10.1021/acsami.6b01761.

- 17 Wan, F. *et al.* In Situ Binding Sb Nanospheres on Graphene via Oxygen Bonds as Superior Anode for Ultrafast Sodium-Ion Batteries. *Acs Appl Mater Inter* (2016) **8**, 7790-7799, doi:10.1021/acsami.5b12242.
- 18 Zhou, X. S. *et al.* An SbOx/Reduced Graphene Oxide Composite as a High-Rate Anode Material for Sodium-Ion Batteries. *J Phys Chem C* (2014) **118**, 23527-23534, doi:10.1021/jp507116t.
- 19 Zhu, Y. J. *et al.* Red Phosphorus Single-Walled Carbon Nanotube Composite as a Superior Anode for Sodium Ion Batteries. *Acs Nano* (2015) **9**, 3254-3264, doi:10.1021/acs.nano.5b00376.
- 20 Song, J. X. *et al.* Chemically Bonded Phosphorus/Graphene Hybrid as a High Performance Anode for Sodium-Ion Batteries. *Nano Lett* (2014) **14**, 6329-6335, doi:10.1021/nl502759z.
- 21 Zhao, Q. J., Huang, Y. H. & Hu, X. L. A Si/C nanocomposite anode by ball milling for highly reversible sodium storage. *Electrochem Commun* (2016) **70**, 8-12, doi:10.1016/j.elecom.2016.06.012.
- 22 Wang, X. J., Liu, Y. C., Wang, Y. J. & Jiao, L. F. CuO Quantum Dots Embedded in Carbon Nanofibers as Binder-Free Anode for Sodium Ion Batteries with Enhanced Properties. *Small* (2016) **12**, 4865-4872, doi:10.1002/smll.201601474.
- 23 Wang, L. J. *et al.* Porous CuO nanowires as the anode of rechargeable Na-ion batteries. *Nano Res* (2014) **7**, 199-208, doi:10.1007/s12274-013-0387-6.
- 24 Park, Y. *et al.* Sodium Terephthalate as an Organic Anode Material for Sodium Ion Batteries. *Adv Mater* (2012) **24**, 3562-3567, doi:10.1002/adma.201201205.
- 25 Goodwin, A. L. Organic Crystals Packing Down. *Nat Mater* (2010) **9**, 7-8, doi:10.1038/nmat2597.
- 26 Stevens, D. A. & Dahn, J. R. High capacity anode materials for rechargeable sodium-ion batteries. *J Electrochem Soc* (2000) **147**, 1271-1273, doi:10.1149/1.1393348.
- 27 Chen, T. Q. *et al.* Electrospun carbon nanofibers as anode materials for sodium ion batteries with excellent cycle performance. *J Mater Chem A* (2014) **2**, 4117-4121, doi:10.1039/c3ta14806h.
- 28 Pol, V. G. *et al.* Spherical Carbon as a New High-Rate Anode for Sodium-ion Batteries. *Electrochim Acta* (2014) **127**, 61-67, doi:10.1016/j.electacta.2014.01.132.
- 29 Bai, Y. *et al.* Hard Carbon Originated from Polyvinyl Chloride Nanofibers As High-Performance Anode Material for Na-Ion Battery. *Acs Appl Mater Inter* (2015) **7**, 5598-5604, doi:10.1021/acsami.5b00861.
- 30 Ponrouch, A., Goni, A. R. & Palacin, M. R. High capacity hard carbon anodes for sodium ion batteries in additive free electrolyte. *Electrochem Commun* (2013) **27**, 85-88, doi:10.1016/j.elecom.2012.10.038.
- 31 Li, Y. M. *et al.* Amorphous monodispersed hard carbon micro-spherules derived from biomass as a high performance negative electrode material for sodium-ion batteries. *J Mater Chem A* (2015) **3**, 71-77, doi:10.1039/c4ta05451b.
- 32 Kalyani, P. & Anitha, A. Biomass carbon & its prospects in electrochemical energy systems. *Int J Hydrogen Energ* (2013) **38**, 4034-4045, doi:10.1016/j.ijhydene.2013.01.048.
- 33 Lotfabad, E. M. *et al.* High-Density Sodium and Lithium Ion Battery Anodes from Banana Peels. *Acs Nano* (2014) **8**, 7115-7129, doi:10.1021/nn502045y.

- 34 Xing, W. B., Dunlap, R. A. & Dahn, J. R. Studies of lithium insertion in ballmilled sugar carbons. *J. Electrochem. Soc.* (1998) **145**, 62-70, doi:10.1149/1.1838212.
- 35 Babu, R. S. & Pyo, M. Hard Carbon and Carbon Nanotube Composites for the Improvement of Low-Voltage Performance in Na Ion Batteries. *J Electrochem Soc* (2014) **161**, A1045-A1050, doi:10.1149/2.075406jes.
- 36 Shen, F. *et al.* Chemically Crushed Wood Cellulose Fiber towards High-Performance Sodium-Ion Batteries. *Acs. Appl. Mater. Inter.* (2015) **7**, 23291-23296, doi:10.1021/acsami.5b07583.
- 37 Jin, J., Yu, S. J., Shi, Z. Q., Wang, C. Y. & Chong, C. B. Lignin-based electrospun carbon nanofibrous webs as free-standing and binder-free electrodes for sodium ion batteries. *J Power Sources* (2014) **272**, 800-807, doi:10.1016/j.jpowsour.2014.08.119.
- 38 Ding, J. *et al.* Carbon Nanosheet Frameworks Derived from Peat Moss as High Performance Sodium Ion Battery Anodes. *Acs Nano* (2013) **7**, 11004-11015, doi:10.1021/nm404640c.
- 39 Wang, P. Z. *et al.* Fluorine-Doped Carbon Particles Derived from Lotus Petioles as High-Performance Anode Materials for Sodium-Ion Batteries. *J Phys Chem C* (2015) **119**, 21336-21344, doi:10.1021/acs.jpcc.5b05443.
- 40 Wu, L. M., Buchholz, D., Vaalma, C., Giffin, G. A. & Passerini, S. Apple-Biowaste-Derived Hard Carbon as a Powerful Anode Material for Na-Ion Batteries. *Chemelectrochem* (2016) **3**, 292-298, doi:10.1002/celc.201500437.
- 41 Agriculture, U. S. D. o. USDA: Noncitrus Fruits and Nuts Summary. (2016).
- 42 Acikalin, K., Karaca, F. & Bolat, E. Pyrolysis of pistachio shell: Effects of pyrolysis conditions and analysis of products. *Fuel* (2012) **95**, 169-177, doi:10.1016/j.fuel.2011.09.037.
- 43 Xu, J. D. *et al.* Preparing two-dimensional microporous carbon from Pistachio nutshell with high areal capacitance as supercapacitor materials. *Sci Rep-Uk* (2014) **4**, doi:Artn 5545
10.1038/Srep05545.
- 44 Kil, K. C. & Paik, U. Lithium salt of carboxymethyl cellulose as an aqueous binder for thick graphite electrode in lithium ion batteries. *Macromol Res* (2015) **23**, 719-725, doi:10.1007/s13233-015-3094-1.
- 45 Cao, L. Y. *et al.* Rape seed shuck derived-lamellar hard carbon as anodes for sodium-ion batteries. *J Alloy Compd* (2017) **695**, 632-637, doi:10.1016/j.jallcom.2016.11.135.
- 46 Simone, V. *et al.* Hard carbon derived from cellulose as anode for sodium ion batteries: Dependence of electrochemical properties on structure. *J Energy Chem* (2016) **25**, 761-768, doi:10.1016/j.jechem.2016.04.016.
- 47 Mitchell, D. R. G. DiffTools: Electron diffraction software tools for DigitalMicrograph (TM). *Microsc Res Techniq* (2008) **71**, 588-593, doi:10.1002/jemt.20591.
- 48 Gammer, C., Mangler, C., Rentenberger, C. & Karnthaler, H. P. Quantitative local profile analysis of nanomaterials by electron diffraction. *Scripta Mater* (2010) **63**, 312-315, doi:10.1016/j.scriptamat.2010.04.019.
- 49 Acikalin, K. Pyrolytic characteristics and kinetics of pistachio shell by thermogravimetric analysis. *J Therm Anal Calorim* (2012) **109**, 227-235, doi:10.1007/s10973-011-1714-3.
- 50 Tonbul, Y. Pyrolysis of pistachio shell as a biomass. *J Therm Anal Calorim* (2008) **91**, 641-647, doi:10.1007/s10973-007-8428-6.

- 51 Lua, A. C. & Yang, T. Effects of vacuum pyrolysis conditions on the characteristics of activated carbons derived from pistachio-nut shells. *J Colloid Interf Sci* (2004) **276**, 364-372, doi:10.1016/j.jcis.2004.03.071.
- 52 Ferrari, A. C. & Robertson, J. Interpretation of Raman spectra of disordered and amorphous carbon. *Phys Rev B* (2000) **61**, 14095-14107, doi:DOI 10.1103/PhysRevB.61.14095.
- 53 Shao, Y. Y. *et al.* Surface-Driven Sodium Ion Energy Storage in Nanocellular Carbon Foams. *Nano Lett* (2013) **13**, 3909-3914, doi:10.1021/nl401995a.
- 54 Lv, W. M. *et al.* Peanut shell derived hard carbon as ultralong cycling anodes for lithium and sodium batteries. *Electrochim. Acta* (2015) **176**, 533-541, doi:10.1016/j.electacta.2015.07.059.
- 55 Bommier, C., Surta, T. W., Dolgos, M. & Ji, X. L. New Mechanistic Insights on Na-Ion Storage in Nongraphitizable Carbon. *Nano Lett* (2015) **15**, 5888-5892, doi:10.1021/acs.nanolett.5b01969.
- 56 Chen, C. J. *et al.* Na⁺ intercalation pseudocapacitance in graphene-coupled titanium oxide enabling ultra-fast sodium storage and long-term cycling. *Nat. Commun.* (2015) **6**, doi:Artn 6929 10.1038/Ncomms7929.

5. UNIQUE STRUCTURE OF BIOMASS DERIVED CARBON FOR LITHIUM-SULFUR BATTERY

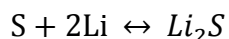
The scientific hypothesis was made by K.Kim and P.J. Kim. All experimental and characterization work was performed by K.Kim. Data analysis was conducted by K.Kim and P.J. Kim. Manuscript writing was performed by K. Kim and P.J. Kim, and revised by Prof. J. P. Youngblood and Prof. V. G. Pol.

The following chapter contains content reproduced with permission from K. Kim, P.J. Kim, J. P. Youngblood, and V. G. Pol., Surface Functionalization of Carbon Architecture with Nano-MnO₂ for Effective Polysulfide Confinement in Lithium-Sulfur Batteries, *Chemsuschem* **2018**, 11, 2375 - 2381. Copyright 2018 John Wiley and sons.

5.1 Introduction to lithium-sulfur batteries

The conventional lithium ion battery (LIB) using LiCoO₂ cathode and graphite anode shows an energy density of 160 Wh kg⁻¹.¹ To meet the recent technologies requirement, next generation energy storage systems such as lithium-sulfur batteries (Li-S), lithium metal batteries, lithium-air batteries, and many other high capacity battery systems are favorable. Among these techniques, Li-S battery shows a high specific capacity of 1672 mAh g⁻¹, specific energy of 2,500 Wh kg⁻¹, and energy density of 2,200 Wh L⁻¹.

The electrochemical reaction of the Li-S battery is:



During discharge, the lithium anode oxidizes and release Li⁺ and electrons, which migrates to sulfur cathode via electrolyte and external circuit. During charge, this process is reversed (Figure 5.1).

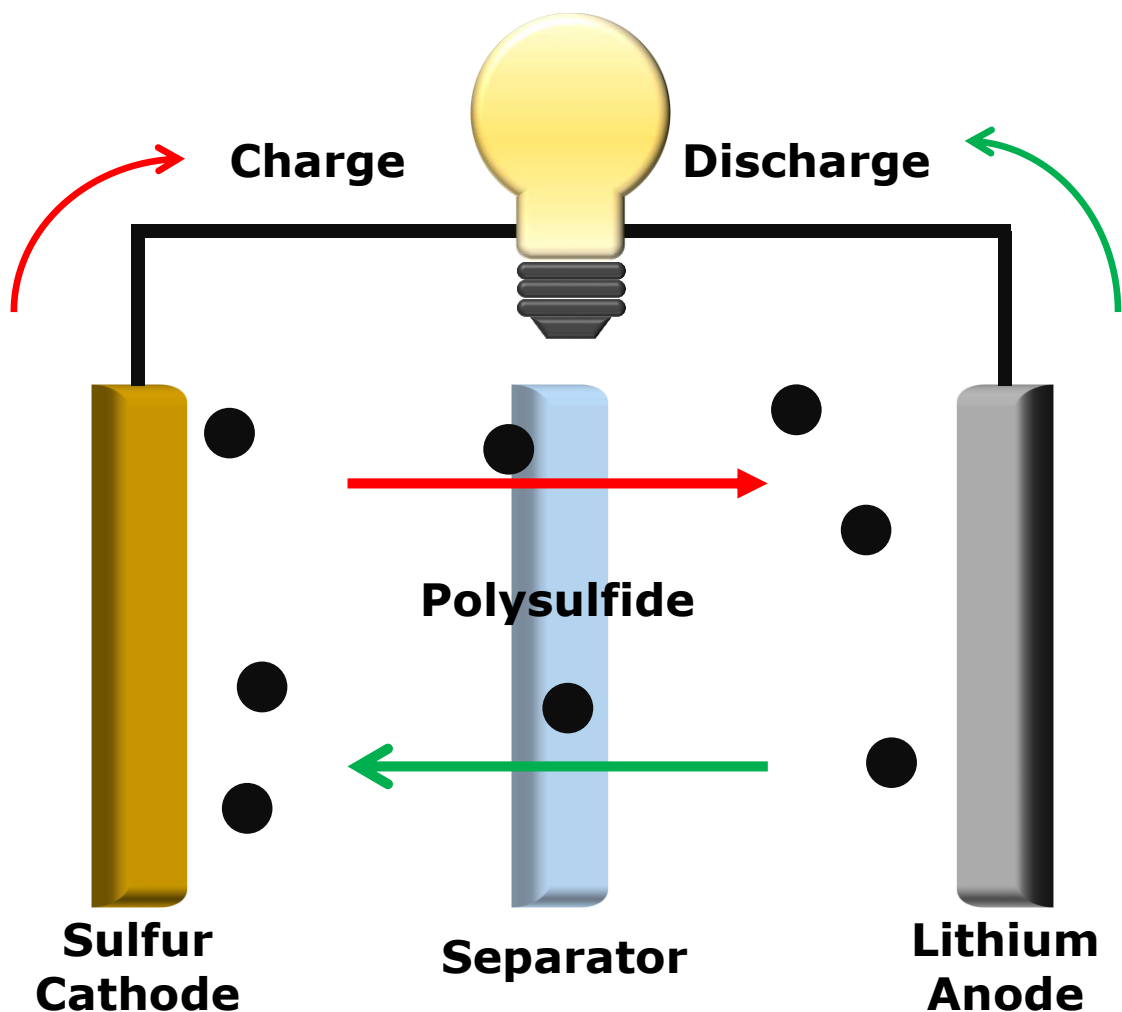
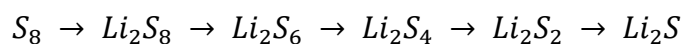


Figure 5.1 Schematic diagram of Li-S battery.

Even though the overall reaction looks simple, the actual chemical reaction inside is complicated. During the cycle process of Li-S battery, solid sulfur element goes through several stage:



The long chain polysulfides (Li_2S_n , $4 \leq n \leq 8$) easily dissolve into electrolyte, while short chain polysulfides (Li_2S_n , $1 \leq n \leq 2$) are insoluble in electrolyte.

5.1.1 Li-S battery challenges

Several issues curb the practical implement of Li-S battery in industries. In terms of sulfur cathode, the electronically insulating sulfur results in poor specific capacities; the long chain polysulfide dissolution into electrolyte leads to continuous loss of active material; the sulfur volume expansion can cause pulverization during repeated charge/discharge cycles. In terms of lithium anode, lithium metal is reactive with electrolyte and form a solid electrolyte interphase (SEI) layer, which leads to consumption of lithium and electrolyte. The high chain polysulfide reaction on lithium anode forms a low chain polysulfide, which does not dissolve into electrolyte and precipitate on the surface of the electrode. This hinders the redox reaction on the electrode and lowers the Coulombic efficiency. Furthermore, continuous growth and breakage of SEI layer can form a lithium dendrite, which can cause internal short circuit, safety hazard, and poor Coulombic efficiency.

5.1.2 Efforts to resolve Li-S battery challenges

To resolve the insulating property of sulfur, sulfur elements are encapsulated in carbon scaffold.^{2,3} Nazar's group has proposed a mesoporous carbon as a sulfur reservoir.⁴ The carbon networks provide an electronic conduit to the active material. Furthermore, the carbon network traps sulfur inside and restricting the polysulfide shuttling, which improves the reversibility of the battery. Numerous efforts to encapsulate sulfur inside various carbon structures including carbon nanotube,⁵ carbon clothes,⁶ and many other carbon scaffold⁷⁻⁹ have been reported.

The most critical issue that deteriorates the performance of Li-S battery is the 'polysulfide shuttling effect'. The high order chain polysulfide (Li_2S_n , $4 \leq n \leq 8$), formed during the reaction of lithium ion and sulfur cathode, dissolves into electrolyte and migrates to lithium anode. On the surface of lithium anode, high order polysulfide forms a low order polysulfide (Li_2S_n , $1 \leq n \leq 2$) which is insoluble to electrolyte. As the insoluble and insulating low order polysulfide precipitate on lithium anode, the overall Li-S battery performance degrades in terms of reversibility and capacity. Electrolyte modification, interface (anode, cathode, separator) modification, and chemical absorption method have been suggested to resolve the polysulfide shuttling. Here, a brief summary of each method is discussed.

The modification of cell components has attracted significant interest due to facile process and improved performance of Li-S battery. In terms of electrolyte modification, Liang and

coworkers modified electrolyte with LiNO_3 additive.¹⁰ They have found that LiNO_3 additive does not influence the redox reaction and the polysulfide diffusion. Instead, the additive form a passive film on lithium anode which improves the cycle efficiency. Liu et. al studied the gel polymer electrolyte (GPE) instead of using liquid electrolyte (LE).¹¹ Author has prepared pentaerythritol tetraacrylate (PETEA)-based GPE which exhibits high ionic conductivity and stable interface with sulfur cathode. GPE successfully restricts the polysulfide shuttling effect and showed an 80% cycle retention after 400 cycles.

Polypropylene (P.P.) separator coating with either polysulfide adsorption or electro-repulsive material is another promising method to resolve polysulfide issue.¹²⁻¹⁴ Yi Cui's group has coated black phosphorus on separator to restrict the polysulfide shuttling and improve the electrical conductivity. The strong bonding between phosphorous and sulfur, good electrical conductivity (300 S m^{-1}), and good lithium ion conductor makes black phosphorus coated separator successful in improving the Li-S battery performance. One of my prior work utilized carbon nanotube (CNT) as an electro-repulsive layer.¹⁵ A pristine CNT, oxidized CNT (O-CNT), and hydrogen reduced CNT (H-CNT) was compared. As a result, O-CNT with more negative charge is more effective in restricting polysulfide shuttling effect.

Another approach is chemical adsorption method using metal oxides.¹⁶ Metal oxides chemically reacts with polysulfide and form thiosulfate, which is insoluble in electrolyte. Thereby, the polysulfide shuttling is effectively suppressed.

5.2 Introduction of current work

Biomass-derived carbon has been widely investigated as a promising energy storage material due to its natural abundance, low cost, and renewability.¹⁷⁻²² In the previous study, Pistachio shell-derived carbon (PC) showed well-interconnected macroporous channels and micropores in the carbon.²³ These structural characteristics enable sulfur loading and physical confinement of polysulfides within micro-/macropores.

In this chapter, we demonstrate an effective strategy of decorating nano- MnO_2 onto the PC scaffold to further capture out-diffused polysulfides via chemical interaction and thereby reactivate the chemically-captured polysulfide species. MnO_2 is reported to have a chemical interaction with polysulfides; this helps to bind the polysulfides and thus improves the cycle stability of sulfur cathode.^{24,25} With the aid of synergistic contributions of the structural benefits of PC and the

uniform decoration of nano-MnO₂ onto the PC scaffold, polysulfide shuttling was noticeably alleviated and the cycling performance of the resultant sulfur cathode was dramatically improved over 250 cycles. Ex-situ studies (e.g. SEM and XRD) and Raman analysis were carried out in order to further characterize the positive effects of nano-MnO₂ on capturing polysulfides during repetitive electrochemical reactions.

5.3 Experimental

5.3.1 Preparation of pistachio shell-derived carbon (PC)

Fresh pistachio shells were washed with DI water several times to remove salt and other contaminants followed by drying inside a vacuum oven overnight at 80 °C. A crucible filled with cleaned pistachio shells was placed inside a furnace (OTF-1200X, MTI corp.) and heated to 1000 °C at a heating/cooling rate of 5 °C min⁻¹ and maintained for 2 hours under Ar flow. As-prepared pistachio shell-derived carbon (PC) were ball-milled (8000M Mixer/Mill, SPEX Sample Prep) for 10 min and stored in a glass vial.

5.3.2 Fabrication of nano-MnO₂ decorated pistachio shell-derived carbon (M-PC)

PC and 0.001M KMnO₄ (Sigma Aldrich) solution in DI water were added to a glass vial at a mass ratio of 1:10. Subsequently, the vial was placed inside an oven set at 80 °C for 2 hours. As-prepared nano-MnO₂ decorated PC (M-PC) was washed with DI water at least 3 times and dried inside an oven for 6 hours.

5.3.3 Preparation of sulfur cathode electrode (M-PC/S and PC/S)

As-prepared PC (or M-PC) and sulfur was loaded inside a stainless steel container with a mass ratio of 30:70. The container was sealed and located inside a vacuum oven set at 155 °C and maintained for at least 12 hours to provide sufficient time to impregnate the sulfur within the macroporous channels and micropores via capillary force. As-prepared samples were ground (mortar and pestle grinding) and then ball-milled to obtain fine powders (termed, PC/S or M-PC/S). A slurry was prepared by dispersing 80 wt. % sulfur composite, 10 wt. % PVDF, and 10 wt. % Super P into NMP by planetary mixer (Thinky, 10 mins at 2000 rpm). As-prepared slurry was casted on an aluminum foil using an automated doctor blade. Subsequently, the film was dried at 50 °C in vacuum for 10 hours. After drying, the film was punched into a half-inch

diameter disc. The cell was assembled into 2032-type coin cell. Lithium metal (Alfa Aesar) as a counter-electrode, 1 M bis(trifluoromethane) sulfonamide lithium (1.0 M LiTFSI in DIOX/DME = 50/50, Sigma Aldrich) with LiNO₃ additive (1 wt. %) as electrolyte, and Cellgard 2500 as a separator were used in the cell assembly.

5.3.4 Material characterization

Scanning electron microscopy (SEM, FEI quanta 3D FED dual-beam at 10 kV) was utilized to image the morphology of PC and M-PC. The Brunauer-Emmett-Teller (BET) surface area and pore size was measured by N₂ adsorption-desorption (Qunatachrome Nova 2200e). Raman spectroscopy (Renishaw, InVia Raman microscope) and X-ray diffraction (XRD, Rigaku at 40 kV and 44 mA) techniques were used to study crystallographic nature of materials. Galvanostatic charge-discharge cycling was measured by a BST8-MA device (MTI Corporation) in the potential range of 1.5 – 3.0 V vs. Li⁺/Li. Electrochemical impedance spectroscopy (EIS) were conducted using a Gamry Reference 600 Electrochemical Workstation. Measurements were conducted over a frequency range from 1 MHz to 0.01 Hz. TGA analysis was further conducted to measure the loading mass of MnO₂ in M-PC/S-chem (Figure S6). The first drop near 220 °C indicates the amount of sulfur (70%), which agrees with the initial sulfur amount impregnated in M-PC. The remaining weight after carbon burn-out is 2.8 wt.%, which is 3.1 wt.% MnO₂ loading in M-PC/S-chem. The TGA result describes successful impregnation of sulfur in M-PC and decoration of MnO₂.

5.4 Results and discussion

Figure 1 illustrates the schematic concept of utilizing nano-MnO₂ as polysulfide anchoring agent in Li-S batteries. Previously, it was reported that PC scaffold has numerous macroporous channels and micropores in its carbon structure.²³ These structural benefits of PC not only facilitate effective penetration of electrolyte into macroporous channels but also physically confine polysulfides into micropores. However, during repetitive electrochemical reaction, polysulfides which were loosely confined within micropores start to diffuse into the electrolyte due to the poor chemical affinity with non-polar carbon scaffold (Figure 5.2a). By decorating nano-MnO₂ onto the PC scaffold (M-PC), the out-diffused polysulfides were further captured and reactivated by

forming thiosulfate bonds with nano-MnO₂, contributing to the improved cycle performance of sulfur cathode electrode (Figure 5.2b).

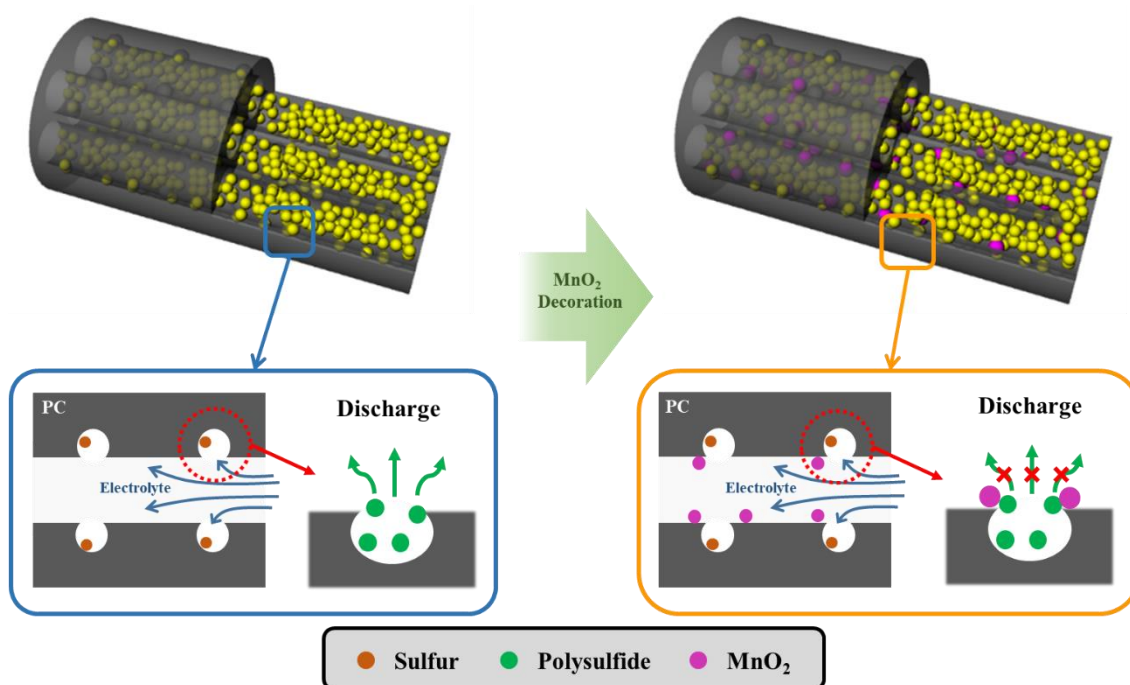
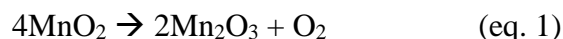


Figure 5.2 Schematic diagram. The electrochemical behaviors of (a) PC/sulfur electrode and (b) M-PC/sulfur electrode during discharge.

Figure 5.3a shows the photographs of pistachio shell before and after carbonization process. After pyrolysis, pistachio shells turned black and still maintained the structure without serious collapse and deformation. To characterize the morphologies of pyrolyzed pistachio shell, top-view and cross-sectional SEM analysis were carried out. Top-view SEM image shows an uneven and rough surface throughout the entire area, exhibiting numerous macro pores with sizes of $\sim 5\ \mu\text{m}$ (Figure 5.4a). Cross-sectional SEM shows interconnected macroporous channels throughout the PC scaffold (Figure 5.4b). The size of channel is also $\sim 5\ \mu\text{m}$ (inset of Figure 5.4b). An electrolyte permeability test was conducted by dropping electrolytes onto PC scaffold. Three drops of electrolyte were fully infiltrated inside the structure of PC scaffold. This result directly corroborates that PC has a favorable architecture to enable the efficient penetration of electrolyte into the macroporous channels (Figure 5.5). Surface area and pore size distribution of PC was

carried out and are presented in Figure 5.3b. The surface area of PC is as high as $384 \text{ m}^2 \text{ g}^{-1}$ and the distribution of pore size mostly ranges from 1 to 2 nm, indicative of a microporous structure. For further characterization of PC after nano-MnO₂ decoration (M-PC), XRD, TGA, BET, and EDS mapping were carried out. The X-ray diffraction (XRD) pattern of pristine PC shows two diffraction peaks centered at 23° and 44° , corresponding to typical amorphous carbon (002) and (100) crystal plane, respectively (Figure 5.3c). After nano-MnO₂ decoration, new peaks appeared at 13° , 25° , 37° , and 65° , which are consistent with (001), (002), (111), and (020) miller indices (JCPDS 42-1317), respectively. To determine the approximate ratio of MnO₂ to PC, thermogravimetric analysis (TGA) was conducted under air flow (Figure 5.3d). The transformation of MnO₂ to Mn₂O₃ under air atmosphere is previously reported (Equation 1).²⁶⁻²⁹



The loading mass of MnO₂ is 9.0% of the total mass of M-PC, which is estimated by considering the transition from MnO₂ to Mn₂O₃ (8.2 %) at 800°C . The TGA result for PC shows no remaining residue after reaching 800°C . As shown in Figure 5.3f, nanosheet-structured MnO₂ (pointed with yellow arrow) covered the entire surface of PC after decorating nano-MnO₂. This could be differentiated by the top-view SEM image of pristine PC (Figure 5.3e). In order to clearly determine and characterize the distribution of MnO₂ throughout the surface of PC, energy dispersive spectroscopy (EDS) mapping was further conducted (Figure 2g). The EDS analysis confirms the presence of Mn and O elements throughout the entire PC scaffold (Figure 5.3g), indicating the successful decoration of MnO₂.^{30,31} Further TEM studies confirmed the successful decoration of nano-MnO₂ on PC scaffold. The TEM image of pristine PC shows amorphous carbon structure (Figure 5.3h), while that of M-PC shows wrinkled structure which indicates the successful decoration of nano-MnO₂ (Figure 5.3i).³²

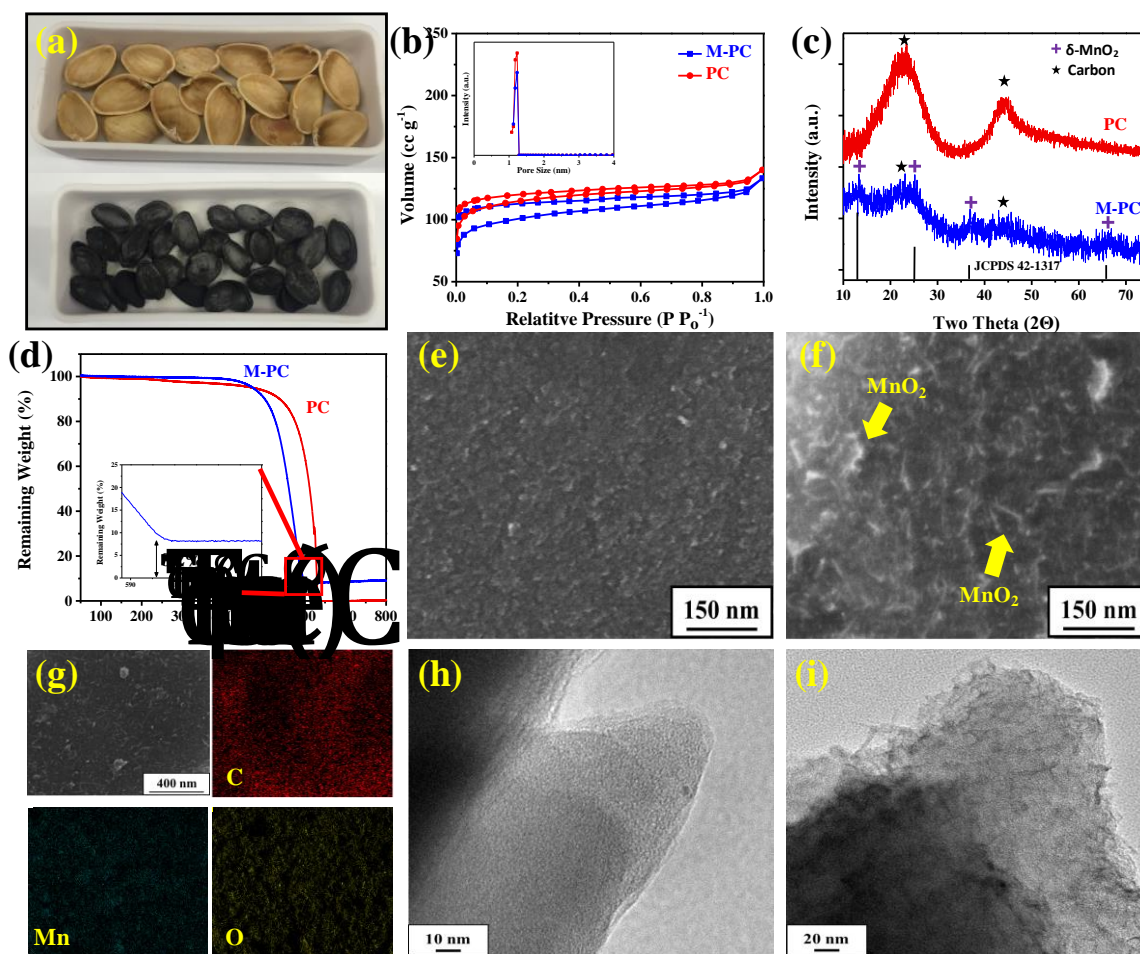


Figure 5.3 Characterization of PC and M-PC. (a) Before and after pyrolysis of pistachio shell; confirmation of nano-MnO₂ decoration by (b) BET, (c) XRD, (d) TGA; SEM images of (e) pristine PC and (f) M-PC (MnO₂ is indicated by yellow arrow); (g) EDS mapping; TEM images of (h) pristine PC and (i) M-PC (wrinkled structure).

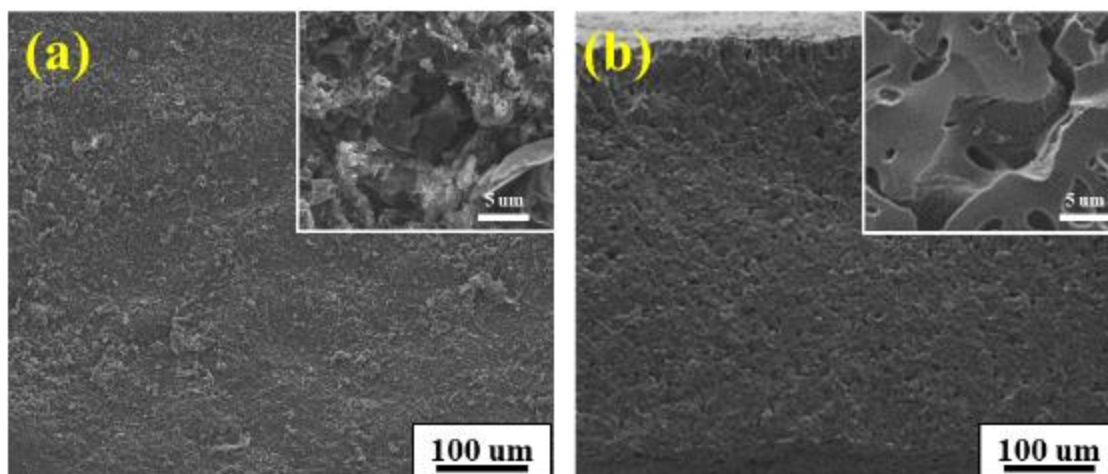


Figure 5.4 The (a) top-view and (b) cross-sectional view SEM image of pistachio derived carbon.

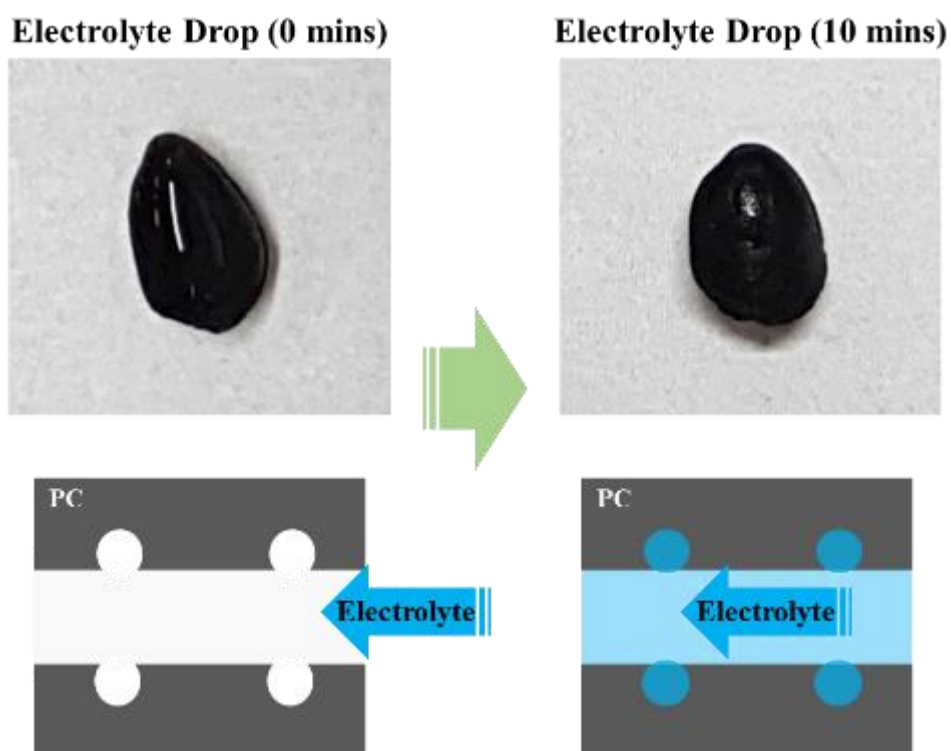


Figure 5.5 Electrolyte permeability test on the PC substrate. Total 3 drops of electrolyte was fully percolated into the PC substrate after 10 min.

In order to validate the benefits of chemical decoration of nano-MnO₂ onto PC scaffold in terms of electrochemical properties, PC scaffold was physically mixed with MnO₂ particles and sulfur (M-PC/S-phy.) as a comparison electrode and was evaluated and compared in Figure 5.6. An equal amount of MnO₂ was added for the direct comparison with the PC scaffold chemically anchored with nano-MnO₂ (M-PC/S-chem.). Figure 5.6a-b depicts the schematic of two electrodes during electrochemical reaction. The M-PC/S-chem. has close contact between the nano-MnO₂ and carbon, thus facilitating effective electron transport and enhanced redox reaction kinetics (Figure 5.6b). On the contrary, physically isolated MnO₂ with poor electrical conductivity is unfavorable to provide the efficient conductive pathway for active materials and chemically-trapped polysulfides, thus leading to low utilization of sulfur and poor cycle stability (Figure 5.6a). The 1st and 100th charge/discharge voltage profiles are compared to show the polarization difference of M-PC/S-chem. and M-PC/S-phy. Both cells were cycled at 1 C. The voltage profiles of M-PC/S-chem. exhibits a smaller polarization (400 mV) than the M-PC/S-phy. (460 mV). This indicates that chemical decoration of nano-MnO₂ onto the conductive scaffold can more effectively facilitate the reversible electrochemical redox reaction than the physically mixed electrode (Figure 5.6c-d).³³ The M-PC/S-chem. showed a cycle retention of 80% and high discharge capacity over 100 cycles at a current density of 1C. In contrast, M-PC/S-phy. showed a relatively low capacity and poor cycle retention (65 % of initial capacity) (Figure 5.6e). Extrapolating from the obtained results, the direct decoration of functional inorganic materials (such as nano-MnO₂) onto a conductive scaffold via chemical decoration improves the electrochemical performance and stabilizes the electrochemical reactions of Li-S batteries over a physical mixed electrode.

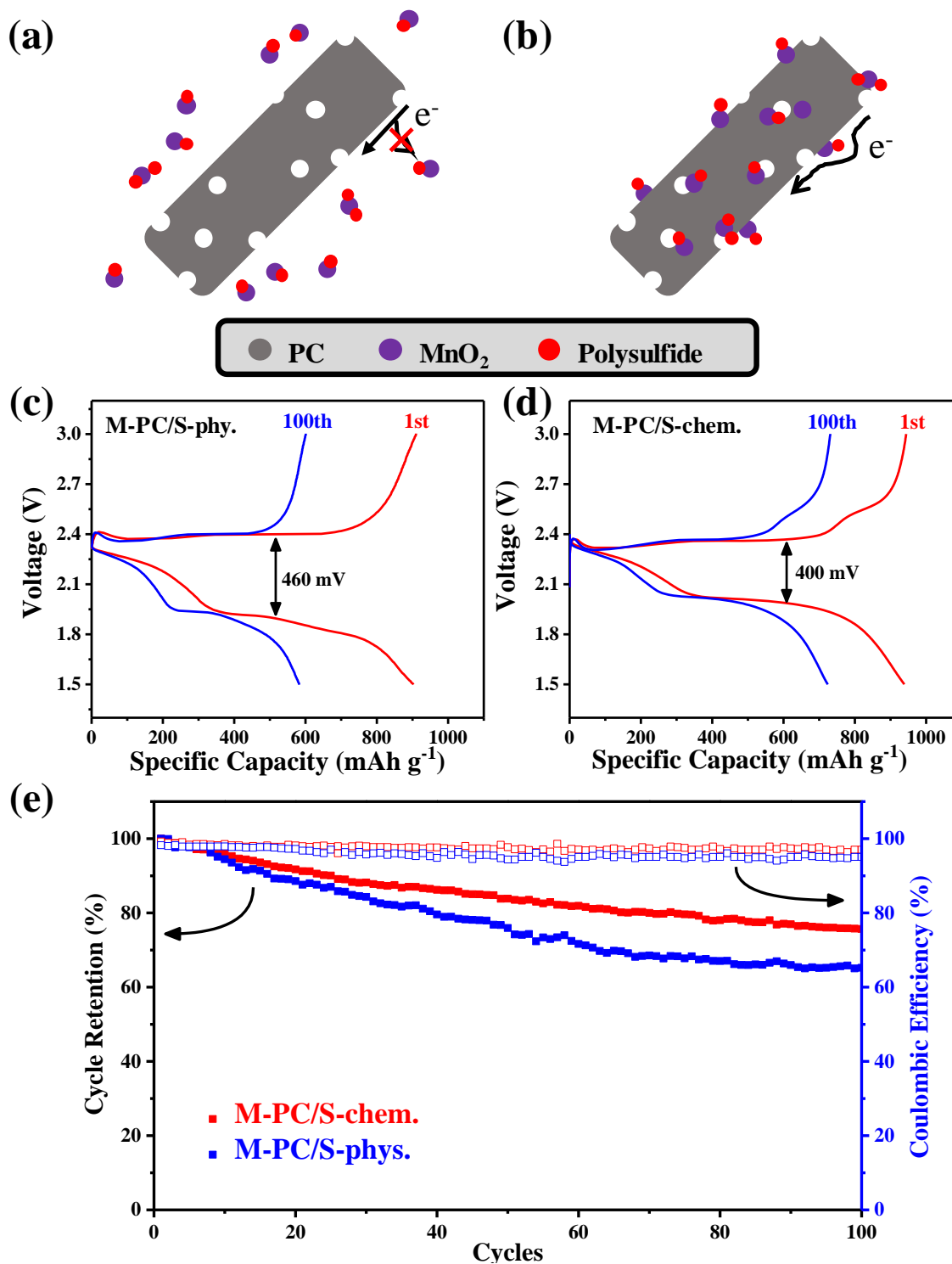


Figure 5.6 Electrochemical performances of M-PC/S-phy. and M-PC/S-chem. Schematic diagram of (a) M-PC/S-phy. and (b) M-PC/S-chem. during discharge/charge; voltage profiles of (c) M-PC/S-phy. and (d) M-PC/S-chem. at 1st and 100th cycles; (e) cycle performance with Coulombic efficiency at a current density of 1 C.

To ascertain the effect of nano-MnO₂ on long-term electrochemical stability, electrochemical performances of PC/S and M-PC/S electrodes were evaluated and are presented in Figure 5.7. Long-term cyclability of these two electrodes were evaluated at 0.5 C over 250 cycles (Figure 5.7a). The M-PC/S showed a much higher cycle retention (62 %) than PC/S (45 %) over 250 cycles, which is attributed to the synergistic contribution of the structure of PC and the chemical decoration of nano-MnO₂. To confirm the influences of nano-MnO₂ decoration on the rate capabilities of the sulfur cathode, each electrode was evaluated at different current densities from 0.5 to 4 C (Figure 5.8). The PC/S electrode delivered relatively low rate capabilities at current densities from 0.5 to 4 C. In contrast, the M-PC/S electrode showed higher reversible discharge capacities of 1163, 984, 795, and 422 mAh g⁻¹ as current densities increase from 0.5 to 4 C, respectively. In addition, the voltage profiles of PC/S and M-PC/S at different current rate showed noticeable differences in voltage hysteresis. The polarization gap of M-PC/S increased from 280 mV (at 0.5 C) to 430 mV (at 2 C), whereas that of PC/S became a bit wider from 320 mV (at 0.5 C) to 620 mV (at 2C), which directly supports that nano-MnO₂ helps to activate more polysulfide species and enable the reversible reactions. This is ascribed to two main benefits of M-PC: a) physical confinement of polysulfides within the micropores of PC scaffold and b) the further capture of polysulfides via chemical interaction of nano-MnO₂. The charge/discharge curves of both PC/S and M-PC/S at the 1st and 250th cycles are shown in Figure 5.7b and 5.7c. Both voltage profiles showed typical sulfur electrode behaviors with two plateau regions (2.3V and 2.1V, which is contributed from high and low order polysulfide reduction, respectively). Interestingly, there is a clear difference in the length of plateau region (2.3V), which is associated with high-order polysulfide reduction, after 250 cycles. The PC/S showed a drastic decrease of length (58% drop) after 250 cycles, implying that large amount of high-order polysulfides was dissolved into the electrolyte and not further reactivated by the conductive PC scaffold. On the other hand, the M-PC/S exhibited relatively small decrease of length (34 %) after 250 cycles. This clearly explains that nano-MnO₂ effectively holds high-order polysulfides by chemical interaction. In addition, the Nyquist plots showed clear differences in the diameter of the semi-circle, corresponding to charge transfer resistance, as the cycle number increased.³⁴ The M-PC/S showed a significantly small increase of charge transfer from 1st to 100th cycle, compared to the PC/S (Figure 5.7d and 5.7e). This strongly supports that nano-MnO₂ facilitates the improved redox kinetics and aids to stabilize the cycle performances by suppressing polysulfide shuttling.

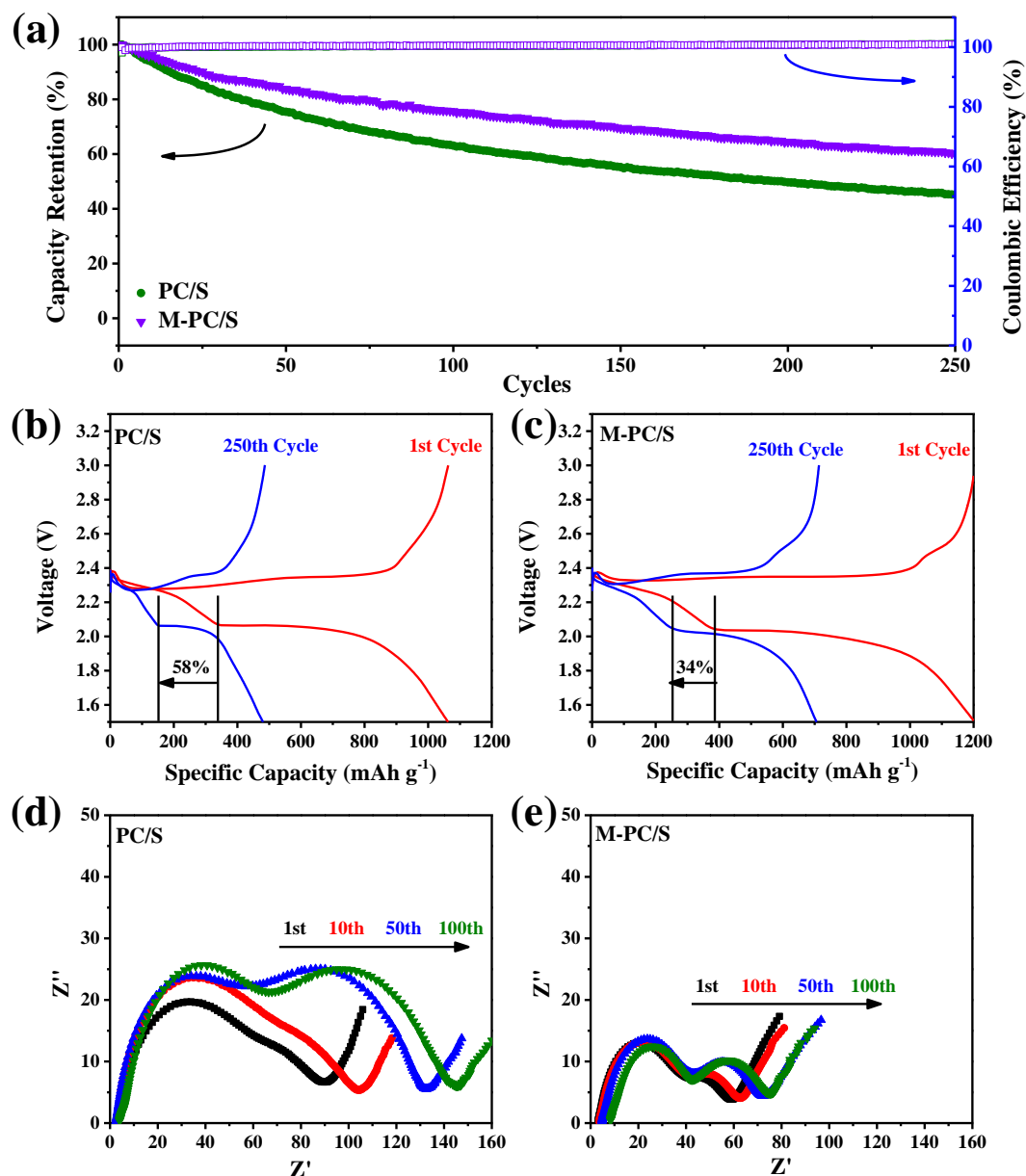


Figure 5.7 Long-term electrochemical performances of PC/S and M-PC/S. (a) Cycle performance of PC/S and M-PC/S at a current density of 0.5 C; (b) voltage profiles of PC/S and (c) M-PC/S 1st and 250th cycle; EIS studies of (d) PC/S and (e) M-PC/S at different cycle numbers.

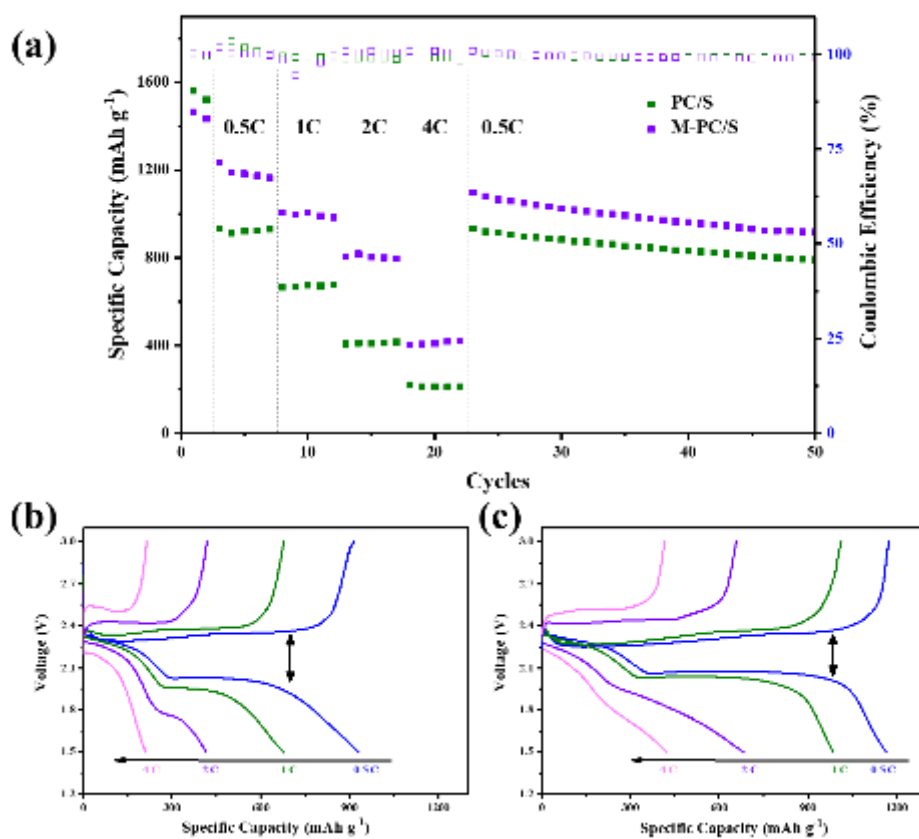


Figure 5.8 Rate study of before/after decoration of MnO₂ on PC (a) and a voltage profile at difference C-rates of PC (b), M-PC (c).

To investigate polysulfide interaction with nano-MnO₂, polysulfide absorption tests were carried out by soaking the PC and M-PC in a polysulfide solution (Li₂S₈) followed by washing with fresh electrolyte. The polysulfide solution was prepared by following reported study.³⁵ Raman spectroscopy was utilized to measure the peak shift of binding energy after polysulfide absorption.³⁶ During discharge, the polysulfide species diffused out of PC/S electrode migrated towards the anodic side without any blocking, whereas the polysulfides dissolved out of M-PC/S were chemically captured by nano-MnO₂ (Figure 5.9a and 5.9b). Before and after polysulfide absorption test, PC showed analogous Raman peak positions located at 1320 cm⁻¹ (D) and 1590 cm⁻¹ (G), corresponding to amorphous carbon and graphitized carbon, respectively. This implies that PC itself has no binding affinity with polysulfide (Figure 5.9c). In contrast, M-PC presented an additional peak at 650 cm⁻¹, which is associated with Mn-O lattice vibration.³⁷ After polysulfide absorption, the band assigned to Mn-O lattice vibration was red-shifted and a peak around 480 cm⁻¹ appeared due to the formation of thiosulfate.²⁴ In addition, M-PC/Phys. polysulfide adsorption test was conducted to confirm the effect of MnO₂ (Figure 5.10). M-PC/Phys. showed a red-shifted Mn-O lattice vibration and a thiosulfate peak which is analogous to M-PC/Chem. results. This result directly provides concrete evidence for the effect of nano-MnO₂ as polysulfide anchoring agents.

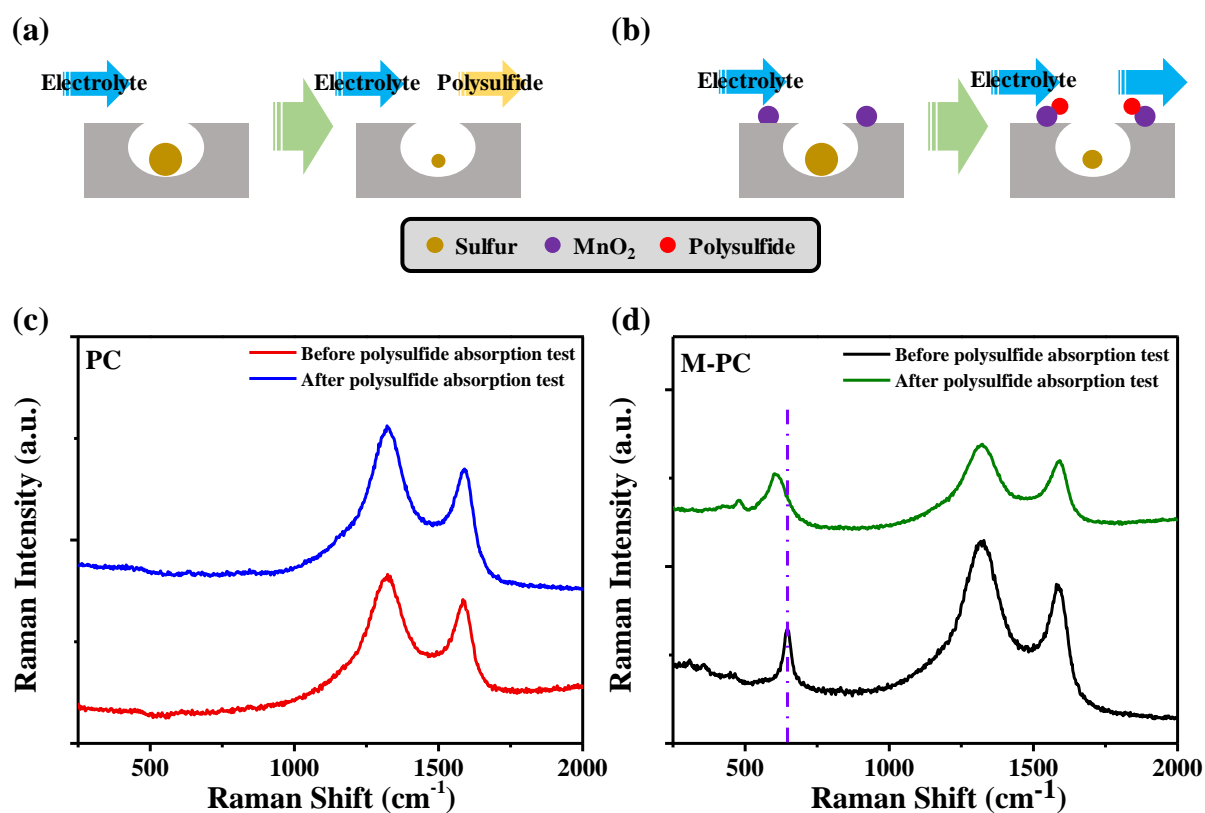


Figure 5.9 Raman spectroscopy before and after polysulfide absorption test. Schematic diagram to illustrate the role of (a) PC and (b) M-PC during electrochemical tests. Raman spectra for (c) PC and (d) M-PC before and after polysulfide absorption.

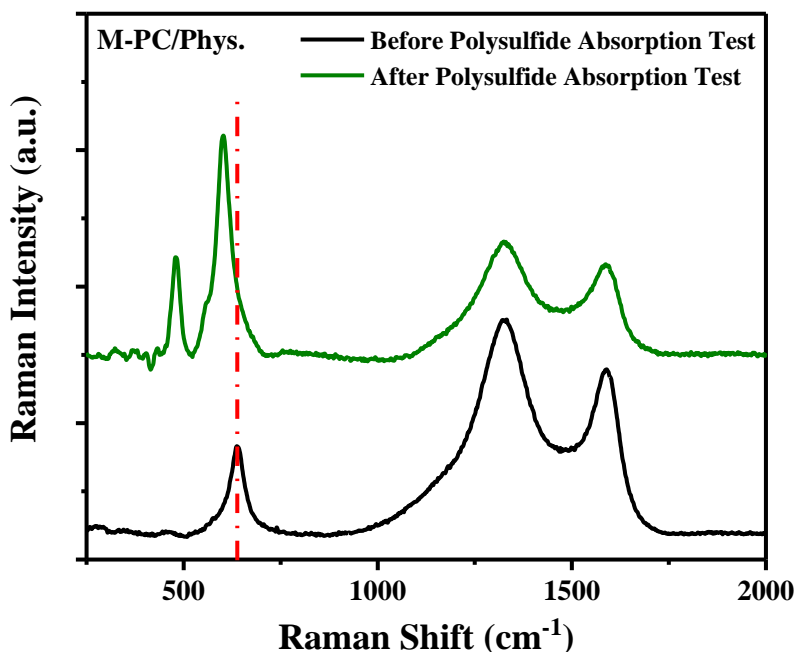


Figure 5.10 Polysulfide absorption test of M-PC/Phys.

Cells were disassembled after cycles in order to investigate the effect of nano- MnO_2 on the suppression of polysulfide shuttling. Figure 5.11 presents the photographs and SEM images of lithium foil after 250 cycles. The lithium foil evaluated with PC/S showed black spots and protrusion on localized areas (Figure 5.11a), while that with M-PC/S exhibited relatively smooth and uniform topography throughout the entire area (Figure 5.11b). SEM and X-ray photoelectron spectroscopy (XPS) analysis were performed to characterize the morphology and chemical composition of black spots on the Li foil from the PC/S cell. The SEM image of black spots shows a rough and uneven surface morphology (Figure 5.11c). In contrast, the SEM image of the Li metal foil from the M-PC/S cell presents conformal topography without any noticeable agglomerates of polysulfides over the surface (Figure 5.11d). The XPS spectrum of the PC/S black spots shows two peaks centered at S $2p_{3/2}$ (162 eV) and S $2p_{3/2}$ (161 eV), which corresponds to a chemical shift indicating Li_2S_2 and Li_2S (Figure 5.12).³⁶ These results strongly support that nano- MnO_2 effectively aids to curb the diffusion of polysulfide towards Li metal

foil, thereby protecting Li metal from side reactions and improving the cycle performance of Li-S batteries.³⁸

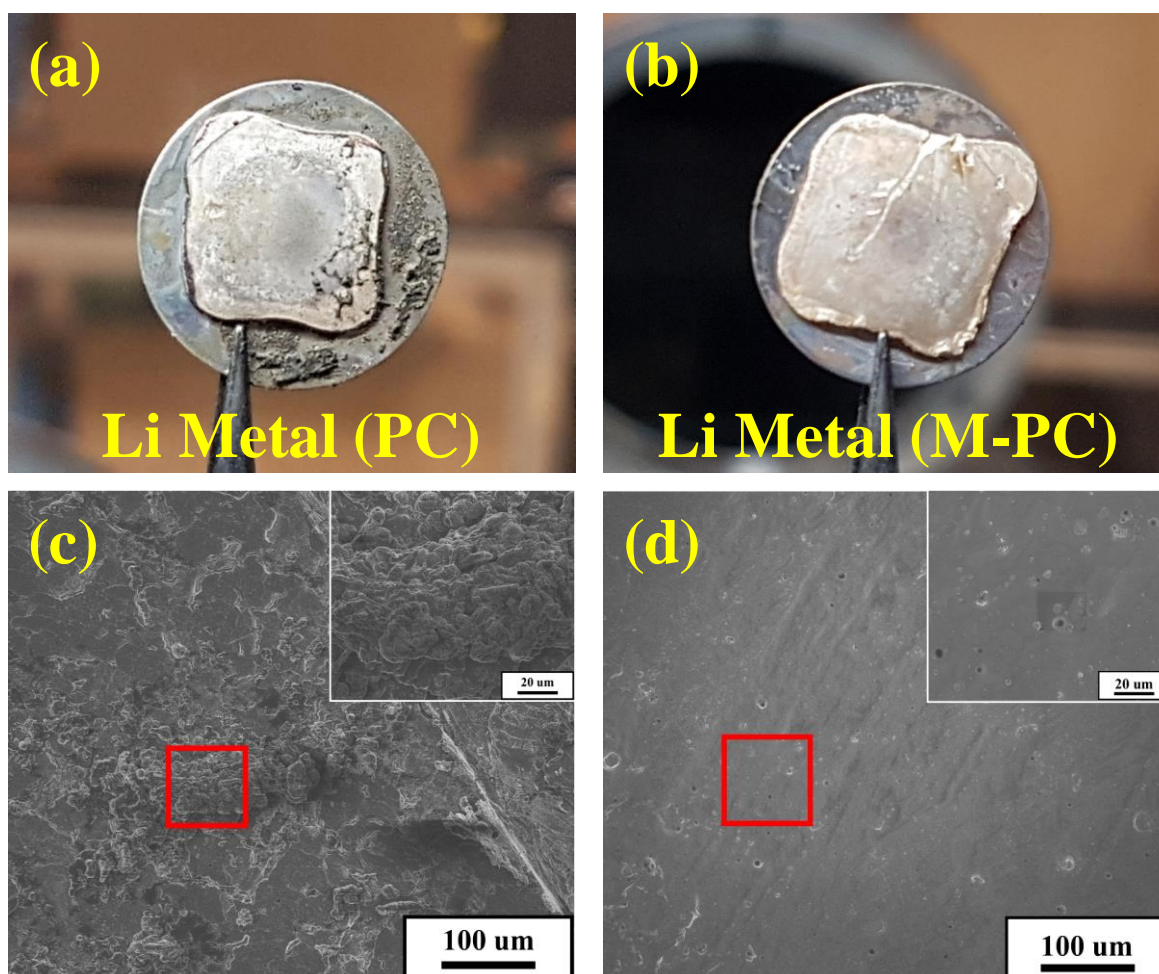


Figure 5.11 Characterization of Li metal foil after 250 cycle tests. Photographs of (a) Li foil in PC/S cell and (b) Li foil in M-PC/S cell; SEM images of (c) Li foil in PC/S cell and (d) Li foil in M-PC/S cell.

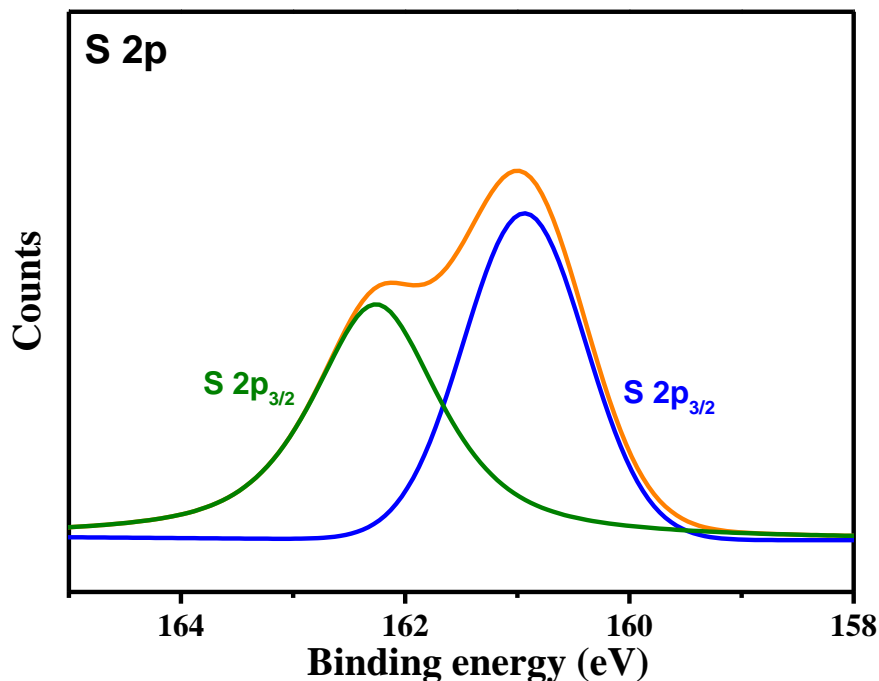


Figure 5.12 XPS result of black spots on cycled PC lithium foil.

5.5 Conclusion

In this chapter, we demonstrated an effective strategy of decorating nano-MnO₂ onto sulfur reservoir to further capture the out-diffused polysulfides via chemical interaction and thereby improve the electrochemical performances of sulfur cathode. Pistachio shell-derived carbon (PC) was employed as a sustainable carbon host to accommodate sulfur within the interconnected macro channels and micropores. After nano-MnO₂ decoration, cycle retention was dramatically improved with 62 % of initial capacity over 250 cycles and rate capability was also significantly enhanced. These favorable effects are mainly attributed to the synergistic contributions of the structural benefits of PC scaffold and the uniform decoration of nano-MnO₂ onto the PC scaffold. Raman analysis and ex-situ studies (SEM and XPS) confirmed that nano-MnO₂ has positive effects on capturing the polysulfides. Unlike the previous approach to physically hold polysulfides within sulfur container, our strategy of decorating nano-MnO₂, as a chemical agent, onto carbon scaffold

can provide a new guideline to address the fundamental challenges of sulfur cathode without increasing the mass burden of total battery configuration. In addition, it could be further extended to other materials which have chemical interaction with polysulfides and will boost the development of excellent sulfur container for Li-S batteries.

5.6 References

- 1 Ryu, J., Hong, D., Lee, H.-W. & Park, S. Practical considerations of Si-based anodes for lithium-ion battery applications. *Nano Res* (2017) **10**, 3970-4002.
- 2 Zhang, C., Wu, H. B., Yuan, C., Guo, Z. & Lou, X. W. Confining sulfur in double-shelled hollow carbon spheres for lithium-sulfur batteries. *Angewandte Chemie* (2012) **124**, 9730-9733.
- 3 Zhou, G., Zhao, Y. & Manthiram, A. Dual-confined flexible sulfur cathodes encapsulated in nitrogen-doped double-shelled hollow carbon spheres and wrapped with graphene for Li-S batteries. *Adv. Energy Mater.* (2015) **5**, 1402263.
- 4 Ji, X., Lee, K. T. & Nazar, L. F. A highly ordered nanostructured carbon-sulphur cathode for lithium-sulphur batteries. *Nature materials* (2009) **8**, 500.
- 5 Kim, J. H. *et al.* Hydroxylated carbon nanotube enhanced sulfur cathodes for improved electrochemical performance of lithium-sulfur batteries. *Chem. Commun.* (2015) **51**, 13682-13685.
- 6 Elazari, R., Salitra, G., Garsuch, A., Panchenko, A. & Aurbach, D. Sulfur-impregnated activated carbon fiber cloth as a binder-free cathode for rechargeable Li-S batteries. *Adv. Mater.* (2011) **23**, 5641-5644.
- 7 Ji, L. *et al.* Graphene oxide as a sulfur immobilizer in high performance lithium/sulfur cells. *J Am Chem Soc* (2011) **133**, 18522-18525.
- 8 Zhang, B., Qin, X., Li, G. & Gao, X. Enhancement of long stability of sulfur cathode by encapsulating sulfur into micropores of carbon spheres. *Energ Environ Sci* (2010) **3**, 1531-1537.
- 9 Zheng, G., Yang, Y., Cha, J. J., Hong, S. S. & Cui, Y. Hollow carbon nanofiber-encapsulated sulfur cathodes for high specific capacity rechargeable lithium batteries. *Nano Lett.* (2011) **11**, 4462-4467.
- 10 Liang, X. *et al.* Improved cycling performances of lithium sulfur batteries with LiNO₃-modified electrolyte. *J Power Sources* (2011) **196**, 9839-9843.
- 11 Liu, M. *et al.* Novel gel polymer electrolyte for high-performance lithium-sulfur batteries. *Nano Energy* (2016) **22**, 278-289.
- 12 Zhang, Z., Lai, Y., Zhang, Z., Zhang, K. & Li, J. Al₂O₃-coated porous separator for enhanced electrochemical performance of lithium sulfur batteries. *Electrochim. Acta* (2014) **129**, 55-61.
- 13 Yao, H. *et al.* Improved lithium-sulfur batteries with a conductive coating on the separator to prevent the accumulation of inactive S-related species at the cathode-separator interface. *Energ Environ Sci* (2014) **7**, 3381-3390.
- 14 Kim, P. J. H., Narayanan, S., Xue, J., Thangadurai, V. & Pol, V. G. Li-Ion-Permeable and Electronically Conductive Membrane Comprising Garnet-type Li₆La₃Ta₁.₅Y_{0.5}O₁₂ and Graphene Towards Ultra-stable and High-Rate Lithium Sulfur Batteries. *ACS Applied Energy Materials* (2018).
- 15 Kim, P. J. H., Kim, K. & Pol, V. G. Towards highly stable lithium sulfur batteries: Surface functionalization of carbon nanotube scaffolds. *Carbon* (2018) **131**, 175-183.
- 16 Liang, X. *et al.* Tuning transition metal oxide-sulfur interactions for long life lithium sulfur batteries: The “Goldilocks” principle. *Adv. Energy Mater.* (2016) **6**, 1501636.
- 17 Xing, W. B., Dunlap, R. A. & Dahn, J. R. Studies of lithium insertion in ballmilled sugar carbons. *J. Electrochem. Soc.* (1998) **145**, 62-70, doi:Doi 10.1149/1.1838212.

- 18 Shen, F. *et al.* Chemically Crushed Wood Cellulose Fiber towards High-Performance Sodium-Ion Batteries. *Acs. Appl. Mater. Inter.* (2015) **7**, 23291-23296, doi:10.1021/acsami.5b07583.
- 19 Lim, D. G. *et al.* Lithium storage in structurally tunable carbon anode derived from sustainable source. *Carbon* (2017) **121**, 134-142, doi:10.1016/j.carbon.2017.05.079.
- 20 Lotfabad, E. M. *et al.* High-Density Sodium and Lithium Ion Battery Anodes from Banana Peels. *Acs Nano* (2014) **8**, 7115-7129, doi:10.1021/nn502045y.
- 21 Kim, K. *et al.* Li-ion storage in an amorphous, solid, spheroidal carbon anode produced by dry-autoclaving of coffee oil. *Carbon* (2018).
- 22 Kim, P. J., Fontecha, H. D., Kim, K. & Pol, V. G. Towards High Performance Lithium Sulfur Batteries: Upcycling of LDPE Plastic into Sulfonated Carbon Scaffold via Microwave-promoted Sulfonation. *Acs. Appl. Mater. Inter.* (2018).
- 23 Kim, K. *et al.* Tailored Carbon Anodes Derived from Biomass for Sodium-Ion Storage. *Acs Sustain. Chem. Eng.* (2017) **5**, 8720-8728, doi:10.1021/acssuschemeng.7b01497.
- 24 Liang, X. *et al.* A highly efficient polysulfide mediator for lithium-sulfur batteries. *Nat. Commun.* (2015) **6**, doi:Artn 5682
10.1038/Ncomms6682.
- 25 Li, Z., Zhang, J. T. & Lou, X. W. Hollow Carbon Nanofibers Filled with MnO₂ Nanosheets as Efficient Sulfur Hosts for Lithium-Sulfur Batteries. *Angew. Chem. Int. Edit.* (2015) **54**, 12886-12890, doi:10.1002/anie.201506972.
- 26 Xie, X. & Gao, L. Characterization of a manganese dioxide/carbon nanotube composite fabricated using an in situ coating method. *Carbon* (2007) **45**, 2365-2373.
- 27 Tsang, C., Kim, J. & Manthiram, A. Synthesis of manganese oxides by reduction of KMnO₄ with KBH₄ in aqueous solutions. *J Solid State Chem* (1998) **137**, 28-32, doi:DOI 10.1006/jssc.1997.7656.
- 28 Devaraj, S. & Munichandraiah, N. Effect of crystallographic structure of MnO₂ on its electrochemical capacitance properties. *J Phys Chem C* (2008) **112**, 4406-4417, doi:10.1021/jp7108785.
- 29 You, Z., Li, G., Dang, J., Yu, W. & Lv, X. The mechanism on reducing manganese oxide ore with elemental sulfur. *Powder Technology* (2018) **330**, 310-316.
- 30 Yu, N. *et al.* High-Performance Fiber-Shaped All-Solid-State Asymmetric Supercapacitors Based on Ultrathin MnO₂ Nanosheet/Carbon Fiber Cathodes for Wearable Electronics. *Adv. Energy Mater.* (2016) **6**, doi:Artn 1501458
10.1002/Aenm.201501458.
- 31 Chen, Y. C. *et al.* Highly flexible supercapacitors with manganese oxide nanosheet/carbon cloth electrode. *Electrochim. Acta* (2011) **56**, 7124-7130, doi:10.1016/j.electacta.2011.05.090.
- 32 Kim, J. H., Lee, S., Lee, J. W., Song, T. & Paik, U. 3D-interconnected nanoporous RGO-CNT structure for supercapacitors application. *Electrochim. Acta* (2014) **125**, 536-542.
- 33 Wang, H. L. *et al.* Graphene-Wrapped Sulfur Particles as a Rechargeable Lithium-Sulfur Battery Cathode Material with High Capacity and Cycling Stability. *Nano Lett.* (2011) **11**, 2644-2647, doi:10.1021/nl200658a.
- 34 Carter, R. *et al.* Polysulfide Anchoring Mechanism Revealed by Atomic Layer Deposition of V₂O₅ and Sulfur-Filled Carbon Nanotubes for Lithium-Sulfur Batteries. *Acs. Appl. Mater. Inter.* (2017) **9**, 7185-7192, doi:10.1021/acsami.6b16155.

- 35 Kim, J. H., Choi, J., Seo, J., Kwon, J. & Paik, U. Two-dimensional Nafion nanoweb anion-shield for improved electrochemical performances of lithium-sulfur batteries. *J. Mater. Chem. A* (2016) **4**, 11203-11206, doi:10.1039/c6ta04203a.
- 36 Kim, P. J. H. *et al.* Synergistic protective effect of a BN-carbon separator for highly stable lithium sulfur batteries. *Npg Asia Mater.* (2017) **9**, doi:ARTN e375 10.1038/am.2017.51.
- 37 Mao, L., Zhang, K., Chan, H. S. O. & Wu, J. S. Nanostructured MnO₂/graphene composites for supercapacitor electrodes: the effect of morphology, crystallinity and composition. *J Mater Chem* (2012) **22**, 1845-1851, doi:10.1039/c1jm14503g.
- 38 Li, W. Y. *et al.* The synergetic effect of lithium polysulfide and lithium nitrate to prevent lithium dendrite growth. *Nat. Commun.* (2015) **6**, doi:Artn 7436 10.1038/Ncomms8436.

6. SUMMARY AND FUTURE PROSPECTS

In this chapter, the storyline of my Ph.D. work is summarized. Some of the parts in this chapter was extracted from the manuscripts of chapter 3, 4, and 5.

Carbon based materials for its high reversibility, stable cyclability, low potential, and high conductivity have been heavily studied for various energy storage including battery, supercapacitor, CO₂ capturing, and many others. Recent technology such as electric vehicles and large grid storage systems require higher capacity and cost-effective battery. To meet these demands, carbon based material derived from sustainable sources have been investigated for energy storage applications including lithium ion battery, sodium ion battery, and lithium sulfur battery in this thesis. A solvent-free carbon preparation method, named dry autoclave method, was utilized to prepare spherical carbon from coffee oil. The nucleation and growth of carbon is realized by the autogenic pressure and temperature inside a closed systems. To resolve the cost and geo-politic issue of lithium resource, sodium ion battery has been studied for the past decades. However, the larger size of sodium ion compared to lithium ion limits the selection of carbon material as anode. Carbon derived from sustainable sources show interlayer spacing sufficient for sodium ion intercalation. In this work, the carbonization temperature impact on biomass-derived carbon structure are studied. The correlation of storage mechanism and the structure of carbon was carefully elaborated. Finally, lithium sulfur battery with high capacity has attracted huge attention as a next-generation battery. The practical implement of lithium-sulfur battery is hindered by sulfur conductivity issue and the polysulfide shuttling effect which degrades the battery performances. Biomass derived carbon with macro-channel and micropores was used as sulfur reservoir. Synergic effect of physical restriction (carbon structure) and chemical restriction (MnO₂ decoration) has improved the Li-S battery performance. The cost-effective, eco-friendly, porous structure, and conductive property of biomass derived carbon is beneficial for various applications. Brief summary of each chapter and the future prospect of carbon in energy storage system is discussed in the next few paragraphs.

6.1 Coffee oil derived carbon for lithium ion battery

Numerous carbon preparation methods have been proposed including electro-spinning, solvothermal method, carbon exfoliation, and acid/base treatment. These methods are expensive, require sophisticated technique, and use environmental unfriendly solvents. To propose a cost-effective and environmental benign carbon preparation method, dry autoclave method which is solvent- and catalyst-free was introduced. Spherical carbon was successfully fabricated from coffee oil. The prepared carbon was used as an anode material for lithium ion battery. A stable cycle performance was obtained for both room temperature and elevated temperature condition over 250 cycles.

6.2 Biomass derived carbon for sodium ion battery and its storage mechanism study

Sodium ion batteries are suggested as an alternative energy storage system for lithium ion batteries for its advantages. Due to the larger ionic size of sodium compared to lithium, careful selection of carbon materials is essential. Biomass derived carbon has been heavily studied for its resource abundance and cost-benefits. In this study, due to its abundance and high porosity structure, pistachio shell was selected as the primary carbon source. Pistachio shell was carbonized at different temperature ranged from 700 to 1500 °C to understand the sodium storage mechanism and the electrochemical performance difference. Pistachio shell carbonized at 1000 °C resulted in highly amorphous structure with specific surface area (760.9 m²/g) and stable cycle performance (225 mAh g⁻¹ at 10 mA g⁻¹). Furthermore, the XRD, Raman, CV, and voltage profile of each carbonization temperature suggested a combination of defect sites, sp² content, pseudocapacitance, and intercalation as a possible storage mechanism. Our initial results obtained from carbonized pistachio shell suggest that sufficient electrochemical performance may be obtained from bio-waste materials, offering new pathways for sustainable electro-mobility and other battery applications.

6.3 Biomass derived carbon for lithium-sulfur battery

The polysulfide shuttling effect hinders the practical use of lithium-sulfur (Li-S) in commercial batteries. In this thesis to resolve the polysulfide issue, a physical trap (pistachio derived carbon) and a chemical trap (MnO₂ decoration) method is introduced. The macro-channel

and micropores structure of pistachio shell derived carbon (PC) facile the permeation of electrolyte into the structure and increase the sulfur loading. Nano-MnO₂ (less than 10 wt. %) decoration onto sulfur reservoir further improve the Li-S performance by capturing the out-diffused polysulfides via chemical interaction without increasing the mass burden of total battery configuration. The electrochemical performance of PC and M-PC are compared and discussed. To substantiate the improved performance by nano-MnO₂ decoration, Raman study has been conducted. Raman study confirmed the chemical reaction between MnO₂ and polysulfide.

6.4 Future outlooks

This thesis focus on utilizing carbon materials for various energy storage systems. Carbon material application can be expanded into lithium metal battery. Lithium metal battery has extremely high capacity of 3,000 mAh g⁻¹, however the risk of lithium dendrite growth hinders the practical use. Lithium dendrite growth is controlled by various factors including conductivity of electrode, uniformity of lithium ion flux, local current density and local heat spot on the electrode, and stability of SEI layer. One of author's future work is studying the impact of carbon orientation in film on the behavior of lithium dendrite growth. Differently orientated carbon film has different conductivity characteristics. The higher conductive film results in more uniform lithium dendrite growth, which improve the cell performance. Another study is the carbon size effect on lithium metal battery. An intercalating carbon materials coated on the PP separator can reduce the local current density applied on lithium counter-electrode. Further study is correlating the carbon size and lithium metal performance. The work presented in this thesis aims to show the infinite possibility of carbon materials in numerous energy storage systems.

VITA

Kyungho Kim received his B.S. in Material Science and Engineering from Korea University, Seoul, Korea. Kim began his research career after he joined Funnano group at KAIST, Daejeon, Korea, under the guidance of Prof. Yeonsik Jung. He studied self-assembly of block copolymer (BCP). The main goal of his research was to improve the BCP self-assembly process. He participated in a research team which was one of the first team to develop sub-10 mins assembly process. Also he studied the possibility of using BCP as an etching mask. As results, Kim successfully fabricated graphene quantum dot and graphene nanoribbon.

Kim enrolled at Purdue University in the School of Material Engineering in 2014 Fall under the guidance of Prof. Jeffrey Youngblood and Prof. Vilas Pol. Kim performed research in applying carbon materials into various energy storage systems such as lithium ion battery, sodium ion battery, lithium-sulfur battery, and lithium-metal battery. He has successfully published 8 SCI papers and two oral presentation at ECS meeting and TAPPI meeting. Kim has experience in lab set-up for Prof. Osswald (2014 – 2016) and served as safety manager. After joining ViPER group, Kim served as equipment super-user (Raman, SEM, TEM, BET, and many others).

PUBLICATIONS

1. **Kyungho Kim**, Geoffrey Daniel, Vadim G. Kessler, Gulaim A. Seisenbaeva, Vilas G. Pol “Basic Medium Heterogeneous Solution Synthesis of α -2 MnO₂ Nanoflakes as an Anode or Cathode in half Cell 3 Configuration (vs Lithium) of Li-ion Batteries”, *Nanomaterials* **2018**, 8 (8), 608, doi:10.3390/nano8080608.
2. Patrick J. Kim, **Kyungho Kim**, and Vilas G. Pol “Uniform Metal-Ion Flux through Interface-modified Membrane for Highly Stable Metal Batteries”, *Electrochimica Acta* **283** (2018) 517-527.
3. **Kyungho Kim**, Patrick J. Kim, Jeffrey P. Youngblood, and Vilas G. Pol “Surface Functionalization of Carbon Architecture with Nano-MnO₂ for Effective Polysulfide Confinement in Lithium-Sulfur Batteries”, *Chemsuschem* (2018), 11, 2375-2381, doi: [10.1002/cssc.201800894](https://doi.org/10.1002/cssc.201800894)
4. Patrick J. Kim, Harif Fontechas, **Kyungho Kim**, and Vilas Pol “Towards High Performance Lithium Sulfur Batteries: Upcycling of LDPE Plastic into Sulfonated Carbon Scaffold via Microwave-promoted Sulfonation”, *ACS Appl. Mater. Interfaces*, 2018, 10 (17), pp 14827 - 14834 doi: 10.1021/acsami.8b03959
5. **Kyungho Kim**, Ryan A. Adams, Patrick J. Kim, Anjela Arora, Enrico Martinez, Jeffrey P. Youngblood, and Vilas G. Pol. " Li-ion storage in an amorphous, solid, spheroidal carbon anode produced by dry-autoclaving of coffee oil." *Carbon* (2018), 133, 62 – 68, doi: [10.1016/j.carbon.2018.03.013](https://doi.org/10.1016/j.carbon.2018.03.013)
6. Patrick J. Kim, **Kyungho Kim**, Vilas G. Pol. “Towards highly stable lithium sulfur batteries: Surface functionalization of carbon nanotube scaffold.” *Carbon* (2018), 131, 175 – 183, doi: [10.1016/j.carbon.2018.01.100](https://doi.org/10.1016/j.carbon.2018.01.100).
7. **Kyungho Kim**, Daw Gen Lim, Changwan Han, Sebastian Osswald, Volkan Ortalan, Jeffrey Youngblood, and Vilas Pol. “Tailored Carbon Anodes for Sodium-ion Storage.” *ACS Sustainable Chemistry and Engineering*, 2017, 5 (10), 8720-8728.
8. Daw Gen Lim, **Kyungho Kim**, Mayuri Razdan, Sebastian Osswald, and Vilas G. Pol. “Structure Property Relationships of Lithium Storing Carbonaceous Particles Derived from Bioproduct.” *Carbon*, 2017, 121, 134-142.

9. Woon Ik Park, Yong Joo Kim, Jae Won Jeong, **Kyungho Kim**, Jung-Keun Yoo, Yoon Hyung Hur, Jong Min Kim, Edwin Thomas, Alfredo Alexander-Katz, and Yeon Sik Jung. “Host-Guest Self-assembly in Block Copolymer Blends.” *Scientific Reports* (2013), 3, 3190; doi: 10.1038/srep03190.
10. **Kyungho Kim**§, Jinsup Lee§, Woon Ik Park, Bo-Hyun Kim, Jong Hyun Park, Tae-Hoon Kim, Sungyool Bong, Chul-Hong Kim, GeeSung Chae, Myungchul Jun, Yongkee Hwange, YeonSik Jung*, and Seokwoo Jeon*. “Uniform Graphene Quantum Dots Patterned from Self-Assembled Silica Nanodots.” *Nano Letters*, 2012, 12, p. 6078- 6083,
11. Woon Ik Park, Jong Moon Yoon, Moonkyu Park, Jinsup Lee, Sung Kyu Kim, Jae Won Jeong, **Kyungho Kim**, Hu Young Jeong, Seok woo Jeon, Kwang Soo No, Jeong Yong Lee, and Yeon Sik Jung. “Self-Assembly-Induced Formation of High-Density Silicon Oxide Memristor Nanostructures on Graphene and Metal Electrodes.” *Nano Letters*, 2012, 12, p.1235 – 1240
12. Woon Ik Park, **Kyungho Kim**, Hyun-Ik Jang, Jae Won Jeong, Jong Min Kim, Jaesuk Choi, Jae Hong Park, and Yeon Sik Jung. “Directed Self-Assembly with sub-100 Degrees Celsius Processing Temperature, Sub-10 Nanometer Resolution, and Sub-1 Minute Assembly Time.” *Small*, 2012, 8, p.3762 - 3768